CHALMERS
UNIVERSITY OF TECHNOLOGY

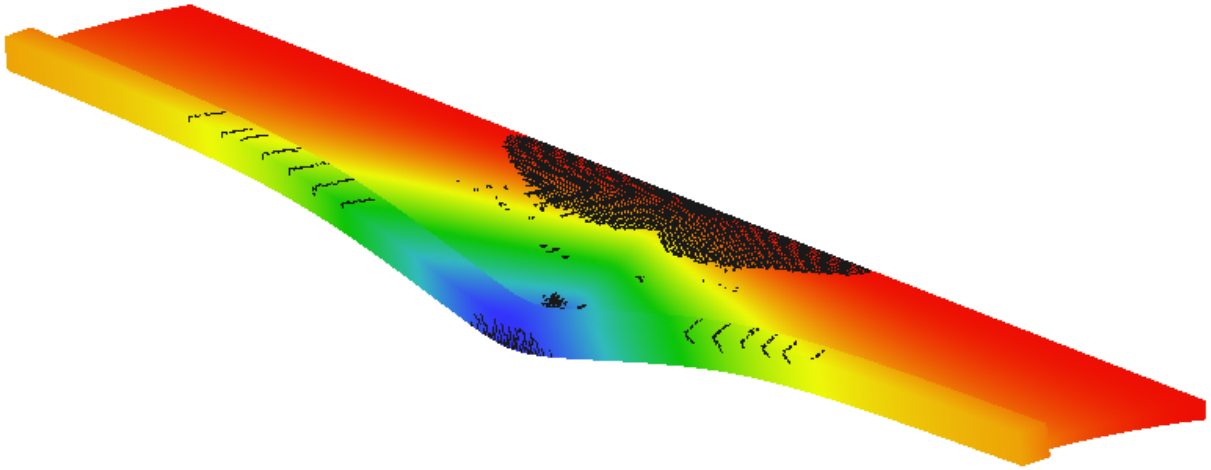

Point Load Distribution in Overhang Slabs

Effects of Model Complexity and Load History

Master's thesis in the Master's Programme Structural Engineering and Building Technology

Markus Johansson
Niklas Kjellberg

DEPARTMENT OF ARCHITECTURE AND CIVIL ENGINEERING
DIVISION OF STRUCTURAL ENGINEERING

CHALMERS UNIVERSITY OF TECHNOLOGY
Master's thesis ACEX30
Gothenburg, Sweden 2025

MASTER'S THESIS ACEX30

Point Load Distribution in Overhang Slabs

Effects of Model Complexity and Load History

Master's Thesis in the Master's Programme Structural Engineering and Building Technology

Markus Johansson
Niklas Kjellberg

Department of Architecture and Civil Engineering
Division of Structural Engineering
CHALMERS UNIVERSITY OF TECHNOLOGY
Gothenburg, Sweden 2025

Point Load Distribution in Overhang Slabs
Effects of Model Complexity and Load History
Master's Thesis in the Master's Programme Structural Engineering and Building Technology

Markus Johansson
Niklas Kjellberg

Supervisor: Mattias Blomfors, Norconsult Sverige AB
Examiner: Karin Lundgren, Division of Structural Engineering

Examensarbete ACEX30
Institutionen för Arkitektur och Samhällsbyggnadsteknik
Chalmers Tekniska Högskola, 2025

Department of Architecture and Civil Engineering
Division of Structural Engineering
Chalmers University of Technology
SE-412 96 Göteborg
Sweden
Telephone +46 31 772 1000

Cover:
The deformed shape of a reinforced concrete overhang slab including crack pattern.
Department of Architecture and Civil Engineering
Göteborg, Sweden, 2025

Point Load Distribution in Overhang Slabs
Effects of Model Complexity and Load History

Master's thesis in the Master's Programme Structural Engineering and Building Technology

Markus Johansson

Niklas Kjellberg

Department of Architecture and Civil Engineering
Division of Structural Engineering
Chalmers University of Technology

ABSTRACT

Understanding the distribution of point loads in overhang slabs is crucial for improving design and assessment of reinforced concrete bridges. The concept of an effective width allows shear forces and bending moments to be evaluated at critical sections and used in the dimensioning of the slab. While linear Finite Element (FE) analyses generally provide conservative and sufficiently accurate results, they may not fully capture the structural behaviour. Non-linear FE analyses offer a more realistic representation, but at the cost of increased computational effort and complexity. Finding a balance between accuracy and efficiency is therefore a key consideration.

This Master's thesis investigates the load-bearing capacity and force distribution resulting from concentrated loads using analysis models of varying complexity, aligned with current regulations. A series of load cases and geometries were analysed using conventional hand calculations, linear FE models, and non-linear FE models.

Findings reveal a significantly higher load-bearing capacity in non-linear analysis due to force redistribution following reinforcement yielding. Furthermore, the edge beam has little effect on the load-bearing capacity in linear models, while in non-linear analysis it significantly improves both capacity and force distribution. Hand calculations and linear analysis are conservative, simple, and relatively quick to perform, making them suitable for an initial evaluation of load-bearing capacity. However, if a higher capacity needs to be verified, non-linear FE analysis can be used to provide a more refined and potentially less conservative assessment.

The non-linear FE model was also subjected to a loading history, where the cantilever slab experienced sequential point loads at multiple locations, resulting in increased permanent deflections and cracking. However, the prior loading had low effect on the ultimate load-bearing capacity. Its main influence was observed in the serviceability limit state, where both deflection and crack width were increased.

Key words: shear force, moment, distribution, cantilever slab without shear reinforcement, non-linear finite elements modelling, load-bearing capacity

Fördelning av punktlaster i konsolplattor
Effekter av modellkomplexitet och lasthistorik

Examensarbete inom masterprogrammet Konstruktionsteknik och Byggnadsteknologi

Markus Johansson

Niklas Kjellberg

Institutionen för arkitektur och samhällsbyggnadsteknik
Avdelningen för Konstruktionsteknik
Chalmers tekniska högskola

SAMMANFATTNING

Förståelsen av hur punktlaster fördelas i konsolplattor är avgörande för att förbättra dimensionering och analys av armerade betongbroar. Användning av konceptet effektiv bredd möjliggör att tvärkrafter och böjmoment kan utvärderas i kritiska snitt och användas vid dimensionering av plattan. Även om linjära Finita Element (FE) analyser generellt ger konservativa och tillräckligt noggranna resultat, fångar de inte alltid konstruktionens verkliga beteende. Icke-linjära FE-analyser erbjuder en mer realistisk beskrivning, men till priset av ökad beräkningskomplexitet och modelleringstid. Att hitta en balans mellan noggrannhet och effektivitet är därför en viktig avvägning.

Detta examensarbete undersöker bärförmåga och kraftfördelning från koncentrerade laster med hjälp av analysmodeller av varierande komplexitet, i linje med gällande regelverk. Ett antal lastfall och geometrier analyserades med konventionella handberäkningar, linjära FE-modeller samt icke-linjära FE-modeller.

Resultaten visar på en avsevärt högre bärförmåga i de icke-linjära analyserna, främst till följd av lastomfördelning efter att armeringen börjat flyta. Vidare konstateras att kantbalken har liten påverkan på bärförmågan i linjära modeller, medan den i icke-linjära analyser ger en tydlig ökad effekt både på kapacitet och lastfördelning. Handberäkningar och linjära analyser är konservativa, enkla och relativt snabba att genomföra, vilket gör dem lämpliga för en initial bedömning av bärförmågan. Om en högre kapacitet behöver verifieras kan dock en icke-linjär FE-analys användas för att uppnå en mer detaljerad och mindre konservativ bedömning.

Den icke-linjära FE modellen belastades sekventiellt med punktlaster på flera olika positioner för att simulera lasthistorik. Detta ledde till ökad permanent nedböjning och sprickbildning. Den tidigare belastningen hade dock låg inverkan på den maximala bärförmågan. Den huvudsakliga effekten observerades i bruksgränstillståndet, där både nedböjning och sprickvidd uppvisade ökande värden.

Nyckelord: tvärkraft, moment, lastspridning, konsolplatta utan tvärkraftsarmering, icke-linjär finit element modellering, bärförmåga

Contents

Preface

This thesis explores the load-bearing capacity and distribution from point loads acting on reinforced concrete overhang slabs without shear reinforcement. Non-linear FE analyses are used to assess the accuracy and limitations of conventional hand calculation methods and linear FE models.

The work was carried out between January and June 2025 at Norconsult, in collaboration with Chalmers. It constitutes the final part of the master's program in Structural Engineering and Building Technology at Chalmers.

We would like to express our sincere gratitude to our supervisor, Mattias Blomfors, at Norconsult, for his valuable guidance and continuous support throughout this project. We also extend our thanks to our examiner, Karin Lundgren, from Chalmers, for her insightful feedback and suggestions.

Gothenburg, June 2025
Markus Johansson
Niklas Kjellberg

Notations

Roman upper case letters

A_{sl}	Reinforcement area
A'_{sl}	Compressive reinforcement area
COV	Coefficient of Variation
$C_{Rd,c}$	Shear resistance factor for concrete
D	Dynamic factor
DOF	Degree of Freedom
EC	Eurocode
E_{ck}	Characteristic modulus of elasticity for concrete
E_{cm}	Mean modulus of elasticity for concrete
$ECOV$	Estimate of Coefficient of Variation
E_s	Modulus of elasticity for steel
F_d	Design value of actions
FE	Finite Element
G_F	Fracture energy
$F_{F,GRF}$	Fracture energy using the GRF method
G_{F0}	Base value of fracture energy
$GRFm$	Global Resistance Factor method
GSF	Global Safety Factor
I_1	Moment of inertia considering both the edge beam and the adjacent part of the slab nearest to the outer wheel
I_2	Moment of inertia per unit width of the slab
L	Length
L_k	Length of cantilever including edge beam
M	Bending moment
M_{Ed}	Design bending moment
M_{Rd}	Design bending moment resistance
$M_{selfweight}$	Bending moment from self-weight
PSF	Partial Safety Factor
RC	Reinforced Concrete
R_d	Resistance of structure considering design values
R_k	Resistance of structure considering characteristic values
R_m	Resistance of structure considering mean values
SLS	Serviceability Limit State
ULS	Ultimate Limit state
V	Shear effect
V_{Ed}	Design shear load effect
V_R	Coefficient of variation for the resistance
$V_{Rd,c}$	Design shear resistance without shear reinforcement
$V_{selfweight}$	Shear effect from self-weight

Roman lower case letters

a	Horizontal distance from load to support
b	Width of loading area
b_{ef}	Effective width
b_x	Load dimension in x direction
b_y	Load dimension in y direction
b_w	Cross-section width
c	Coefficient for effective width considering moment
d	Effective depth
d_{ef}	Mean effective depth
d_y	Effective depth in transverse direction
d_z	Effective depth in longitudinal direction
f_{cd}	Design compressive strength of concrete
f_{ck}	Characteristic compressive strength of concrete
f_{cm}	Mean compressive strength of concrete
$f_{cm,GRF}$	Mean compressive strength of concrete using the GRF method
f_{cmo}	Reference value for fracture energy
f_{ctk}	Characteristic tensile strength of concrete
f_{ctm}	Mean tensile strength of concrete
$f_{ctm,GRF}$	Mean tensile strength of concrete using the GRF method
f_{yd}	Design yield strength of reinforcement steel
f_{yk}	Characteristic yield strength of reinforcement steel
f_{ym}	Mean yield strength of reinforcement steel
$f_{ym,GRF}$	Mean yield strength of reinforcement steel using the GRF method
h_{eb}	Height of edge beam
k	Size effect factor
m_{rx}	Reinforcement moment in x direction
m_{ry}	Reinforcement moment in y direction
m_x	Bending moment in x direction
m_{xy}	Torsional moment
m_y	Bending moment in y direction
n	Coefficient for effective width considering moment
t	Surface thickness
t_{k1}	Thickness of slab at support
t_{k2}	Thickness of slab at cantilever end
v	Velocity
w_{eb}	Width of edge beam
x	Depth of natural axis
y_{cs}	Distance between load and critical section

Greek lower case letters

α	Stress reduction factor for the concrete compression block
α_{cc}	coefficient accounting for long term effects and load application on compressive concrete
α_{ct}	coefficient accounting for long term effects and load application on tensile concrete
α_R	Sensitivity factor
β	Depth factor for the concrete compression block
β_R	Reliability index
γ_c	Partial safety factor for concrete
γ_{perm}	Load combination factor for self-weight
γ_R^*	Global resistance factor
γ_{Rd}	Model uncertainty factor
γ_s	Partial safety factor for steel
$\gamma_{traffic}$	Load combination factor for traffic loads
ε_c	Concrete strain
ε_s	Steel strain
μ	Factor for torsional moment in reinforcement moment
ν	Poisson's ratio
ρ_c	Density of concrete including reinforcement
ρ_l	Reinforcement ratio
ρ_{ly}	Longitudinal reinforcement ratio
ρ_{lz}	Transversal reinforcement ratio
σ_c	Concrete stress
σ_s	Steel stress
σ_s'	Compressive steel stress
$\chi_{Typf.M}$	Distribution factor of traffic loads considering moment
$\chi_{Typf.V}$	Distribution factor of traffic loads considering shear

1 Introduction

This chapter provides an overview of the aim of the thesis along with a background, situating it within a broader context to highlight its significance. The problem description and methodology are also explained.

1.1 Background

The construction sector accounts for 22 % of the annual emissions in Sweden (Boverket, 2024) and the use of concrete is a significant part of this. Therefore, it is important to minimize the use of concrete in new bridges and to extend the lifetime of existing bridges. The Swedish Transport Administration is responsible for managing 21 000 bridges in Sweden (Trafikverket, 2023b) which regularly need to be inspected and maintained. In 2018, the Swedish Road Administration decided to upgrade the classification for 70 to 80 % of the heavy road network until 2029 from BK1 to the new BK4, which means an increase in the gross vehicle weight from 64 to 74 tons (Natanaelsson & Eriksson, 2020). Therefore, the load-bearing capacity for many bridges must be re-evaluated. By increased understanding about the structural behaviour and optimized modelling, through different modelling complexities, a sufficient load-bearing capacity may be proved and unnecessary reconstruction avoided.

To achieve sufficient width in beam bridges, the bridge deck slab typically cantilevers beyond the main girders. In new constructions, optimizing the design of Reinforced Concrete (RC) cantilever bridge deck slabs can reduce material use and minimize environmental impact. In the same way, precise analysis of existing structures can increase their life span. To enable efficient analyses of overhang slabs in existing bridges, it is important to know what level of modelling complexity should be used and how conservative each approach is. Hand calculations based on simplified assumptions generally give faster and more conservative results compared to more detailed analyses, such as linear elastic Finite Element (FE) analysis, which typically provide more accurate results, while non-linear analysis, which also can account for the material's non-linear properties, give even more realistic results but is more time consuming.

1.2 Problem description

In this thesis, the load distribution for RC overhang slabs at different levels of modelling complexity, was investigated, as well as how loading history affects the load-bearing capacity. Reissen and Hegger (2016) showed how the load spreading rule does not correlate to measured experimental result regarding how forces from point loads are distributed in overhang RC slabs. Although FE analysis provides more realistic results, it is also more time-consuming and requires higher computational power. Finding a balance between reliable and not overly conservative results and limiting the use of cost-inefficient tools is essential.

Furthermore, in non-linear FE analysis there is an uncertainty how the load history can influence the result. This thesis has investigated how the structural response can change as a result of previous service loads and the load-bearing capacity of an overhang slab. Repeated or sustained loading leading to formation and propagation of cracks change the internal stress distribution and stiffness of the slab. These changes can impact and potentially reduce the slab's overall load-bearing capacity. Understanding how the FE

model is influenced by previous loading is essential for accurately assessing the slab's performance and ensuring its long-term safety and reliability.

1.3 Aim

This Master's thesis aims to describe and explain how different model complexities, from conventional hand calculations to non-linear FE-analysis, differ in terms of distribution of point loads in RC overhang slabs, while also examining how load history influences the distribution in non-linear FE analysis.

1.4 Limitations

In this thesis, only RC overhang slabs without shear reinforcement was investigated, as these are the most commonly used. Further, a limited amount of geometries and load cases was considered.

1.5 Methodology

The first step of the thesis work was to perform a literature review which served to gain an understanding of the topic and the current knowledge in the field regarding how modelling complexity can influence the load-bearing capacity. Additionally, ways to account for loading history on different levels of modelling complexity was investigated. Also, the thesis work included a review of the regulations which needed to be considered.

A selection of geometries was chosen, with a base geometry serving as the reference. Key parameters was systematically varied from this base to study their effects. The following steps describe the different analyses that was conducted, which follows the different assessment levels from Plos et al. (2017):

- Performing hand calculations by developing a python-script based on Eurocode 2 and regulations from the Swedish Road Administration. These calculations were used to determine the load effects for different slab geometries and loading cases.
- The different cases were also analysed by using linear FE-modelling and compared to the results from the hand calculations. The software FEM-Design (Strusoft, 2025) was used for the linear FE-models.
- Non-linear analyses in the software ATENA (Cervenka Consulting, 2025) was carried out for a selection of cases considering non-linear material properties. The cantilever slab was also analysed considering previous service loads which were used to investigate the influence on load capacity and distribution.

The shear force and moment distributions at critical sections were analysed and compared to identify similarities and differences across the different assessment levels. Additionally, the ultimate load-bearing capacity and corresponding failure modes were evaluated and compared.

1.6 Utilization of AI tools

In this report, AI tools has been used to support the writing process by improving language quality and assist with Python programming.

2 Behaviour of Overhang Slabs

RC overhang slabs primarily exhibit three main failure modes: moment failure, shear failure, and punching shear failure. This chapter provides a general overview of these failure mechanisms and behaviour of overhang slabs along with a brief discussion of key properties of reinforced concrete. Additionally, relevant results from experimental studies conducted in this field are summarized.

Throughout this report, the term longitudinal direction refers to the direction of traffic flow, parallel to the bridge's main span, while the transversal direction is perpendicular to it. Additionally, regarding the overhang slab, the length refers to the extent of the slab in the transversal direction, and width corresponds to its dimension in the longitudinal direction. Directions are defined in Figure 2.1 below.

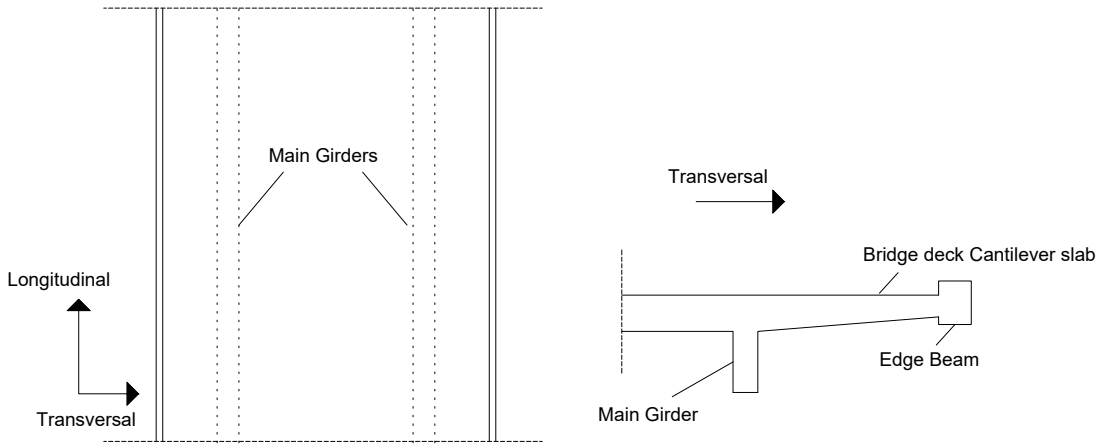

Figure 2.1: Definition of longitudinal and transversal direction for a bridge deck.

2.1 Behaviour of reinforced concrete

RC structures rely on the combined properties of concrete and steel reinforcement to resist applied loads. Concrete is a brittle material that primarily resists compressive forces, while steel reinforcement, which has a ductile behaviour, provides tensile resistance. The stress-strain relationships for concrete and reinforcing steel, shown in Figure 2.2, illustrate their fundamental mechanical properties.

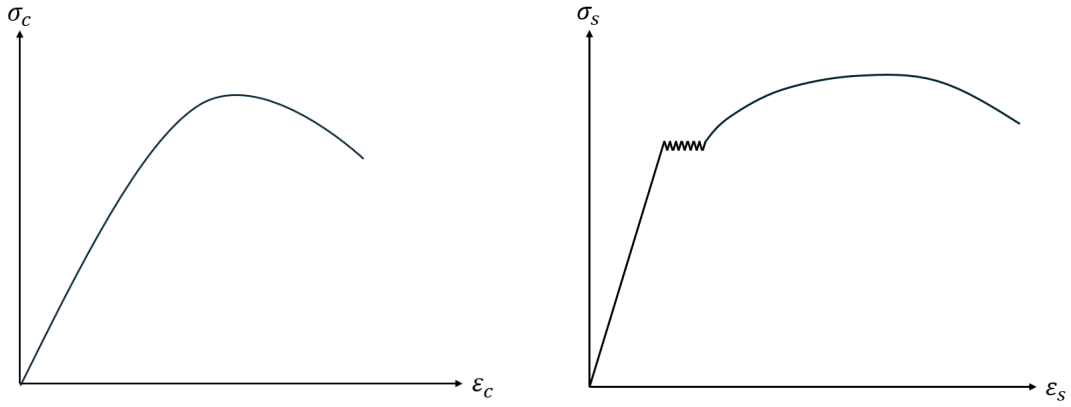

(a) Concrete **(b)** Reinforcing Steel

Figure 2.2: General stress-strain relationships for concrete in compression and reinforcing steel with yield plateau in tension.

Concrete exhibits a non-linear stress-strain behaviour, characterized by an initial linear elastic phase, followed by a gradual transition into non-linearity due to microcracking, and eventually reaching a peak stress before softening occurs. The ultimate strain capacity is relatively low, making concrete susceptible to cracking under tensile stresses. Reinforcement steel, on the other hand, typically exhibits an elastic-plastic behaviour, with an initial linear response followed by yielding and strain hardening. The high ductility of steel allows it to sustain large deformations before failure, which is crucial for the redistribution of internal forces in RC structures.

Due to the interaction between concrete and reinforcement, RC structures experience non-linear behaviour, particularly as cracks develop in the tensile zone. This non-linearity is reflected in the moment-curvature relationship, illustrated in Figure 2.3, which captures the change in stiffness as the concrete cracks. As the curvature increases, cracks begin to form in the tensile zone, leading to a significant reduction in stiffness in these regions. Consequently, internal forces are redistributed across different cross-sections, resulting in higher stresses in uncracked sections and altering the overall moment distribution (Engström, 2015).

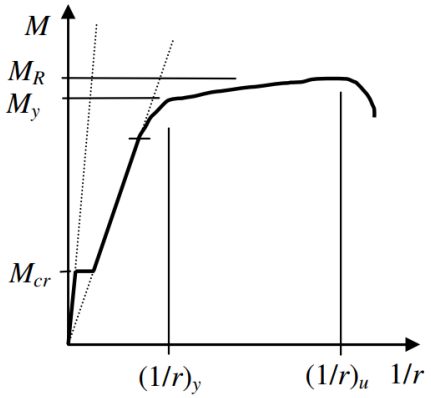

Figure 2.3: Moment-curvature relationhip for reinforced concrete (Al-Emrani et al., 2013).

Even in regions with stabilized cracking, the bond between the concrete and reinforcement allows for the transfer of tensile stresses, contributing to an overall increase in stiffness, compared to fully cracked regions. This phenomenon, known as tension stiffening, results in a lower average strain in the reinforcement between cracks compared to within the cracks. Additionally, as the reinforcement carries the tensile forces in cracked areas, the surrounding concrete becomes tensile-free, leading to a release of stresses and a corresponding bond stress-slip effect. Figure 2.4 illustrates a commonly used bond stress-slip relationship, adapted from the Model Code 2010 (CEB-FIP, 2013).

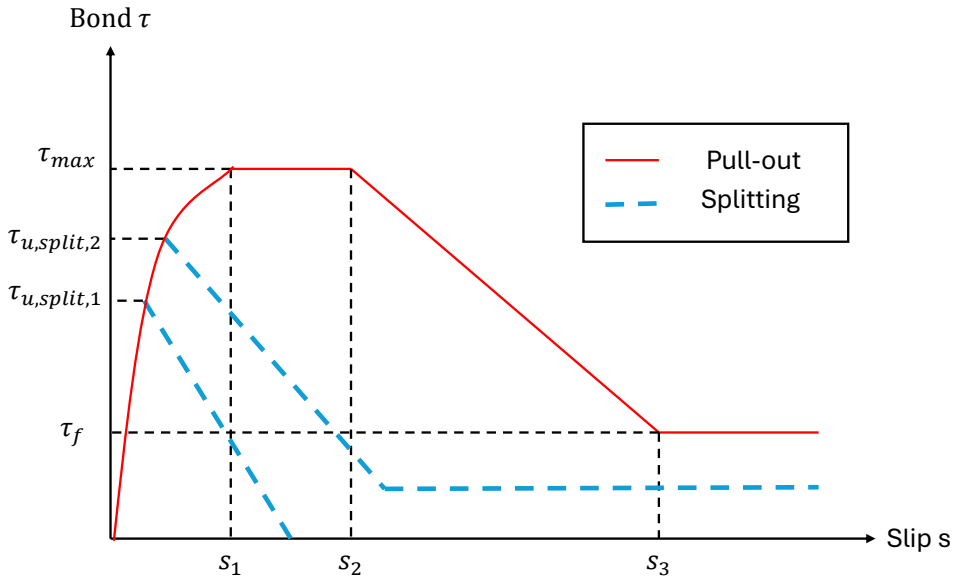

Figure 2.4: Bond stress-slip relation, adapted from Model Code 2010 (CEB-FIP, 2013). The red line indicates pull-out failure and the dashed blue lines splitting failure. The lower dashed blue line is used for unconfined concrete and the upper for stirrups.

2.2 One- and two-way action in RC slabs

When subjected to external loads, cantilever bridge deck slabs primarily carry forces in the transversal direction, with bending reinforcement arranged accordingly and secondary reinforcement provided in the longitudinal direction. For analytical purposes, the slab is often divided into strips of unit width, each modelled as an individual beam spanning from the support to the free edge. Under uniformly distributed loads, these strips transfer their load directly to the support, following a one-way action (Engström, 2014). However, when exposed to concentrated loads, the load transfer mechanism becomes more complex. Instead of being carried exclusively in the primary span direction, a portion of the load is redistributed longitudinally due to internal compatibility requirements and stiffness variations within the slab. This occurs because adjacent strips cannot deflect independently, resulting in internal shear forces that facilitate lateral load transfer. Consequently, a cantilever slab subjected to concentrated loads exhibits an intermediate behaviour between one-way and two-way action, where the extent of longitudinal load redistribution depends on the slab geometry, reinforcement layout, and boundary conditions.

A higher reinforcement ratio in the longitudinal direction enhances the slab's ability to redistribute concentrated loads in the longitudinal direction, increasing the two-way action response. Furthermore, the presence of edge beams or thickened slab sections at the free edge improves longitudinal stiffness. The effectiveness of this load distribution is also influenced by the cracking state of the slab, as cracks can reduce stiffness and alter distribution. The contribution of longitudinal action is particularly significant when concentrated loads are located near the free edge, creating the highest moment demands at the clamped edge.

2.3 Moment distribution

In cantilever slabs, loads are carried in both the main load-bearing direction and the longitudinal direction through two-way action. The addition of an edge beam significantly alters this distribution by increasing the slab stiffness in the longitudinal direction. This results in reduced localized deflections and an enhanced ability of the slab to redistribute loads longitudinally. When cracking occurs and stiffness is lost, the load is transferred to the stiffer regions, a phenomenon known as moment redistribution due to cracking. Once the reinforcement reaches its yield strength, the moment capacity is attained, and further redistribution takes place. At the serviceability level, the redistribution is governed by the stiffness distribution between cracked and uncracked regions, whereas at higher load levels (ULS), the moment distribution is primarily determined by the moment capacity of different regions.

The yielding moment represents the point at which the reinforcement begins to yield, marking the transition from elastic to plastic behaviour. Beyond this point, the section can undergo plastic deformations and moment be redistributed in the structure, provided sufficient ductility is available. The slab's plastic rotation capacity determines its ability to redistribute moments before reaching a collapse mechanism. A high plastic rotation capacity enables the slab to develop alternative load paths (Engström, 2014).

Moment distribution in slabs is complex and difficult to determine accurately by hand calculations. The interactions between different moment components and the redistribution effects make manual validation challenging. Therefore, numerical methods such as FE analysis are commonly used to obtain more precise results and ensure that the design meets structural safety and serviceability requirements. According to EN 1992-1-1, sectional forces in a slab can be determined using the structural analysis methods described in Section 5 of EN 1992-1-1:

- **Linear elastic analysis**
- **Linear analysis with limited redistribution**
- **Plastic analysis** (limit analysis), which includes:
  - Lower bound approach (static method)
  - Upper bound approach (kinematic method)
- **Non-linear analysis**

In limit analysis, moment distribution can be evaluated using both lower and upper bound solutions. The lower bound approach ensures equilibrium and material strength without exceeding yield limits, providing a conservative estimate of load capacity. In contrast, the upper bound approach assumes a collapse mechanism and estimates load

capacity based on energy principles. While the upper bound method can lead to efficient designs, it requires verification to avoid unconservative results (Engström, 2014).

The moment field in a cantilever slab describes the spatial distribution of bending moments, where beam theory considers only a single bending moment (m_x), while plate theory incorporates both transverse (m_x) and longitudinal (m_y) moments, as well as the torsional moment (m_{xy}) (Engström, 2014). These interactions become particularly significant in the presence of an edge beam, which influences the global moment distribution and enables load sharing between different directions. When analysing moment distribution in slabs subjected to concentrated loads, beam theory is more applicable for less stiff slabs, giving conservative results, while plate theory provides a more precise representation when stiffness is significant in both directions (Engström, 2014). Section 4.3 explains a method for calculating moment capacity in overhang slabs, where moments from concentrated loads are distributed along the support, considering the slab's longitudinal stiffness under the assumption of an uncracked section.

The moment field in a structural element is composed of both bending moments and torsional moments. For the structure to remain stable, this combined moment field must be balanced by the reinforcement moment, which is calculated by:

$$m_{rx} = m_x \pm \mu |m_{xy}| \tag{2.1}$$

$$m_{ry} = m_y \pm \frac{1}{\mu} |m_{xy}| \tag{2.2}$$

where m_x and m_y is bending moment in the x and y direction respectively, m_{xy} is the torsional moment and μ a factor that is usually set to 1. This equilibrium ensures that the structural element can safely resist the applied loads without excessive deformation or failure.

The yield line method, which follows the upper bound approach, estimates the ultimate load by assuming a collapse mechanism, but requires validation to ensure safety. A yield line represents the failure mode, indicating where the slab reaches its load-bearing capacity and a kinematic collapse mechanism forms. The placement of load dividing lines, where shear force is zero, depends on the slab's stiffness properties. A pronounced crack where plastic rotation occurs is referred to as a yield line, and it must form in a manner that ensures the collapse mechanism is kinematically possible. Figure 2.5 illustrates a typical yield line pattern for a cantilever slab subjected to concentrated loads.

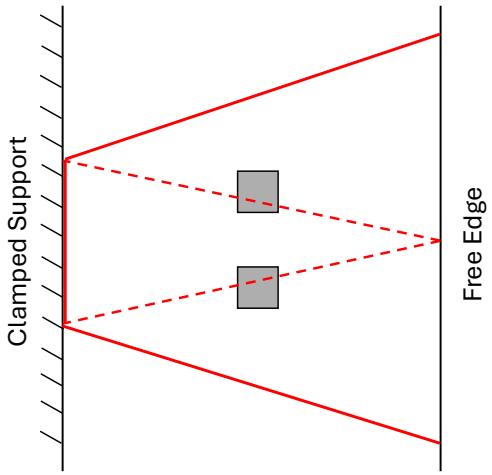

Figure 2.5: Yield line pattern for a cantilever slab subjected to concentrated loads, gray boxes. The solid lines show the yield lines at the top while the dotted lines show the yield lines at the bottom of the slab (Shu et al., 2019).

2.4 Shear effects

Shear forces in RC slabs can be a governing design criteria, especially when subjected to concentrated loads in slabs without shear reinforcement. The shear capacity is influenced by several parameters, such as load position, effective depth, aggregate and concrete properties, and the reinforcement ratio. The bending moment and potential yielding of the reinforcement also affect the shear capacity.

Cantilever slabs subjected to concentrated loads near the support exhibit increased load-carrying capacity. If the load is applied on the upper side of the slab within a distance $a < 3d$ from the centreline of the linear support, where d is the effective depth, the concentrated load is transferred via arch action (Al-Emrani et al., 2013), resulting in direct strutting illustrated in Figure 2.6. According to EN 1992-1-1, section 6.2.3, the portion of the load contributing to the shear force can be reduced by a factor $a/2d$, provided the load is applied within the distance $0.5d < a < 2.0d$. If the load is applied beyond direct arch action in structures without shear reinforcement, the shear force is transferred through a series of parallel compressive struts, which are interconnected by vertical or inclined tension ties. These tensile forces can be provided by friction and aggregate interlock effects in inclined cracks (Al-Emrani et al., 2013).

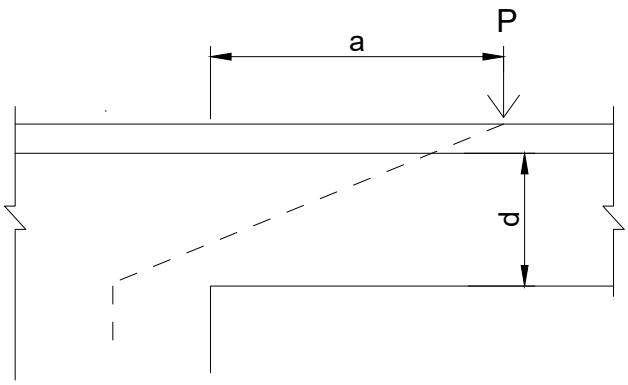

Figure 2.6: Mechanism of arch action Adopted from (Al-Emrani et al., 2013)

The effective width b_{ef} represents the width over which a concentrated load is assumed to be distributed. Although the actual load distribution is not strictly linear, an average stress is considered across this width for calculation and estimation purposes. Various methods for determining the effective width are described in Section 3.1.1.

Reissen and Hegger (2016) showed that a load applied close to the support, where arch action occurs, not only increases shear capacity but also leads to an increase in the measured effective width at the support. This phenomenon is attributed to direct strut formation, which allows a larger portion of the slab width to actively resist shear. In contrast, when the load is applied further away, the effective width decreases as the shear force is transferred through a more distributed shear field, relying on a series of inclined compressive struts and tensile ties instead of a direct force path. Experimental results demonstrated an increase of more than 70% in effective width for loads applied closer to the support, because shear transfer became more direct through compression struts instead of being spread over a broader shear field. This behaviour contrasts with the approach used in Eurocode 2 (EC2), where the load spreading rules assume that the effective width increases with distance from the support. The results suggest that the load spreading rule may not accurately capture shear behaviour in cantilever slabs, as it can be too conservative when the load is applied close to the support or the critical section investigated and overestimate the capacity when the load is applied further away (Reissen & Hegger, 2016).

When a concentrated load is applied beyond the arch action region in a slab without shear reinforcement, the shear force is transferred through internal mechanisms acting in parallel, Figure 2.7 illustrates the general behaviour of this forces. As loading increases, shear-carrying mechanisms interact to resist and redistribute shear forces. The total shear capacity depends on the combined contributions of compression zone action, aggregate interlock, and dowel action (Muttoni & Simões, 2023). When crack widths exceed a critical limit, shear transfer becomes ineffective, leading to brittle failure. This mechanism involves a force couple between the compression zone in the lower part of the slab and the tensile reinforcement in the upper part of the slab, called cantilever action. Aggregate interlock transmits shear across rough crack surfaces, preventing excessive slip between cracked segments. Dowel action occurs as transversal reinforcement resists displacement across inclined cracks, providing shear resistance through stiffness and bond with the concrete.

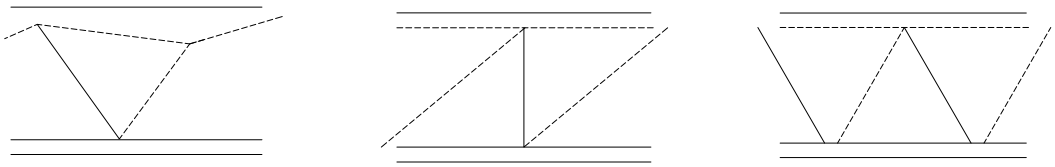

(a) Cantilever action (b) Aggregate interlock action (c) Dowel action

Figure 2.7: Shear-carrying mechanism (a) Cantilever action, (b) Aggregate interlock action and (c) Dowel action, dashed line is compressive forces and solid line is tensile forces. Adopted from Muttoni and Fernández Ruiz (2008).

The thickness of a RC slab has a significant influence on its shear capacity due to the phenomenon called size effect. The size effect describes the reduction in nominal shear strength as the effective depth of a member increases. This reduction is primarily attributed to the wider and more critical shear cracks that develop in deeper members, which reduce the effectiveness of aggregate interlock and other shear transfer mechanisms (Muttoni & Simões, 2023). As member size increases, these cracks become more dominant, limiting the ability of the concrete to transfer shear stresses across the failure plane. Additionally, deeper slabs tend to require less longitudinal reinforcement for flexure, which can further decrease the slab's ability to resist shear due to lower dowel action and diminished residual tensile stresses across cracks (Muttoni & Simões, 2023). In EN 1992-1-1 a size effect factor is included in the shear strength equation when the effective depth increase by more than 200 mm. The size effect factor is expressed as $k = 1 + \sqrt{200/d}$, where d is the effective depth in millimetres and $k \leq 2.0$. This factor reduces the nominal shear strength for deeper members, taking into account the effect of size.

2.5 Structural behaviour in experimental testing

Shear failure in overhang slabs is typically governed by two critical sections: one located near the concentrated load and the other at the line support. The exact position of these sections depends on the number and arrangement of concentrated loads. One-way shear failure is predominant when the shear field acts over a section perpendicular to the support. At the linear support, stresses from the maximum bending moment and shear force can contribute to failure (Setiawan et al., 2024). Punching shear failure occurs near the concentrated load when shear field acting around the loading area exceeds the concrete's punching capacity, forming a conical failure surface. Experimental observations from Setiawan et al. (2024) indicate that failure occurs close to the loaded area rather than at the support for cantilever slabs, but the failure cracks are more similar to one-way shear cracks than punching.

According to Muñoz et al. (2023), experimental tests on overhang slabs without shear reinforcement are usually not conducted on a scale or width sufficient to obtain accurate results. Furthermore, although most bridges include an edge beam system, experiments typically do not include an edge beam. Few full-scale tests are conducted, as they are very expensive, require a large testing facility, and are time consuming. Muñoz et al.

(2023) recommend that the width-to-span ratio, b/s, of tested slabs should be between 4.0 and 4.5, and between 5.3 and 6.1 when an edge beam is present. A too small width in test slabs not only limits the load capacity but may also alter the failure mode. Narrower overhang slabs may fail in flexure, whereas wider ones may fail in shear. Tapered slabs are likely to fail locally in the vicinity of the applied load.

A study by Vaz Rodriguez (2007) involved six large-scale tests on two RC cantilever slabs without shear reinforcement, simulating real bridge deck slabs at a 3/4 scale of their actual size. Compared to smaller-scale tests, these larger specimens account for the size effect in shear more accurately (and has also a better b/s ratio than other experimental test). The tested slabs measured 10 m in longitudinal direction, with a cantilever span of 2.78 m and a thickness varying from 190 mm at the free edge to 380 mm at the clamped support, shown in Figure 2.8. The transverse reinforcement ratios were 0.78% and 0.60%. The load cases were designed to align with EC2 and included one, two, and four concentrated loads. The results confirmed that cantilever bridge deck slabs without shear reinforcement fail in a brittle shear mode before a fully developed flexural mechanism can form.

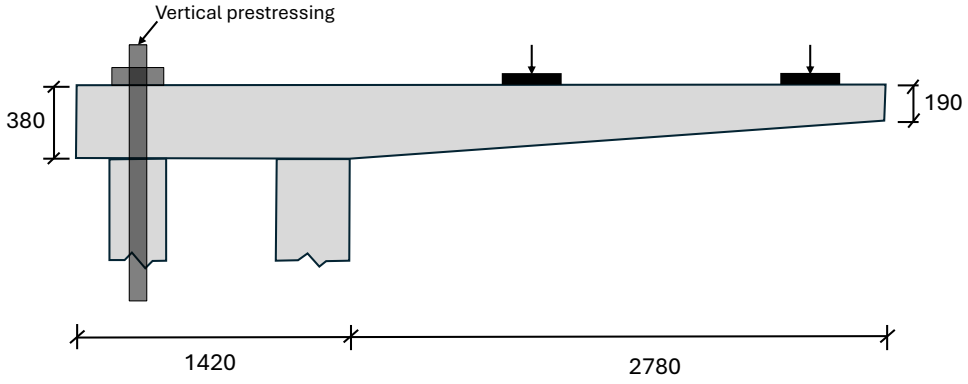

Figure 2.8: Geometry of experimental setup, adopted from Vaz Rodriguez (2007)

The study is further discussed in Vaz Rodriguez et al. (2008), which describes that the failure process begins with flexural cracks forming along the fixed edge on the top surface of the slab, induced by tensile stresses from bending moments. As the load increases, these flexural cracks widen, while shear-induced transverse cracks appear on the bottom surface near the applied loads. As these cracks grow, they eventually form a critical inclined shear failure surface that encloses the concentrated load area. All tested specimens exhibited shear failure via a shear failure surface surrounding the concentrated loads. Shear failure occurred before significant yielding of the flexural reinforcement, highlighting the brittle nature of the failure mechanism. Additionally, specimens with a higher reinforcement ratio demonstrated increased load capacity and deflection.

For practical applications, Vaz Rodriguez et al. (2008) propose that a three-sided control perimeter can be adopted to assess the shear strength of cantilever bridge deck slabs subjected to concentrated loading. This approach provides conservative and reliable results when combined with punching shear formulations from EN 1992-1-1, making it suitable for structural design purposes. The basic control perimeters is presented in Figure 2.9.

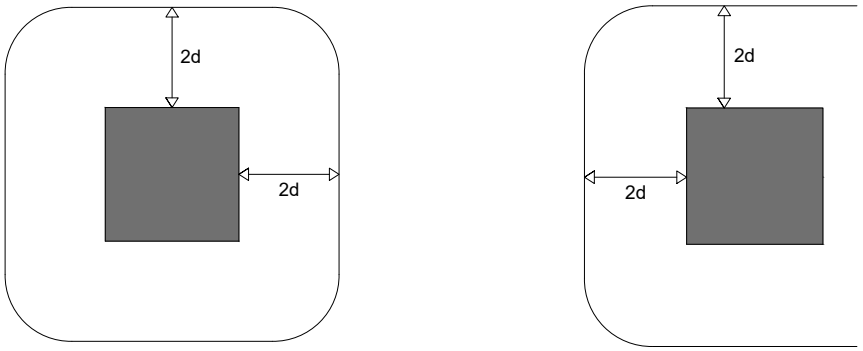

(a) **(b)**

Figure 2.9: Basic control perimeters for punching shear failure for a) general perimeter according to EN 1992-1-1 and b) for a a three-sided control perimeter.

The presence of concentrated loads leads to a non-uniform distribution of shear forces along the slab, particularly near the load introduction zone (Setiawan et al., 2024). This creates localized regions of high shear stress, which are critical for the initiation and propagation of the shear failure surfaces. Factors such as the reinforcement ratio, slab thickness, and loading configuration strongly influence the slab's shear strength and failure behaviour. According to Setiawan et al. (2024) experimental observations shows that slabs can redistribute significant internal forces when concentrated loads are subjected close to the linear support.

An FE model of the full-scale test cantilever slab from Vaz Rodriguez (2007) was conducted by Muñoz et al. (2023). Their FE simulation showed a failure load of 1325 kN, compared to the test failure load of 1396 kN. However, when an edge beam with dimensions 400×400 mm was added to the FE model, the load capacity increased by 20 %.

3 Multi-level assessment of RC slabs

This chapter presents general theory on the assessment of RC structures at different levels of detail, ranging from simplified analytical methods to advanced numerical modelling. The analysis of RC overhang slabs subjected to concentrated loads can be approached at multiple levels, each offering a different balance between accuracy and computational complexity. The first level provides a simplified and conservative response, while each following level incorporates more complex modelling, capturing the slab behaviour in greater detail. Plos et al. (2017) proposed a multi-level assessment of RC bridge deck slabs:

- Level I: Conventional simplified methods
- Level II: 3D linear shell FE-analysis
- Level III: 3D non-linear shell FE-analysis
- Level IV: 3D non-linear FE analysis with continuum elements and fully bonded reinforcement
- Level V: 3D non-linear FE analysis with continuum elements including reinforcement slip

3.1 Level 1 - Simplified methods

The first level of the multi-level assessment uses hand calculations based on simplified methods and aims to provide conservative estimates of the structural capacity. This section introduces the concept of effective width as a simplification for evaluating load effects. Furthermore, it presents commonly used local resistance models for assessing bending, shear, and punching shear capacity.

3.1.1 Effective width

The effective width b_{ef} is used in simplified calculations to transform a complex shear distribution into an equivalent one-dimensional force per unit width. There are two main approaches to defining b_{ef}: the smeared width approach and the load spreading rule. The latter assumes that a concentrated load is distributed towards the support at a constant angle, typically taken as $45°$. EC2 follows this method, but national adaptations differ in the exact starting point of the angle, illustrated in Figure 3.1 including the effective width from the smeared approach used in Sweden, which is described later in this section. Muñoz et al. (2023) provides a detailed comparison of various effective width formulations used in practice. These approaches, primarily geometric, are summarized in Table 3.1, where a is the horizontal distance from the load to the support, b_x and b_y are load plate dimensions, and d is the effective slab depth.

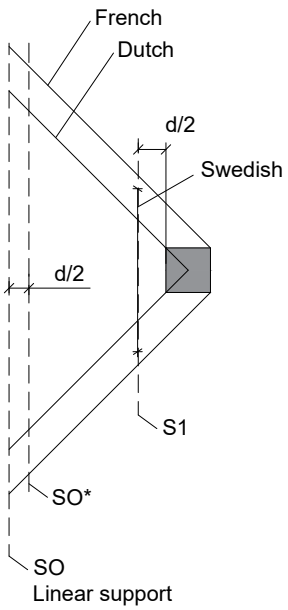

Figure 3.1: Critical sections for the smeared method used in Sweden and the load spread rule from the Dutch and French method using 45 degrees angle. Adopted from Muñoz et al. (2023).

The study by Muñoz et al. (2023) evaluated these formulations through non-linear FE simulations and a compilation of previous experimental comparisons. The findings indicate that geometric approaches, such as the French and Dutch methods, tend to be either overly conservative or unsafe, not following the realistic behaviour. This conclusion is aligning with the experimental tests conducted by Reissen and Hegger (2016), as discussed in Section 2.4.

Table 3.1: Effective width b_{ef} formulations for shear distribution according to different codes (Muñoz et al., 2023).

Method	**Control Section**	**Equation for** b_{ef}
French	S0	$b_{\text{ef}} = 2a + 2b_x + b_y$
Dutch	S0	$b_{\text{ef}} = 2a + b_x$
MC2010	S0*	$b_{\text{ef}} = 2a + 2b_x + b_y - 2d$
German	S0, S0*	$b_{\text{ef}} = t + 0.3(a + b_x/2)$
Swedish	SI $(d/2)$	$b_{\text{ef}} = \max(7d + b_x + t; 10d + 1.3y)$

The analysis in Muñoz et al. (2023) shows that the geometric assumptions behind most b_{ef} formulations do not directly correlate with the actual shear stress distribution. Moreover, the threshold width approach, which assumes that b_{ef} corresponds to the width beyond which capacity stabilizes, was found to be unreliable. Instead, linear-elastic FE simulations are recommended for practical design, as they provide direct shear force distributions and consider boundary conditions more effectively than conventional hand calculations. An additional factor is the influence of an edge beam. The presence of an edge beam significantly alters load distribution and increases load capacity up to 20% (Muñoz, 2020).

In Sweden, the smeared method is used to evaluate shear failure in a critical section with an effective width, which according to Trafikverket (2023a) is given by:

$$b_{ef} = \max \begin{Bmatrix} 7d + b + t \\ 10d + 1.3y_{cs} \end{Bmatrix} \tag{3.1}$$

where d is the effective depth at the critical section, b the width of load and t the thickness of the surface. According to Pacoste et al. (2012), the critical section is located at a distance of $y_{\text{cs}} = \frac{c+d}{2}$ from the load. The shear force within the effective width at the critical section is smeared to a constant shear stress across this width.

3.1.2 Shear capacity

To evaluate the shear and punching shear capacity of a section, a local resistance model is commonly used, given by EN 1992-1-1 as:

$$V_{Rd,c} = C_{Rd,c} \cdot k \cdot (100 \cdot \rho_l \cdot f_{ck})^{\frac{1}{3}} \cdot b_w \cdot d \geq 0.035 \cdot k^{\frac{3}{2}} \cdot f_{ck}^{\frac{1}{2}} \cdot b_w \cdot d \tag{3.2}$$

where:

$$C_{Rd,c} = \frac{0.18}{\gamma_c}$$

$$k = 1 + \sqrt{\frac{200}{d}} \leq 2.0$$

$$\rho_l = \frac{A_{sl}}{b_w \cdot d} \leq 0.02 \text{ For shear capacity}$$

$$\rho_l = \sqrt{\rho_{ly} \cdot \rho_{lz}} \leq 0.02 \text{ For punching shear capacity}$$

where ρ_{ly} and ρ_{lz} is the reinforcement ratio in the longitudinal and transversal direction respectively and b_w is the width which is considered as 1 meter. The method to relate the capacity to the effective width is described in Section 4.3.

3.1.3 Moment capacity

The moment capacity of a section is checked by using ordinary beam theory, considering moment equilibrium around the tensile reinforcement. The capacity is given as:

$$M_{Rd} = \alpha \cdot f_{cd} \cdot b_w \cdot x(d - \beta \cdot x) + \sigma'_s \cdot A'_{sl}(d - d') \tag{3.3}$$

where α and β is factors that is used to describe the stress block and x is the depth of the natural axis which is given by:

$$\alpha \cdot f_{cd} \cdot b_w \cdot x + \sigma'_s \cdot A'_{sl} = \sigma_s \cdot A_{sl} \tag{3.4}$$

3.2 Level 2 - Linear analysis

Although RC structures exhibit significant non-linear behaviour due to cracking and reinforcement yielding, linear FE models are widely used for their simplicity, computational efficiency, and the ability to apply the principle of superposition when evaluating multiple load cases. Since linear models operate under the assumption of linear elastic material behaviour, effects such as cracking cannot be explicitly captured as in non-linear models, and the linear analysis is based on the assumption that the section has

a linear relationship between moment and curvature. However, according to Pacoste et al. (2012), this simplification can be justified in ultimate limit state analyses due to the good plastic deformability of RC slabs.

Linear FE models rely on several simplifications, which often lead to unrealistic concentrations of cross-sectional moments and shear forces (Pacoste et al., 2012). The modelling of support conditions is particularly influential, as simplified support models can significantly affect the distribution of internal forces and moments.

The effective width is used for linear FE models in a similar way as in level 1. Depending on the position of the critical section, the effective width for shear can be determined as:

$$b_{\text{ef,max}} = \max \begin{Bmatrix} 7d + b + t \\ 10d + 1.3y_{cs} \end{Bmatrix} \quad \text{for } y = 0 \tag{3.5}$$

$$b_{\text{ef,min}} = \min \begin{Bmatrix} 7d + b + t \\ 10d + 1.3y_{cs} \end{Bmatrix} \quad \text{for } y = y_{\text{max}} \tag{3.6}$$

where the definition of y can be seen in Figure 3.2. If the critical section is located between $y = 0$ and $y = y_{max}$, linear interpolation of the effective widths can be used.

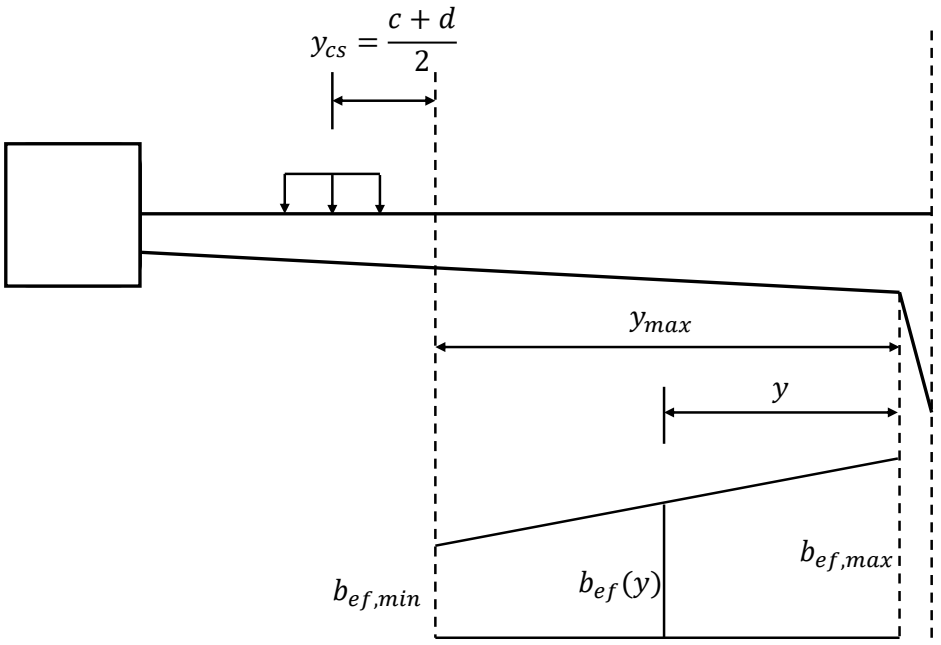

Figure 3.2: Effective widths for shear forces, adapted from Pacoste et al. (2012).

Additionally, Pacoste et al. (2012) gives the effective width when considering moment as:

$$b_{ef} = \min \begin{Bmatrix} 7d + b + t \\ 10d + 1.3y_{cs} \end{Bmatrix} \tag{3.7}$$

3.2.1 Element types

In linear FE-models, beam elements are commonly used to model slender structural components that primarily resist forces through axial, bending, torsional, and shear behaviour. These elements are formulated as one-dimensional representations with cross-sectional properties that determine their stiffness and load-bearing capacity. Because they only require discretization along their length, beam elements are highly computationally efficient, making them well-suited for modelling structural members such as girders and bridge edge beams.

Since beam elements are one-dimensional, they do not inherently capture out-of-plane deformations or local effects. Additionally, beam elements typically assume a uniform stress distribution across the cross-section, which might not always be accurate, especially in cases where shear lag or localized effects influence the response.

Shell elements are commonly used to model thin-walled structural components, such as slabs and plates. They efficiently capture both membrane and bending behaviour, making them well-suited for structures with a high length-to-thickness ratio. Shells are formulated as two-dimensional surfaces with an assigned thickness, allowing them to represent large areas with relatively few elements.

However, shell elements are not well-suited for modelling localized stress concentrations, such as those occurring at connections between the overhang and the main bridge deck or at abrupt changes in geometry. These effects may require refined meshing or the inclusion of solid elements in critical regions.

Davidsson (2003) describes how shell elements in a linear analysis do not provide a good response in direct connections with point loads due to unrealistic stress concentrations. When a point load or a concentrated force is applied to a shell model, very high local stress concentrations occur at the node where the load is applied. However, these concentrations are purely numerical artifacts and do not physically occur in real structures, as concrete cracks and redistributes the forces through plastic deformations and local load spreading, preventing such extreme stress peaks. To obtain more accurate results, Davidsson (2003) recommends avoiding point loads, refining the mesh, and using solid (continuum) elements in critical regions to better capture three-dimensional stress effects near concentrated loads.

3.2.2 Mesh

The mesh size plays a crucial role in ensuring the accuracy and efficiency of an FE model. A fine mesh provides better resolution of stress distributions and deformations but increases computational cost. Conversely, a coarse mesh improves computational efficiency but may compromise accuracy, particularly in regions with high stress gradients or complex geometry.

To achieve an optimal balance, a mesh convergence analysis is performed. This involves systematically refining the mesh and comparing key results, such as displacements, internal forces, and stresses, until further refinement produces negligible changes. By doing so, the model ensures sufficient accuracy without unnecessary computational expense.

Additionally, adaptive meshing techniques or locally refined meshes can be employed in areas of interest, such as around stress concentrations or abrupt geometric transitions,

to enhance accuracy while maintaining efficiency in less critical regions.

It is recommended to ensure that the mesh is sufficiently dense in support regions and in areas subjected to high concentrated loads, as these regions are prone to unrealistic stress peaks (Plos et al., 2021).

3.2.3 Boundary conditions

The support conditions in a FE model play a crucial role in determining the accuracy of the analysis results. Therefore, careful consideration must be given to their modelling. Translations and rotations are often simplified as either completely free or fully fixed. However, in reality, supports typically exhibit some degree of flexibility. To improve accuracy, elastic support conditions can be introduced in the FE model, better reflecting real-world behaviour (Plos et al., 2021). Additionally, if the supports are concentrated at a few nodes or a single node, singularity issues may arise. Therefore, the selection of result sections becomes crucial to ensure accurate analysis, or the modelling is made such that singularities are avoided (Pacoste et al., 2012). In the case of cantilever slabs, the stiffness of the support plays a significant role in this selection, as main girders made of concrete or steel provide vastly different support stiffnesses. For concrete beams, the moment should typically be evaluated at the edge of the beam, where the connection to the slab is relatively stiff. In contrast, for steel beams, the lower stiffness of the flange compared to the web may necessitate placing the result section directly above the web to obtain a more accurate representation of the moment distribution.

3.3 Level 3-5 - Non-linear analysis

RC structures exhibit highly non-linear behaviour due to a combination of factors, including cracking, material non-linearity, and bond stress-slip effects between concrete and reinforcement (Plos, 2000). To accurately capture this complex response, the use of non-linear FE models is essential, as they provide a more realistic representation of key phenomena such as crack propagation, stress redistribution, and the interaction between reinforcement and surrounding concrete. As a result, non-linear FE models can reveal a higher capacity compared to linear FE models and conventional hand calculations (Plos et al., 2021).

In this context, the non-linearity refers specifically to the material behaviour. The geometry is assumed to remain linear (small deformations) and the boundary conditions are considered fixed throughout the analysis, thus the models do not account for non-linearity for the geometry or boundary conditions.

Several aspects need to be considered carefully, including material models and element types, since these choices will impact the accuracy of the response. However, there is always a trade-off between achieving high accuracy and maintaining computational efficiency. A more detailed model, using complex material models and fine meshing, can improve accuracy but can also lead to excessive computation times.

In the multi-level assessment, Levels 3 to 5 involve non-linear analysis with increasing complexity. Level 3 employs shell elements to capture global structural behaviour while maintaining computational efficiency. Level 4 enhances accuracy by using continuum elements with fully bonded reinforcement, allowing for a more detailed representation of stress distribution. Finally, Level 5 further refines the model by incorporating bond stress-slip effects, providing the most realistic simulation of reinforcement-concrete in-

teraction.

3.3.1 Element types

Concrete is typically modelled as either structural or continuum elements. Structural elements, such as beam and shell elements, are typically used for modelling large-scale structures where the primary focus is on global behaviour rather than localized effects. These elements provide computational efficiency while still capturing essential load distribution and deformation characteristics, but they are unable to model shear failure (Hendriks et al., 2017). In contrast, continuum (solid) elements are employed when a more detailed representation of the structure's behaviour is required. These elements allow for a finer analysis of stress distributions and crack propagation, making them essential for capturing localized failure mechanisms and complex interactions between the materials. Although solid elements consists of fewer Degrees of freedom (DOF) per node compared to shell elements, as shown in Figure 3.3, they are more computationally demanding since they require significantly more nodes and therefore also more DOFs. As a result, shell models offer faster simulations while maintaining accurate global structural behaviour.

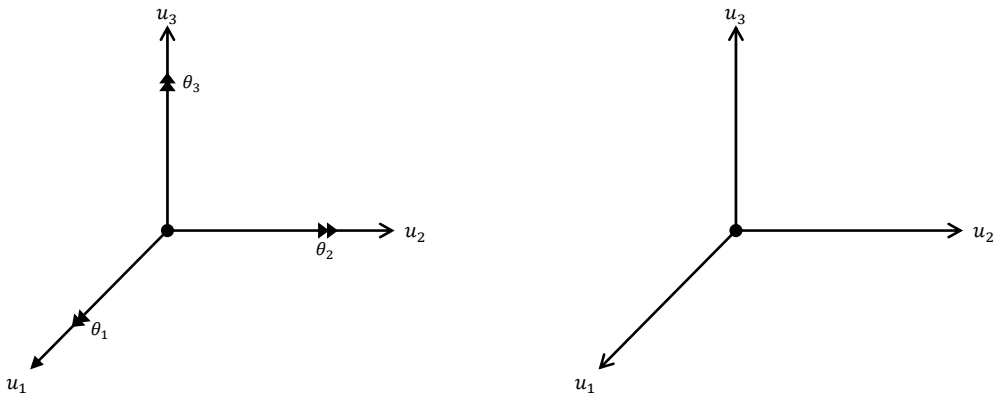

(a) Shell **(b)** Solid

Figure 3.3: DOF for shell and solid elements

Cracks in non-linear FE analysis often align with element edges due to numerical constraints, leading to locking effects that can distort the structural response. To mitigate this, triangular (for 2D models) and tetrahedral (for 3D models) elements are recommended over quadrilateral and hexahedral elements, as they allow cracks to propagate in a more natural manner (Plos et al., 2021).

3.3.2 Reinforcement modelling

Reinforcement in finite element models can be represented in three main ways: embedded reinforcement, 1D bars, or 3D bars (Plos, 2000). Embedded reinforcement is defined within the concrete elements, meaning it does not have its own degrees of freedom. Instead, its strain is derived from the surrounding concrete, providing additional stiffness in the longitudinal direction without requiring a separate mesh. 1D bars are typically modelled using truss or beam elements and are connected to the concrete

via line interface or spring elements. This setup allows for the explicit inclusion of bond stress-slip behaviour, which has a significant impact on the structural response, particularly in cracked regions (Plos et al., 2021). 3D bars, in contrast, are modelled with continuum elements and interact with the surrounding concrete through surface interface elements. Here, the bond stress-slip relationship is not predefined but instead emerges as an output from the analysis, providing a more detailed representation of the reinforcement-concrete interaction.

Bond failure in RC structures can generally be classified into two main types: pull-out failure and splitting failure. Figure 2.4 shows the stress displacement ratio for the failure modes.

Pull-out failure occurs when the bond between the reinforcement bar and the surrounding concrete fails, causing the bar to slide out along its length. In this case, the surrounding concrete remains relatively undisturbed, and the failure typically exhibits ductile behaviour. Pull-out failure is more common in bars with smaller diameters and well-defined ribs, which improve mechanical interlock and bond strength.

Splitting failure, on the other hand, happens when the bond between the bar and concrete remains intact, but the surrounding concrete fails due to radial tensile stresses. These stresses cause longitudinal cracks along the bar, eventually leading to the concrete splitting apart, often forming a wedge-shaped or conical fracture zone around the reinforcement. Splitting failure is generally brittle and is more likely to occur when the concrete cover is thin or when there is insufficient confinement.

3.3.3 Concrete in tension and fracture energy

When concrete is subjected to tensile loading, microcracks form at local weak points within the material. As the tensile load increases, these microcracks begin to coalesce, creating a localized fracture process zone where the material progressively softens. This localization marks the onset of significant stiffness degradation, as tensile stresses can no longer be sustained uniformly across the specimen. After reaching the peak tensile strength, the stress within the fracture zone decreases as the crack opening displacement increases. The material outside the fracture zone unloads, while the localized region continues to deform until full separation occurs. At this stage, no further stress can be transferred across the crack, and the structural integrity depends entirely on reinforcement or other load-carrying mechanisms (Plos, 2000).

Fracture energy is a fundamental material property that significantly influences the modelling of cracking behaviour in non-linear FE analysis of RC structures. Various methods are available to estimate the fracture energy in tension. One commonly used approach is provided in Model Code 90 (CEB-FIP, 1993) and is expressed as:

$$G_F = G_{F0} \left(\frac{f_{cm}}{f_{cmo}} \right)^{0.7} \tag{3.8}$$

where f_{cmo} is a reference value of 10 MPa and G_{F0} the base value of fracture energy. Figure 3.4 illustrates the relationship between tensile stress and crack opening displacement, typically represented by a softening curve. The area under this curve corresponds to the fracture energy (G_F), which represents the energy required to propagate a unit area of crack. Fracture energy governs the post-cracking tensile response of concrete and directly influences crack widths, stiffness degradation, and energy dissipation in

non-linear analyses.

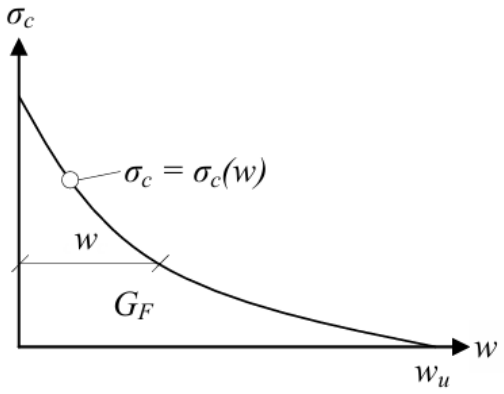

Figure 3.4: Definition of fracture energy (Plos et al., 2021)

3.3.4 Crack modelling

For concrete, it is crucial to include both crack and plasticity models to accurately represent its non-linear behaviour, in addition to the linear elastic behaviour prior to cracking. Crack models, based on fracture mechanics, are typically categorized into three approaches: the discrete, smeared, and embedded crack models (Plos, 2000). While all three approaches describe crack formation as discontinuities, they differ in how these discontinuities are represented. The discrete crack approach models cracks explicitly at the interfaces between elements, requiring special interface elements and prior knowledge of the expected crack positions. The smeared crack approach distributes the discontinuity over the continuum elements, eliminating the need for additional interface elements, but it relies on predefined parameters such as the crack band width to ensure accurate results. Lastly, the embedded crack approach models discontinuities within the elements themselves, describing the cracks as discontinuities, though it also requires specialized elements.

3.3.5 Boundary conditions

The boundary conditions in the non-linear models are the same as those applied in the linear analyses, as described in Section 3.2.3.However, it should be noted that boundary conditions in non-linear analyses can themselves be non-linear. However, such effects are not considered in this report, as all supports are assumed to behave linearly throughout the analysis.

3.3.6 Iteration and convergence

When conducting non-linear analyses, a common approach is the incremental iterative solution method, which uses iterations to establish equilibrium throughout the analysis (Plos, 2000). The incremental iterative solution method must incorporate an iterative scheme to ensure equilibrium within each increment. These schemes rely on achieving convergence by incorporating a stiffness matrix during each iteration. Force, displacement and energy are commonly used measurements to ensure convergence (Plos et al., 2021). The Newton-Raphson method and its modified variant are commonly used for this purpose. In the standard Newton-Raphson method, the stiffness matrix is updated

at every iteration, ensuring rapid convergence but at a higher computational cost. In contrast, the modified Newton-Raphson method updates the stiffness matrix only once per increment, reducing computational effort but potentially requiring more iterations to reach convergence. The quasi-Newton method iteratively updates an approximate inverse of the stiffness matrix, allowing for a faster and more efficient convergence.

The incremental iterative solution method can be implemented using different load-stepping strategies, primarily load-controlled, displacement-controlled, and arc-length incrementation. Load-controlled and displacement-controlled strategies are relatively straightforward, incrementing either the applied load or the prescribed displacement in each step. However, they may struggle when the structure exhibits snap-through or snap-back behaviour (shown in Figure 3.5), as these phenomenons may not be accurately captured due to the non-linear response (Plos, 2000). The arc-length method provides a more advanced alternative by controlling the total length of the load displacement path, enabling the solution to follow equilibrium and capturing possible snap-through or snap-back behaviours.

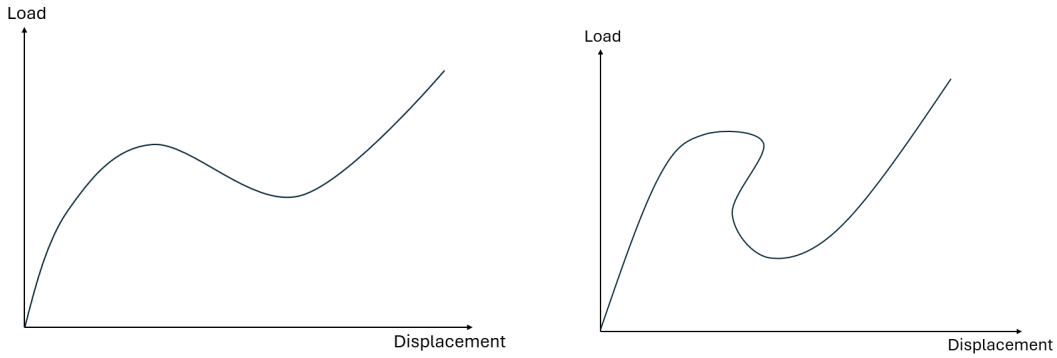

(a) Snap-through **(b)** Snap-back

Figure 3.5: Load-displacement relationship for snap-through and snap-back behaviour

3.3.7 Mesh

Convergence is not only important for each increment, it must also be evaluated for the global response to ensure a sufficiently refined mesh and accurate results. The finite element discretization plays a crucial role in the accuracy of the analysis (Hendriks et al., 2017). While discretization checks can be performed within the software, conducting comparative analyses with different mesh refinements is essential to ensure convergence and accuracy, particularly in regions with high stress gradients (Plos et al., 2021).

3.3.8 Safety format

To ensure the reliability of structural assessments, appropriate safety formats must be applied when evaluating RC structures. Safety formats ensure that the target reliability level is met. Various approaches exist for non-linear FE analyses of reinforced concrete, which can be broadly categorized into full probabilistic analysis, partial safety factor (PSF) methods and global safety factor (GSF) methods (Plos et al., 2021).

The full probabilistic analysis is usually the most correct, as it accounts for all uncertainties explicitly. However, it is computationally demanding, particularly for non-linear

analyses due to the need for detailed knowledge about the probabilistic parameters.

The PSF method is the most commonly used approach in Eurocode and is recommended by Plos et al. (2021) for linear structural analysis, as it allows for the superposition of load combinations. Consequently, the PSF method is recommended for assessment Levels I and II. However, for non-linear analyses, this method is generally not appropriate, as it is based on sectional verification rather than global structural resistance.

For non-linear analyses, GSF methods are generally preferred and are described by:

$$F_d \leq R_d \tag{3.9}$$
$$R_d = \frac{R_m}{\gamma_R^* \cdot \gamma_{Rd}}$$

where F_d is the design value of actions, R_d and R_m is the design value and mean value respectively of the resistance for the structure, γ_R^* is the global resistance factor and γ_{Rd} the model uncertainty factor. The GSF methods apply a single safety factor to the total structural resistance, making them more suitable for capturing the complex interactions within RC structures. According to Plos et al. (2021), two main global safety formats are commonly used: the global resistance factor method (GRFm) and the Estimate of Coefficient of Variation (ECOV) method.

The GRFm adopts a fixed value of $\gamma_R^* \cdot \gamma_{Rd} = 1.27$, simplifying the verification process since it requires only a single non-linear analysis per load combination. This approach is practical for failure modes with low modelling uncertainty, such as bending-dominated failure in beams and frames, as it applies a uniform safety factor irrespective of whether failure is controlled by steel or concrete. However, this method is less suitable for reinforced concrete slabs, where modelling uncertainties are typically greater due to complex failure mechanisms like shear and punching shear. The method uses mean material values to calculate the mean value of the resistance, by using:

$$f_{cm,GRF} = \alpha_{cc} \cdot 1.1 \cdot \frac{\gamma_s}{\gamma_c} \cdot f_{ck} \tag{3.10}$$
$$f_{ctm,GRF} = \alpha_{ct} \cdot 1.1 \cdot \frac{\gamma_s}{\gamma_c} \cdot f_{ctk} \tag{3.11}$$
$$f_{ym,GRF} = 1.1 \cdot f_{yk} \tag{3.12}$$

where α_{cc} and α_{ct} is set to 1, γ_c is set to 1.5 and γ_s to 1.15 which are all given in EN 1992-2.

In contrast, the ECOV method provides a more refined assessment by explicitly considering variability in material properties. This method requires two non-linear analyses, one based on mean material properties and another using characteristic values representing lower-bound material strengths (Cervenka et al., 2007). The global resistance factor introduced in equation 3.9 can for the ECOV method be determined by:

$$\gamma_R^* = \exp(\alpha_R \cdot \beta_R \cdot V_R) \tag{3.13}$$

where α_R is the sensitivity factor and β_R is the reliability factor. Also, V_R is the Coefficient of Variation (COV) which establishes a probabilistic distribution based on characteristic and mean material values and is determined by:

$$V_R = \frac{1}{1.65} \cdot \ln(\frac{R_m}{R_k}) \tag{3.14}$$

where R_m is the resistance for the structure considering mean values and R_k is the resistance for the structure considering characteristic values. The ECOV method better accounts for uncertainty than the standard Eurocode approach, making it more suitable for cases where structural behaviour is difficult to predict. However, the need for multiple analyses per load case increases computational demands.

3.3.9 Load history

When a RC model is loaded beyond its linear elastic range, it reaches its yield surface and begins to undergo plastic deformations. If the structure is subsequently unloaded after yielding, the material behaviour becomes path-dependent, as the yield surface may shift due to inelastic strains and cracks (Plos, 2000), see Figure 3.6. This phenomenon is often associated with the Bauschinger effect, where the material exhibits reduced yield strength in the reverse loading direction following prior plastic deformation (Plos, 2000). As a result, prior load history can influence the stiffness and force distribution within the structure. Therefore, modelling previous loading history can lead to a different structural response compared to an initially unloaded and undamaged (uncracked) condition.

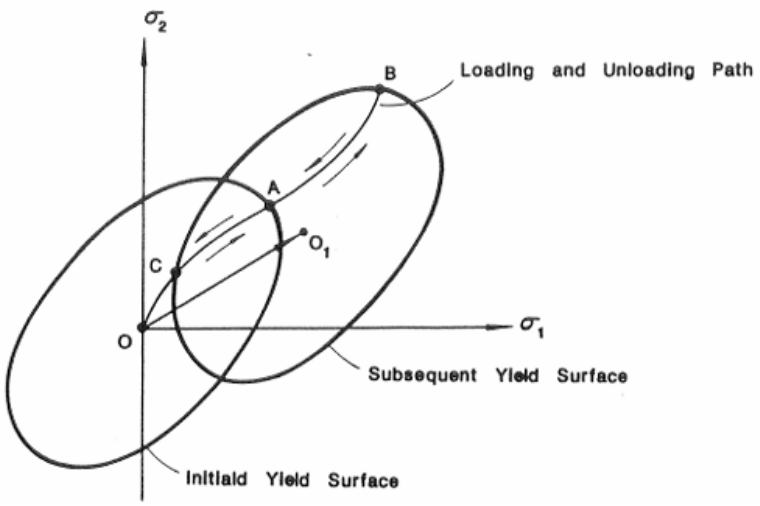

Figure 3.6: Illustration of yield surface movement due to prior loading and unloading from Plos (2000). The diagram shows initial yield surface (O $\rightarrow$ A) and how the loading unloading (A $\rightarrow$ B) lead to a shifted yield surface.

When assessing the load-carrying capacity of RC structures through non-linear analysis, the initial assumption often considers the structure to be uncracked and undamaged before loading is applied. However, in service conditions, prior cracking and accumulated damage can significantly affect both the load distribution and structural capacity. Therefore, to model a realistic representation of the structural response the history of previous applied loads needs to be account for (Plos et al., 2021).

In a non-linear analysis, the structure is subjected to progressively increasing loads to capture its behaviour under different loading conditions. Non-linear effects such as cracking and plastic deformations influence how the structure reacts to additional loads. Consequently, the response becomes history-dependent, meaning that the resistance and deformation pattern vary depending on the sequence of applied loads. This sensitivity

to the load path is not explicitly covered in current design standards and codes (Plos et al., 2021).

To achieve a more realistic simulation, permanent loads should be applied first in the model, as they contribute to the initial stress state and potential early-stage cracking. Subsequent load increments, such as variable live loads, temperature effects, and imposed deformations, should then be introduced in a sequence that reflects real-world conditions. This ensures that the accumulated effects of prior loading, including cracking patterns and redistribution of internal forces, are appropriately captured in the analysis (Plos et al., 2021).

Furthermore, in cases where deterioration mechanisms, such as reinforcement corrosion or frost-induced damage, are considered, their progressive impact on material properties and structural stiffness should be incorporated before applying service loads. This approach aligns with advanced assessment strategies that utilize multi-level evaluation techniques, as discussed in (Plos et al., 2021), to enhance the reliability of non-linear FE analyses.

4 Method

This chapter outlines the methodology applied to the hand-calculations as well as the linear and non-linear FE modelling that was carried out. The approach is based on the recommendations by Plos et al. (2017), as discussed in Chapter 3, modified to suit the specific conditions and objectives of this study. Several geometries have been examined to facilitate comparisons across different assessment levels, the geometries are presented in this chapter.

4.1 Parametric study

The geometry shown in Figure 4.1 has been used as the base geometry, as it represents a typical design commonly found in cantilever slabs of bridges. In Figure 4.2 the reinforcement layout of the base geometry is also shown. Additionally, a surfacing thickness of 100 mm has been considered in the calculations with a unit weight of 22 kN/m^3.

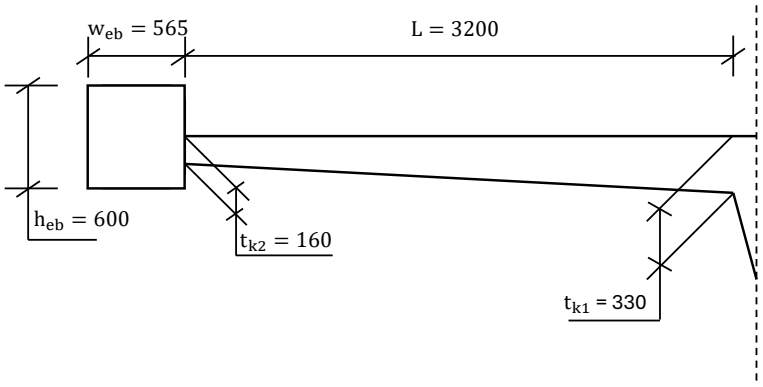

Figure 4.1: Base geometry of the cantilever slab.

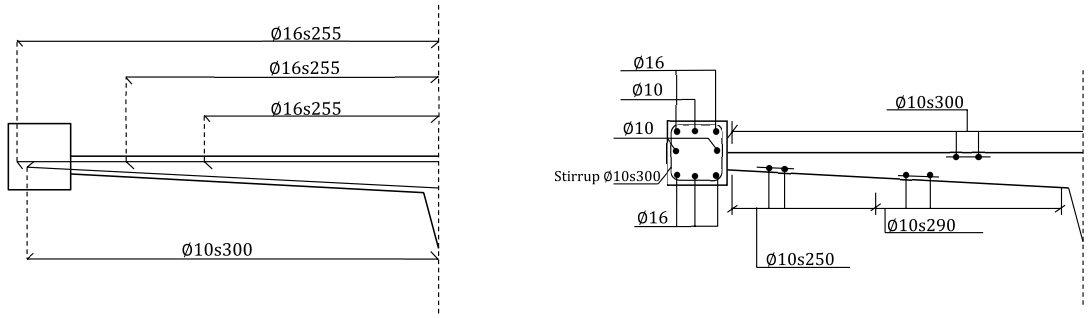

(a) Transversal reinforcement **(b)** Longitudinal reinforcement

Figure 4.2: Reinforcement layout of the base geometry.

Based on this base geometry, several modifications have been introduced to create a set of cases for analysis. Each case is based on the original base geometry, and only the modification described for that specific case is applied. The variations are not cumulative; that is, in each case, only one parameter is changed compared to the base geometry.

The variations include the following cases:

- **Ref**
  Base geometry according to Figure 4.1.
- **NoEdge**
  Edge beam removed.
- **tConst**
  Constant thickness of the slab: 0.25 m.
- **L4m**
  Length of the slab increased to 4 m.
- **L2m**
  Length of the slab decreased to 2 m.
- **t+0.1**
  Thickness of the slab increased by 0.1 m.

Table 4.1 summarizes the geometric parameters used in each case. The reinforcement layout remains unchanged across all cases, except for the L4m case, where the increased span necessitates a higher reinforcement ratio.

Table 4.1: Geometric parameters for each case.

Case	**Ref**	**NoEdge**	**tConst**	**L4m**	**L2m**	**t+0.1**
Height of edge beam, h_{eb} [mm]	600	-	600	600	600	600
Width of edge beam, w_{eb} [mm]	565	-	565	565	565	565
Length of cantilever span, L [m]	3.2	3.2	3.2	4.0	2.0	3.2
Thickness of slab edge, t_{k2} [mm]	160	160	250	160	160	260
Thickness of slab at root, t_{k1} [mm]	330	330	250	375	265	430

The main objective is to evaluate how variations in key geometric parameters affect the structural behaviour of the cantilever slab, particularly in terms of load distribution and force paths at different assessment levels. The objective has thus not been to conduct a full parametric study by exploring all possible geometric cases.

4.2 Material parameters

The material parameters used for the calculations and at different assessment levels are presented in Table 4.2.

Table 4.2: Material parameters for concrete and reinforcement steel. Subscript GRF indicates the parameters used for the safety format GRF.

Material Parameter	Value
Concrete	
Mean compressive strength, f_{cm} [MPa]	43.5
Characteristic compressive strength, f_{ck} [MPa]	35.5
Design compressive strength, f_{cd} [MPa]	23.7
Mean compressive strength GRF, $f_{cm,GRF}$ [MPa]	29.9
Characteristic tensile strength, f_{ctk} [MPa]	2.25
Mean tensile strength GRF, $f_{ctm,GRF}$ [MPa]	1.90
Modulus of elasticity, E_{cm} [GPa]	34
Density including reinforcement, ρ_c [kg/m^3]	2500
Tensile Fracture energy GRF, $G_{F,GRF}$ [N/m]	64.6
Poisson's ratio, ν	0.2
Maximum aggregate size [mm]	16
Reinforcement Steel	
Yield strength, f_{yk} [MPa]	620
Design yield strength, f_{yd} [MPa]	539
Mean yield strength GRF, $f_{ym,GRF}$ [MPa]	682
Modulus of elasticity, E_s [GPa]	200

4.3 Level 1 - Simplified methods

In conventional hand calculations, the cantilever is treated as a one-way slab, divided into 1-meter-wide strips. Each strip is analysed as an independent beam, where applied loads are distributed over an effective width, accounting for the load dispersion through the slab. The strips are analysed using beam theory, considering bending moments and shear forces.

To facilitate the calculations, a Python script was developed to determine the the maximum load for all load cases and geometries. Appendix A presents calculations in Mathcad (PTC, 2025), providing an example for one specific load case based on the base geometry.

4.3.1 Critical sections

For shear, the critical sections considered is located at 0.5d from the perimeter of each wheel pair, as stated by Pacoste et al. (2012). The critical section for moment, on the other hand, is located at the support. These definitions are illustrated in Figure 4.3.

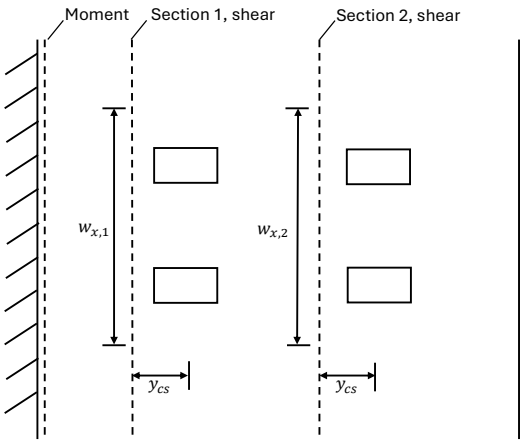

Figure 4.3: Definition of critical sections for shear and moment.

4.3.2 Load cases and distribution

The load cases used in the calculations are based on reference vehicles (*typfordon*) from Trafikverket (2023a). The loads are applied as concentrated forces, each acting as an axle load in the longitudinal direction, shown in Figure 4.4. The load case names are the ones used for the *typfordon*, and these load cases have been modified to only include the concentrated loads. Their magnitudes are expressed in terms of the A-value for load csae a), and B-value for load cases b)-n).

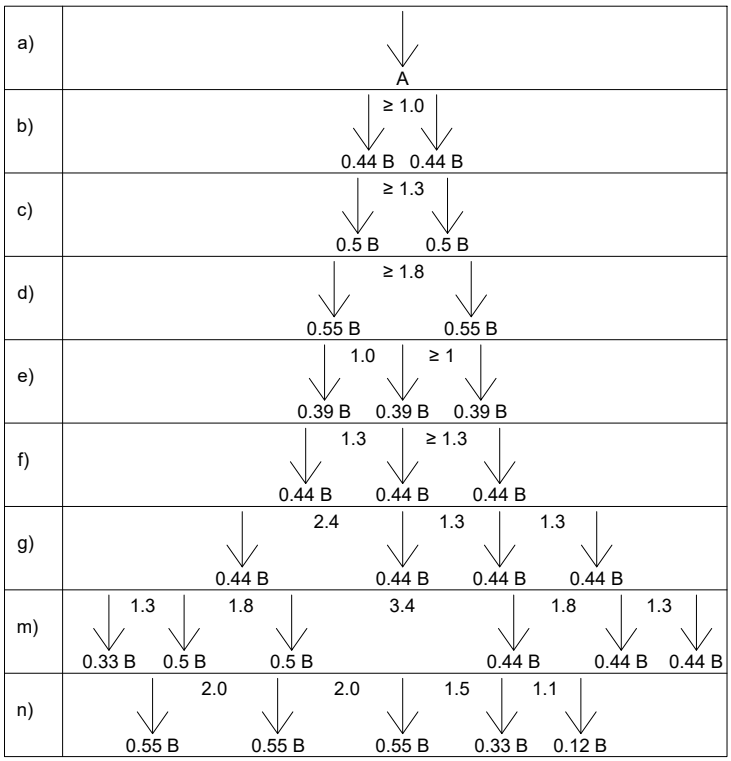

Figure 4.4: Load cases considered with concentrated loads from reference vehicles, *Typfordon*, adapted from Trafikverket (2023a). Each concentrated load represents an axle load and their magnitudes is given below the loads and distance in meters between.

Each point load are distributed as concentrated loads with dimensions 0.2 m in the longitudinal direction and 0.3 m in the transverse direction. The loads are positioned in the middle of a 3 m wide lane, with a centre distance between the wheels of a wheel pair ranging from 1.7 to 2.3 m. However, for the calculations in this report, only a centre distance of 1.7 m has been considered to limit the amount of analyses.

For each load case, the total force is smeared over the total effective width to determine the shear and moment in the critical sections. In cases where the effective widths of different point loads overlap, Figure 4.5 provides guidance for handling the overlap.

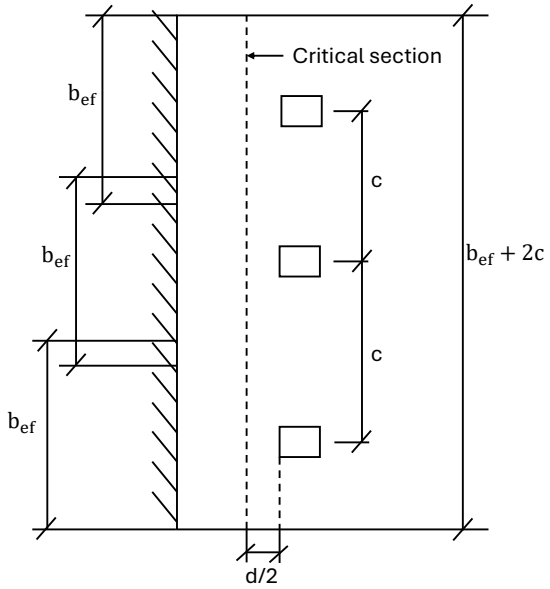

Figure 4.5: Example of effective width for several point loads in close proximity, total effective width is $b_{\text{ef}} + 2c$, adapted from Trafikverket (2023a).

4.3.3 Shear capacity calculation

For each load case, the maximum A and B values has been calculated for shear, punching shear and bending moment separately. For shear, the capacity of a section is determined with equation 3.2 and compared with the shear in the section induced by the self-weight and loads. The shear in the critical sections is determined by:

$$V_{Ed} = \chi_{Typf.V} \cdot \frac{B}{100} \cdot V \cdot D \cdot \gamma_{traffic} + V_{selfweight} \cdot \gamma_{perm} \tag{4.1}$$

where $\chi_{Typf.V}$ is the distribution factor of the traffic loads, B is used for load cases b-n and A for load case a, V is the shear in the critical section in kN when considering B = 100 kN, $\gamma_{traffic}$ is the load combination factor for traffic in ULS which is set to 1.5, $V_{selfweight}$ is the shear in the critical section induced by the self-weight and D is the dynamic factor which is given by:

$$D = \frac{180 + 8 \cdot (\nu - 10)}{20 + L} [\%] \tag{4.2}$$

where L is the length for dynamic addition and set to the length of the slab and ν is the velocity which is set to 80 km/h.

The distribution factor introduced in equation 4.1 is determined by smearing the total load of each load case over the effective width which was introduced in section 3.1.1 as equation 3.1, which is the Swedish approach.

The objective has been to evaluate each load case in Figure 4.4 and compare the results with those from the FE models. Thus, the aim has not been to identify the governing load case but rather to assess all load cases individually, highlighting their similarities and differences.

4.3.4 Punching shear calculation

The punching shear capacity is calculated using Equation 3.2, which takes into account the reinforcement in both the longitudinal and transverse directions. In accordance with EN 1992-1-1, the effective depth is assumed to be constant along the control perimeter and is determined as:

$$d_{\text{ef}} = \frac{d_y + d_z}{2} \tag{4.3}$$

where d_y and d_z are the effective depths in the transverse and longitudinal directions, respectively. The control perimeter is placed at a distance of $2d$ from the loaded area, as illustrated in Figure 2.9.

The general perimeter definition according to EN 1992-1-1 is used, i.e., a four-sided control perimeter, except in cases where the perimeter intersects a slab edge or support. In such cases, adjustments are made accordingly. If control perimeters overlap due to closely spaced loads, they are evaluated as a combined perimeter. Nevertheless, the resistance is also checked individually for each loaded area, even when perimeters overlap.

4.3.5 Moment capacity calculation

The moment capacity of a section is given by equation 3.3. Similar to equation 4.1 when evaluating shear, the moment induced by self-weight and loads is given by:

$$M_{Ed} = \chi_{Typf.M} \cdot \frac{B}{100} \cdot M \cdot D \cdot \gamma_{traffic} + M_{selfweight} \cdot \gamma_{perm} \tag{4.4}$$

The distribution factor $\chi_{Typf.M}$ in equation 4.4 is determined by the effective width, which is not explicitly defined in the current structural codes but is given by Statens Betongkommitté (1968) as:

$$b_{ef} = \frac{2}{n} \tag{4.5}$$

where:

$$n = \sqrt[4]{\frac{c}{4 \cdot E_{ck} \cdot I_1}}$$

$$c = \frac{3 \cdot E_{ck} \cdot I_2}{\alpha^3}$$

$$I_1 = \frac{h_{eb}^3 \cdot w_{eb} + t_{k2}^3 \cdot (L_k - \alpha)}{12}$$

$$I_2 = \frac{t_{k1}^3}{12}$$

where α is the distance from the support to each wheel and L_k is the length of the cantilever including the edge beam. The equation accounts for the effect of the edge beam by considering two axes when defining the moment of inertia, as shown in Figure 4.6. I_1 represents the moment of inertia considering both the edge beam and the adjacent part of the slab nearest to the outer wheel. I_2 represents the moment of inertia per unit width of the slab.

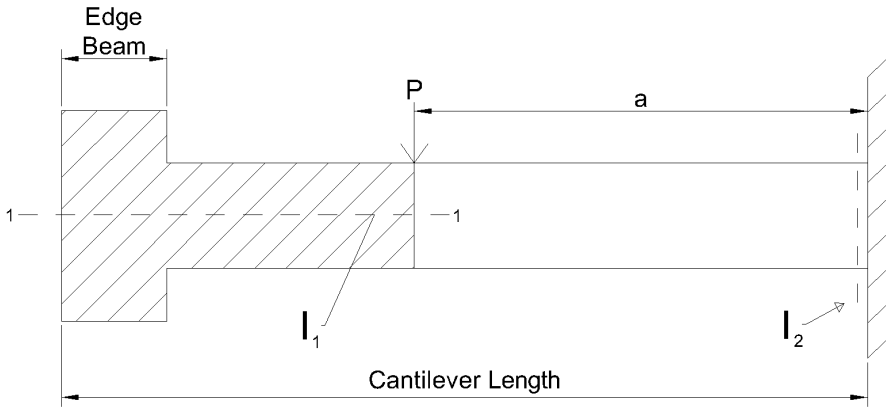

Figure 4.6: Cantilever slab with edge beam subjected to point load, Adopted from Statens Betongkommitté (1968).

4.4 Level 2 - Linear analysis

This section presents the linear FE-analysis carried out to evaluate the load distribution and structural response. The calculations were performed using the software FEM-Design (Strusoft, 2025), following the guidelines outlined by Pacoste et al. (2012).

4.4.1 Modelling approach

The slab was modelled using shell elements, while the edge beam was represented by beam elements. This approach aligns with the theoretical framework described in Section 3.2, ensuring an efficient and accurate representation of the structural behaviour. For all modelled geometries a width of 30 meters was used. The width-to-span ratio is for all geometries larger than the minimum value of 6.1 recommended by Muñoz et al. (2023), in order to ensure the width of the slab does not limit the load distribution. Shell elements with nine nodes were used to capture both bending and membrane action, while beam elements accounted for the axial and flexural stiffness of the edge beam. Since the model was based on a linear analysis, reinforcement was not explicitly included. The base geometry of the model is illustrated in Figure 4.7.

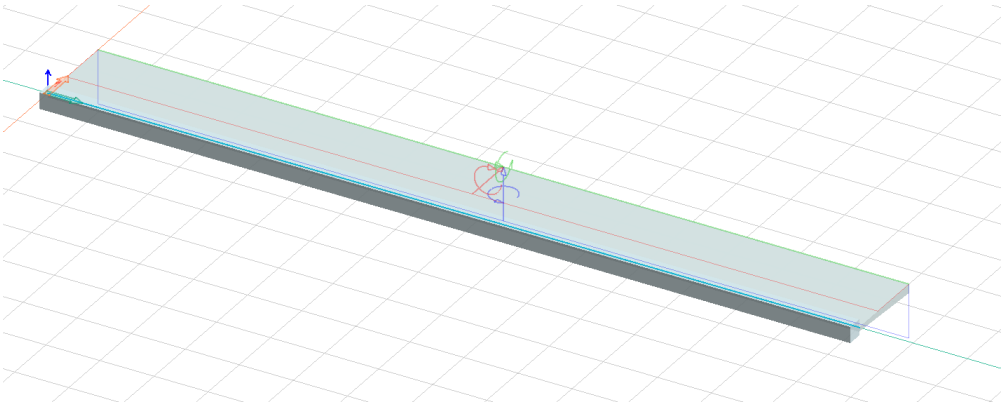

Figure 4.7: Model of the base geometry

To ensure correct load transfer between the slab and the edge beam, a rigid connection was assumed between the shell and beam elements. This assumption was based on the relatively high stiffness of the edge beam compared to the slab thickness, ensuring that deformations remain compatible between the two components. However, localized stress concentrations at the connection could arise due to differences in stiffness, which may affect the force distribution along the slab-edge beam interface. A fully rigid connection has also been modelled at the support, which is also in accordance with Pacoste et al. (2012) guidelines.

4.4.2 Mesh convergence analysis

The mesh used in the linear FE models was a quadrilateral mesh with nine integration points. To ensure stability and accuracy of the model, a mesh convergence analysis was performed. Using load case f), the displacement was evaluated at the point of maximum displacement for different mesh sizes, revealing that convergence was achieved at a mesh size of 0.15 m, as the displacement showed only minor relative changes when the mesh was further refined. However, to improve accuracy in critical regions, a finer mesh size of 0.1 m was used in the final model. The results of the convergence analysis are presented in Figure 4.8.

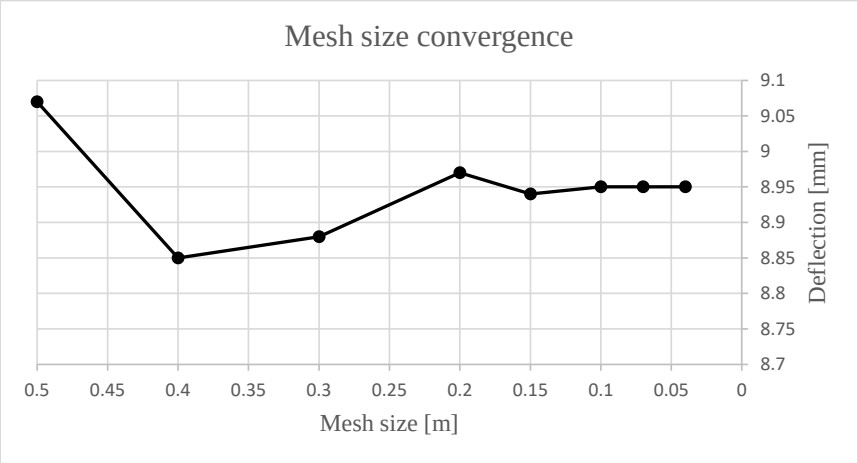

Figure 4.8: Convergence of mesh size, measuring deflection at the tip of the slab.

4.4.3 Load distribution and critical sections

The same critical sections used for the hand calculations were analysed in the FE model, see Section 4.3.1. Shear forces were evaluated at two sections, each at a distance of 0.5d from the applied load, while moment capacity was assessed at the support.

The effective width used in the linear FE-analysis for moment calculations is given in Equation 3.7. Additionally, when considering the effective width for shear, Equation 3.6 is used since the critical section is considered to be located at a distance $y_{cs} = \frac{c+d}{2}$ from the load.

The maximum load is determined using the same approach as in the hand calculations, as described in Equations 4.1 and 4.4. First, the effect of the self-weight is calculated. Then, the effect of a reference load of 100 kN is evaluated separately. This load is gradually increased until the total load effect reaches the structural capacity.

To facilitate the FE modelling process, a Python script has been utilized. This script automates the creation of the slab's geometry, including the edge beam and the fixed support conditions, ensuring consistency and precision in the model. Additionally, it defines and applies the reference loads acting on the structure. The application of the loads to the structure is shown in Figure 4.9.

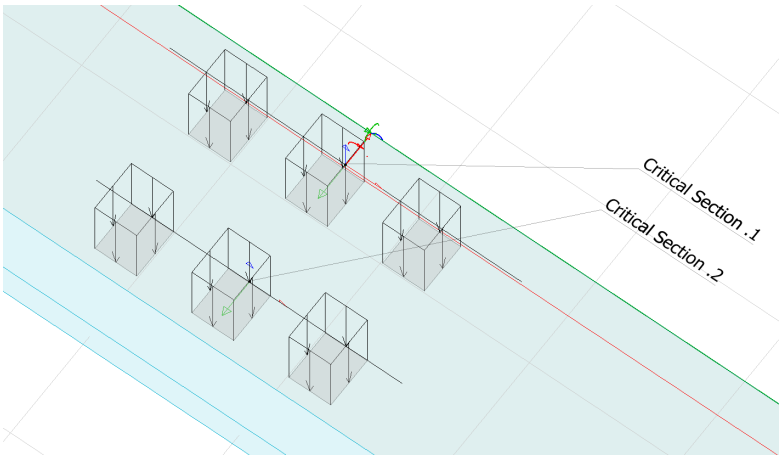

Figure 4.9: Load case f) applied to the base model with the corresponding critical sections for shear forces.

According to Trafikverket (2023a) the load is allowed to be distributed horizontally in the slab with a 1:1 ratio compared to the height to the system line of the slab, as shown in Figure 4.10. The load is distributed both in the longitudinal and transversal direction to better match the real behaviour of the load distribution in the linear FE-analysis. This will increase the load capacity, since the concentrated loads are spread over a wider area. However, the effective width and critical section is calculated from the original width and length of the concentrated loads according to Trafikverket (2023a). For the tapered slabs, the height at the edge is used to determine the location of the system line, which is assumed to be constant across the slab.

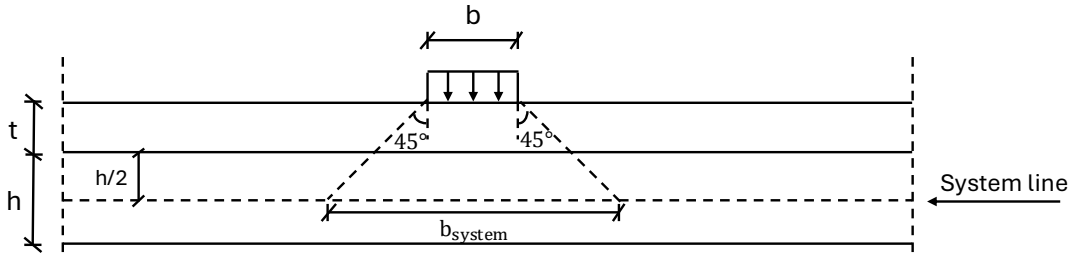

Figure 4.10: Distribution of loads in the slab.

To better capture the behaviour of the RC slab, cracking in the transverse direction has been considered and compared to the uncracked stage. This was done by reducing the Young's modulus by 40% in the transverse direction to account for the reduced stiffness of the cracked slab, in accordance with Trafikverket (2023a).

4.5 Level 3-5 - Non-linear analysis

This section describes the modelling approach used for the non-linear analyses carried out in the software ATENA (Cervenka Consulting, 2025). Two different models has been used, one with shell elements and one with solid elements, along with two different loading procedures, one loaded in ULS to failure directly and one where a Serviceability Limit State (SLS) load is applied at several positions along the cantilever before the loading to failure. The width of the cantilever was 30 meters as for the linear model.

This chapter also outlines the key assumptions made and how these were implemented in the models.

4.5.1 Modelling approach

For the non-linear analysis, two models of the cantilever slab were developed. The first model represents a combination of assessment levels 3 and 4, utilizing both shell and solid elements. The second model corresponds to assessment levels 4 and 5, using only solid elements with embedded reinforcement and bond stress-slip behaviour for critical reinforcement. The motivation for developing two different non-linear models was to enable easier extraction of shear and moment forces at critical sections using shell elements, while also capturing the cantilever's failure behaviour as realistically as possible with solid elements. The two models of the cantilever slab are described as follows:

- **Shell model for the slab**
  The slab is modelled with shell with a layer thickness of 50 mm and a mesh size of 100 mm elements. Smeared reinforcement is used.
  The edge beam is modelled with 4-noded solid tetrahedral elements with mesh size 200 mm and embedded reinforcement.
- **Solid model for the slab**
  The slab and edge beam are modelled with 4-noded solid tetrahedral elements. The slab elements have a general size of 100 mm, refined to 40 mm around areas of applied loads. The edge beam elements are sized at 200 mm.
  A bond stress-slip relationship is applied for the transverse reinforcement in the slab, while the longitudinal reinforcement in both slab and edge beam is fully bonded.

The load distribution, as illustrated in Figure 4.10, is considered in both models. Since solid elements and 3D shell elements are used for the slab, the load spreading is inherently captured within the model. However, the surfacing load is applied as a uniform load at the top of the slab. Therefore, for vehicle wheel loads, the application area was manually adjusted according to a 1:1 spreading ratio.

A mesh sensitivity analysis was carried out to investigate how element size and type influence the results. Both linear and quadratic tetrahedral elements were evaluated. For accurate simulation of localized failure phenomena such as shear failure, a sufficient number of elements and integration points is essential. A coarse mesh of solid elements can artificially stiffen the model, leading to unrealistic behaviour compared to real structures. This effect can be mitigated by refining the mesh, particularly in critical regions such as load introduction areas and near supports. Figure 4.11 shows different load-displacement behaviour for the cantilever when it is subjected to load case a) and the permanent loads. The displacement is measured at the bottom of the edge beam where the deflection is highest.

The computational time was an important consideration, as it was a limiting factor for the mesh refinement. As shown in Figure 4.11, the choice of element type and mesh size influences the global stiffness of the cantilever slab. Shell elements result in a slightly lower stiffness compared to solid elements. Furthermore, models with finer meshes and quadratic elements exhibit a softer load-displacement response and are better able to capture the localized deformation and cracking phenomena compared to coarser, linear

solid element models. However, finer meshes substantially increase computational time.

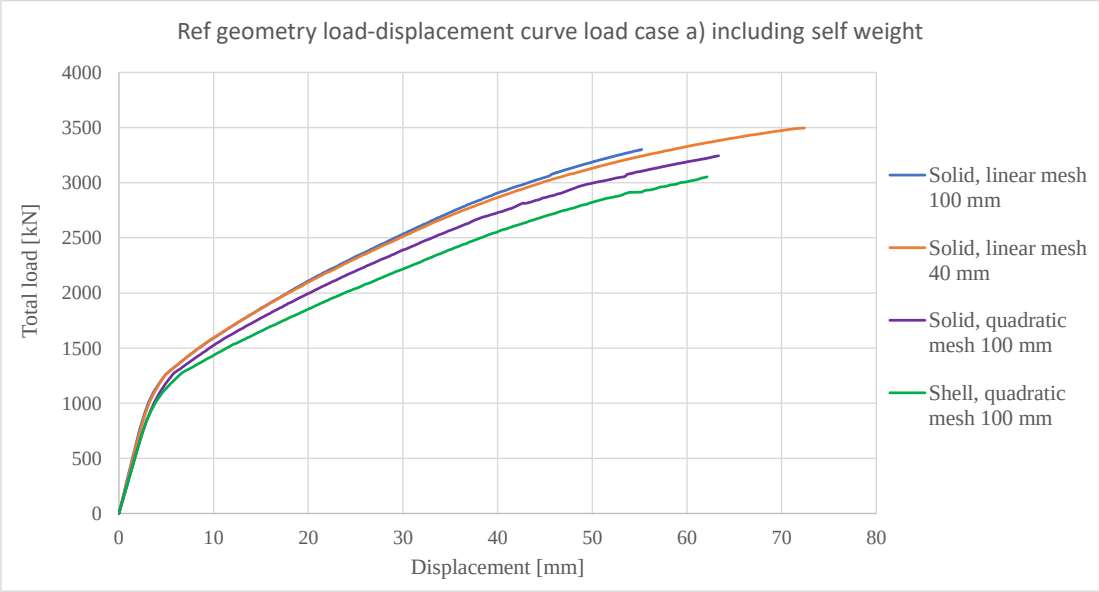

Figure 4.11: Comparison of different mesh densities and types.

The influence of mesh size on the edge beam behaviour can be observed in Figure 4.12. Different mesh densities showed minimal variation in the global load-displacement response, indicating that the chosen mesh size of 200 mm for the edge beam provides a good balance between accuracy and computational efficiency.

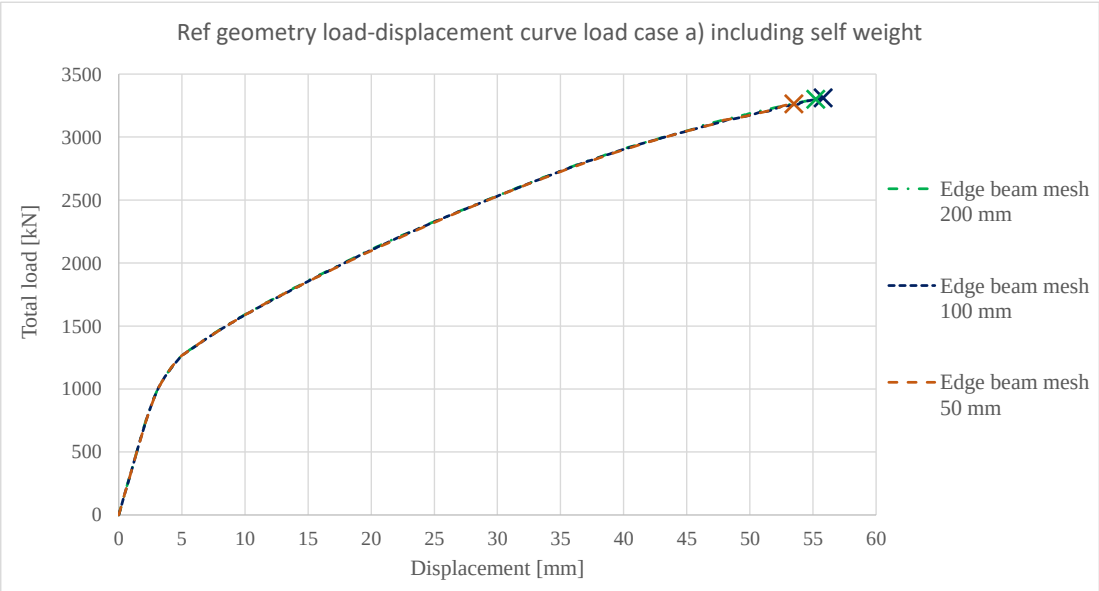

Figure 4.12: Load and displacement for different mesh size of edge beam.

For the shell elements, a mesh size of 0.1 m was used, and two different layer thicknesses, 0.05 m and 0.025 m, were tested. Figure 4.13 presents the total load (including

self-weight and surfacing layer) and displacement of the base geometry subjected to load case (a), representing a single pair of wheels. The results show that reducing the layer thickness from 50 mm to 25 mm did not significantly affect the overall behaviour. However, the finer layering greatly increased computational time. Therefore, a layer thickness of 50 mm was adopted for all analyses using shell elements.

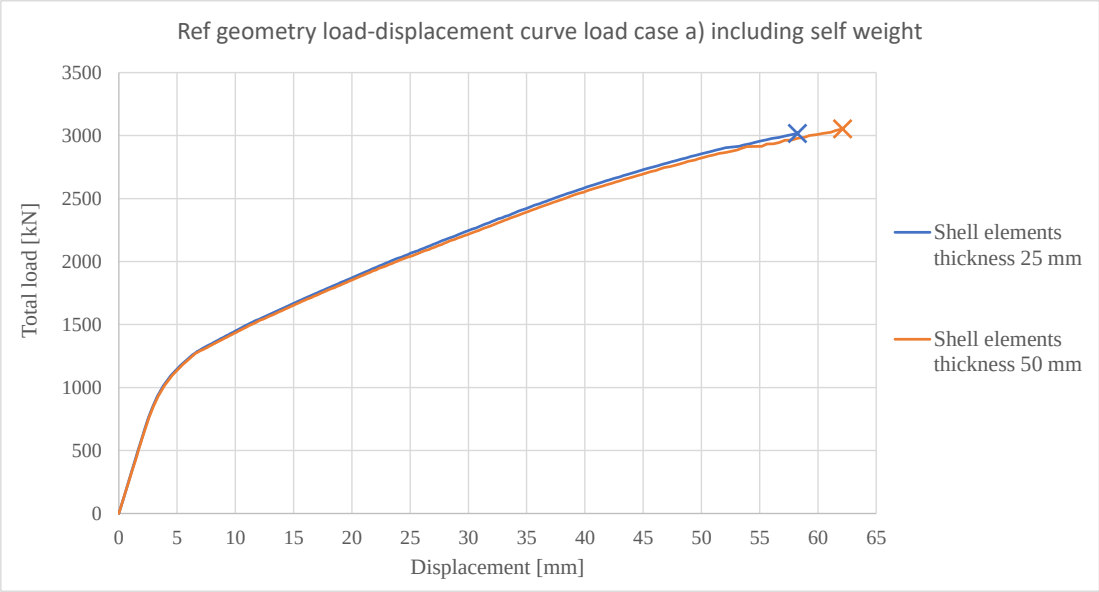

Figure 4.13: Load and displacement for shell elements with 50 and 25 mm layer thickness.

Based on the results from the mesh sensitivity analysis, and considering the relatively large extent of the model combined with the need to manage computational demands, a general element size of 100 mm was selected for the solid element model. To accurately capture local stress concentrations in the slab segment close to the loading plates, the mesh was refined in these regions using an element size of 40 mm. This refinement ensures that critical stress and strain distributions are properly represented, which is particularly important for evaluating potential shear and punching failures. Figure 4.14 presents a sectional view of the developed finite element mesh, illustrating the distribution and refinement of the elements across the cantilever slab.

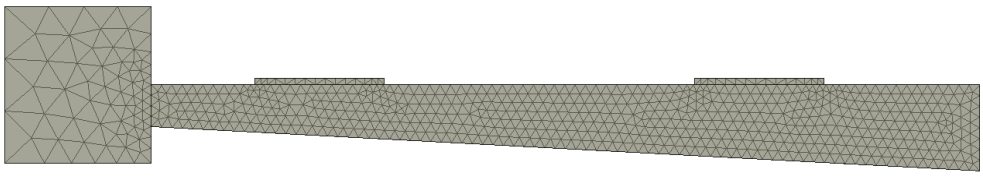

Figure 4.14: Section showing the mesh used for geometry Ref.

To further reduce computational demand, symmetry along the transversal axis of the slab was utilized for load cases where it was applicable. This allowed only half of the slab to be modelled, effectively reducing the number of elements by half without compromising accuracy. Figure 4.15 present an overview of the mesh for a solid element

model utilizing symmetry. The finer 40 mm mesh around the loading plates can be seen to the right in the model. However, when modelling the loading history, symmetry could not be applied, as this approach does not permit the simulation of a vehicle moving along the slab.

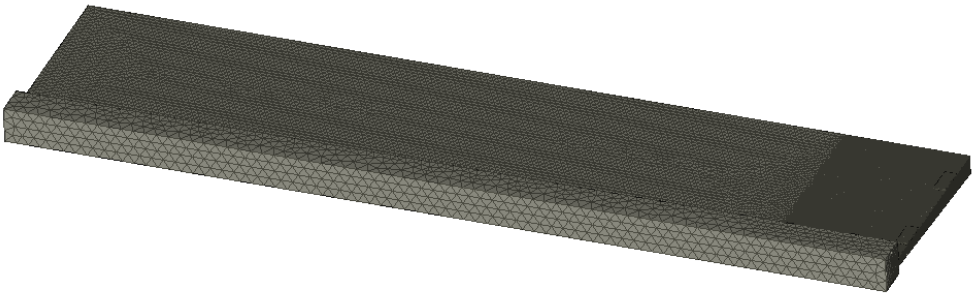

Figure 4.15: The cantilever modelled using symmetry for geometry Ref, with load case a).

4.5.2 Loading procedure and loading history

The concentrated loads are modelled using loading plates with dimensions 0.4 × 0.5 m, placed on the surface of the RC slab. Similar to the linear analysis, the load is assumed to spread at a 45-degree angle in the vertical direction through the surface layer, as illustrated in Figure 4.10, but only down to the surface of the RC slab, not to the system line. The loading plates are modelled with very low stiffness, 0.1 GPa, to avoid influencing the structural response of the slab.

The slab's response is analysed by gradually increasing the wheel loads until failure, enabling the determination of the maximum load capacity and allowing comparison with simpler analyses, such as linear FE models and hand calculations.

The loads are applied in steps, see Figure 4.16. First, permanent loads, including self-weight and dead loads (such as the surfacing layer), are applied up to a scaling factor of 1.2, corresponding to the load coefficient for permanent loads. Then, the variable load, in this case the vehicle load with a reference value of 100 kN, is incrementally applied until failure.

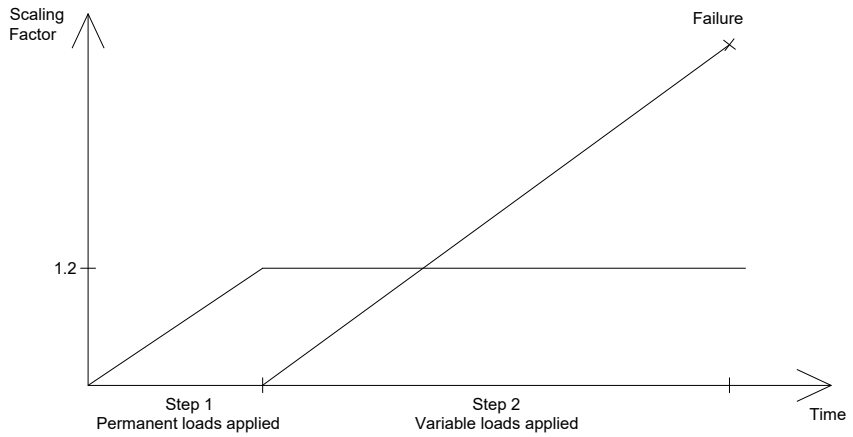

Figure 4.16: Applied load step procedure to failure.

Additional analyses were carried out to consider loading history. These simulations represent a vehicle driving along the slab and were performed by applying a SLS load, which was incrementally moved along the slab. Once the slab had been subjected to this moving load and a cracked state was established, the results were saved, and the analysis was continued using the same load cases as before. This step aimed to determine the slab's load-bearing capacity and load distribution after accounting for prior damage and accumulated cracking. Figure 4.17 presents the principle of the loading procedure with load history.

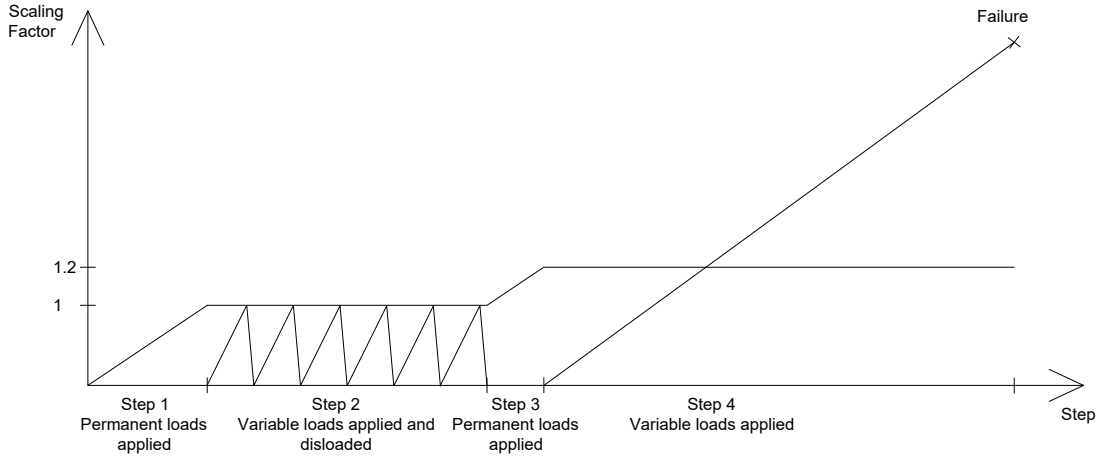

Figure 4.17: Applied load step procedure to failure including previous loads up to SLS.

The moving load was a bogie load representing the maximum SLS load for load case c). The maximum load value was derived from the ULS failure load from the non-linear shell elements model. Using maximum load values from earlier assessment levels for the SLS load did not result in sufficient cracking; therefore, values from the non-linear analysis were used.

4.5.3 Material parameters

The material used in the non-linear analysis is presented in Table 4.2. The stress-strain behaviour of concrete is presented in Figure 4.18 for compression and tension. When considering the safety format, the GRFm was chosen in order to reduced the number of analyses needed compared to the ECOV method. This method uses mean material values, calculated with the equations presented in Section 3.3.8. If results from material tests are available, they should be used as the basis for the analysis. However, for this analysis, generally assumed material properties are used.

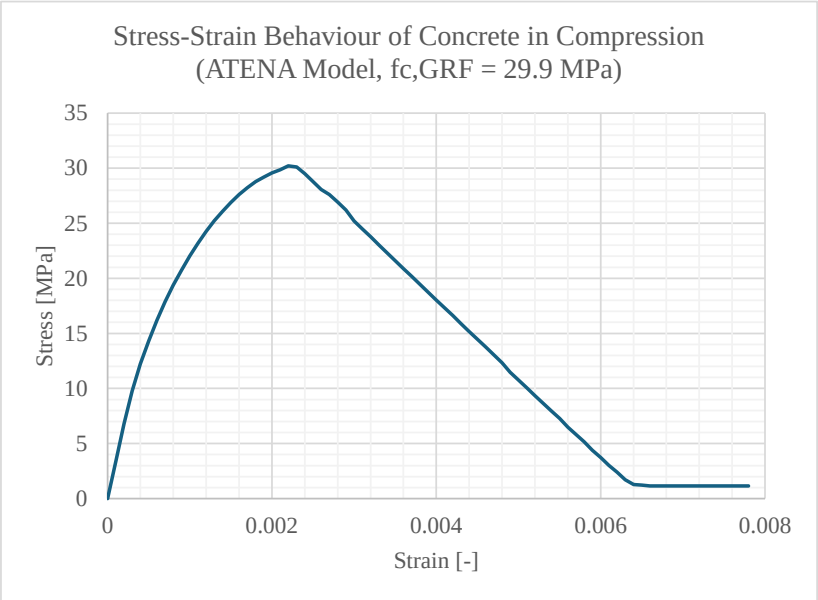

(a) Concrete in compression

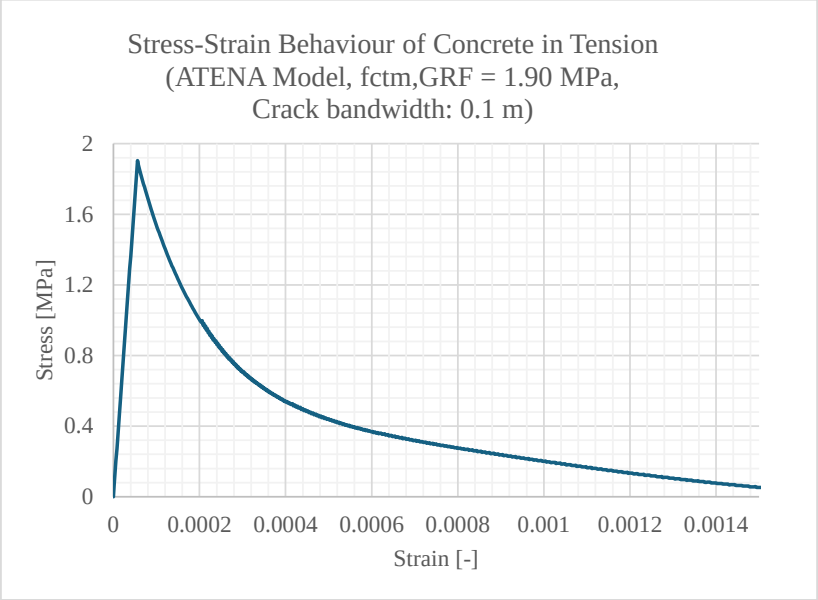

(b) Concrete in tension

Figure 4.18: Concrete behaviour used for: (a) compression, (b) tension.

The fracture energy presented in Table 4.2 has been calculated using Equation 3.8 and assuming a maximum aggregate size of 16 mm. The stress-strain relationships for the reinforcing steel is shown in Figure 4.19.

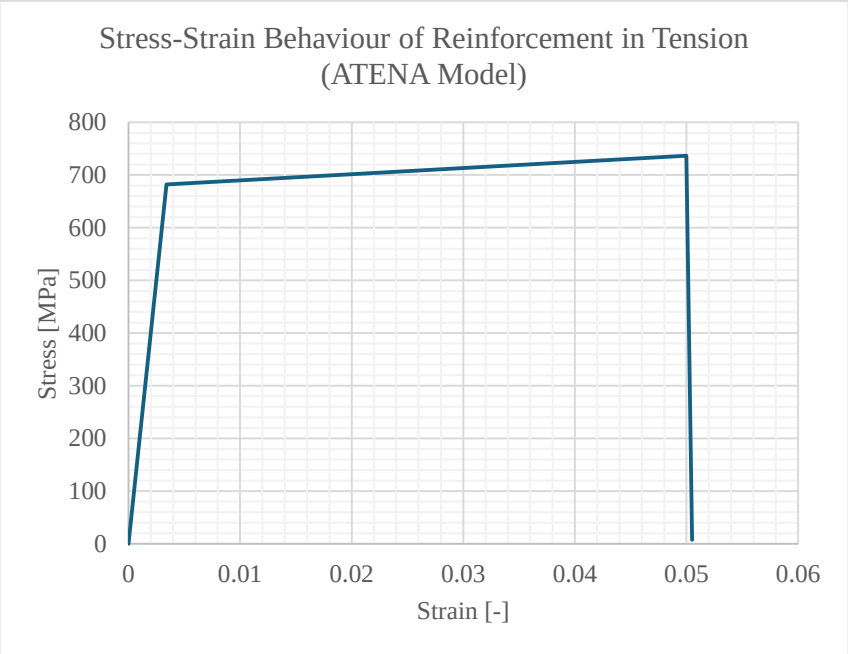

Figure 4.19: Stress strain behaviour of reinforcement.

The bond stress-slip relationship has been considered for the reinforcement in the transversal direction in the slab, while a perfect bond was assumed for the reinforcement in the longitudinal direction and in the edge beam. This assumption was made to accurately capture the bond behaviour where slip is most relevant while simplifying the model in the longitudinal direction. Since transverse reinforcement primarily governs load transfer and crack distribution, incorporating bond stress-slip behaviour provides a more realistic representation of structural response. Conversely, assuming a perfect bond in the longitudinal direction simplifies the analysis without significantly affecting accuracy, as slip effects in this direction are generally less critical for the investigated load cases. The bond stress-slip relationship used is shown in Figure 4.20.

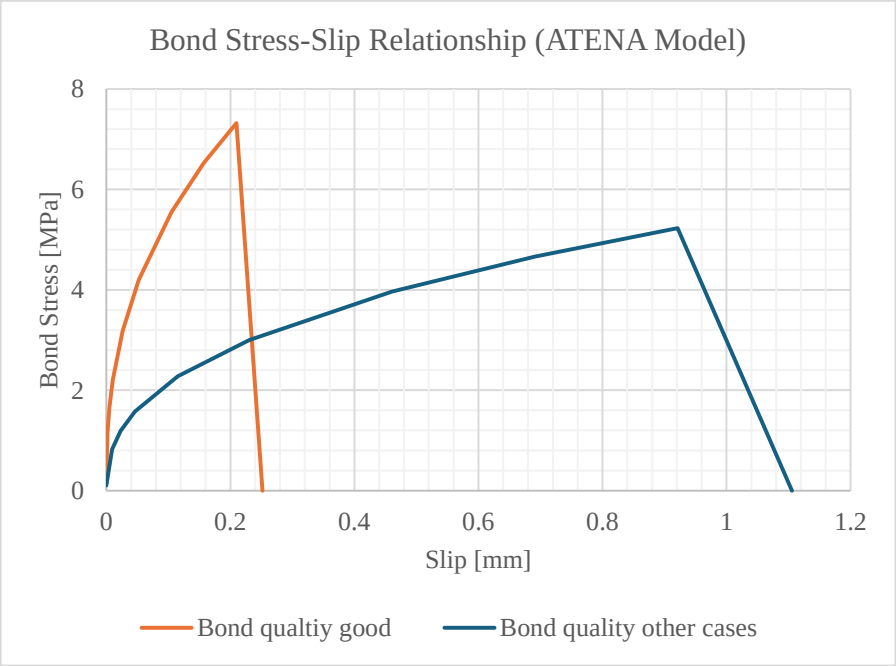

Figure 4.20: Bond stress-slip relationship used.

Reinforcement in the transverse direction in the bottom of the slab is assumed to have a good bond quality. While the transverse reinforcement in the top is assumed to have a lower bond quality.

To ensure consistency in the definition of the crack band width across the model, the element length has been used as the crack band width for both the reinforcement with bond stress-slip (transverse direction) and the reinforcement with perfect bond (longitudinal direction and edge beam). While the crack band width is typically taken as the element length in smeared crack models with bond stress-slip behaviour, it is more accurately related to the crack spacing in the case of perfect bond. Using the element length in this case may be slightly unconservative. Nonetheless, since the dominant cracking occurs in the transversal direction, this approach offers a reasonable and consistent simplification across the model.

To ensure equilibrium and accuracy in the non-linear FE analyses, four convergence criteria were implemented in the Newton-Raphson iterative procedure. A tolerance of 1 % was used for the displacement, residual, and absolute residual errors, while a tolerance of 0.01 % was used for the energy error. All four criteria had to be satisfied simultaneously for convergence to be accepted within an iteration step. To avoid excessive computation in case of non-converging load steps, the maximum number of iterations per step was set to 200.

The failure mode in the solid element model was determined by evaluating the crack pattern and width, as well as the stress distribution and deflection.

5 Results

This chapter presents the results from hand calculations, as well as linear and non-linear FE analyses. The findings for different geometries are compared to the base geometry, with a focus on variations in load-spreading effects and load capacity across different assessment methods. In general, the load capacity increases with more detailed assessment methods, where the non-linear analysis is able to redistribute loads more effectively. Figure 5.1 illustrates this trend by showing the load-displacement response for the reference geometry under load case f), along with the corresponding maximum B-load values for each assessment level. The deflection from the self-weight is not included in the figure.

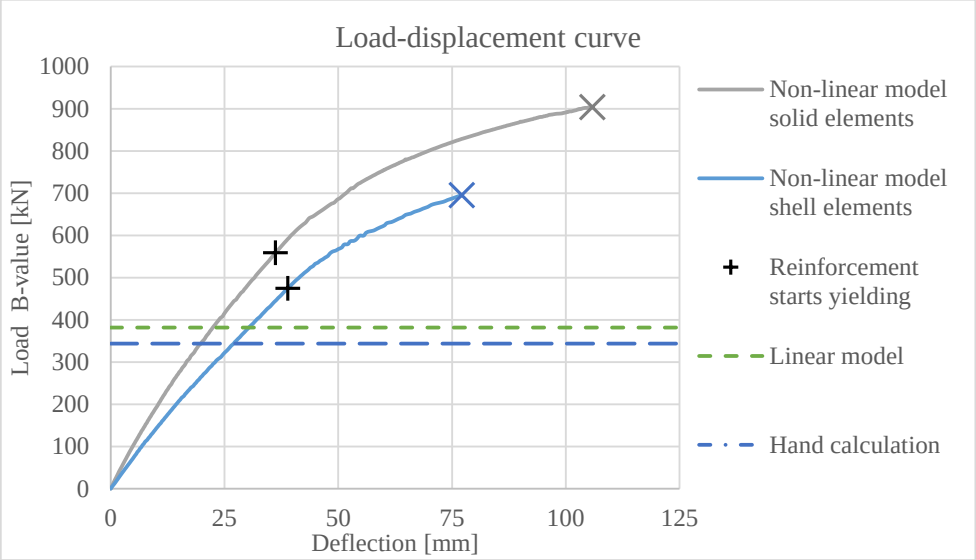

Figure 5.1: Load-displacement response and maximum B-load values for the Ref geometry under load case f), across different assessment levels.

Throughout this chapter, the results evaluated for shear is primarily based on Critical Section 1, as defined in Figure 4.3, which was identified as the governing section for most load cases. If another section proved to be more critical in a specific case, this will be explicitly noted.

5.1 Failure modes

The governing failure mode of the slab varied depending on the assessment method used. For linear analysis the failure mode was shear failure at the critical section for the inner wheel pair regardless of load case and geometry. Similarly for hand calculation the failure mode was shear failure at the inner critical section except for the model with no edge beam (NoEdge) where the failure mode was in moment. For the non-linear analysis, the failure mode varied between punching and moment failure.

To evaluate the governing failure mode, the ratio between the maximum load for shear and moment was calculated for each load case. Figure 5.2 presents these ratios for hand calculations, as well as for both the uncracked and cracked linear FE models for the reference geometry. A ratio below 1.0 indicates that shear governs over moment.

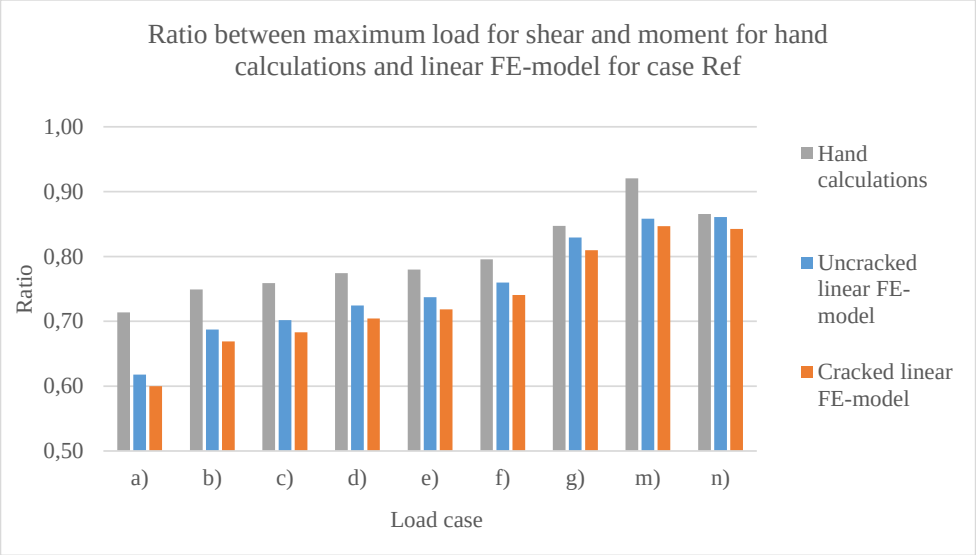

Figure 5.2: Ratio between the maximum load for shear compared to moment for hand calculations and both uncracked and cracked linear FE-models for case Ref.

As shown in Figure 5.2, shear was consistently the governing failure mode across all load cases for the reference geometry, both in hand calculations and in the linear FE models, correspond to assessment level 1 and 2. Furthermore, the ratio between shear and moment increases with higher load case labels, indicating that moment becomes increasingly significant relative to shear. A similar trend was observed for the geometries L4m, L2m, and tConst. However, in the case of tConst, the ratio exceeds 1.0 for load cases g) to n), suggesting a shift towards moment-governed behaviour.

In contrast, the trends for the NoEdge and t+0.1 cases differ from the reference geometry. As illustrated in Figure 5.3, the hand calculations indicate that moment is consistently the governing failure mode for all load cases, with ratios significantly above 1.0. However, both the uncracked and cracked linear FE-models show shear as the governing failure mode, with ratios well below 1.0. Similarly, for the t+0.1 case, shown in Figure 5.4, the results diverge from the reference case. Although shear is still the governing failure mode for all load cases and analyses, the difference in ratio between the hand calculations and linear FE models is significant.

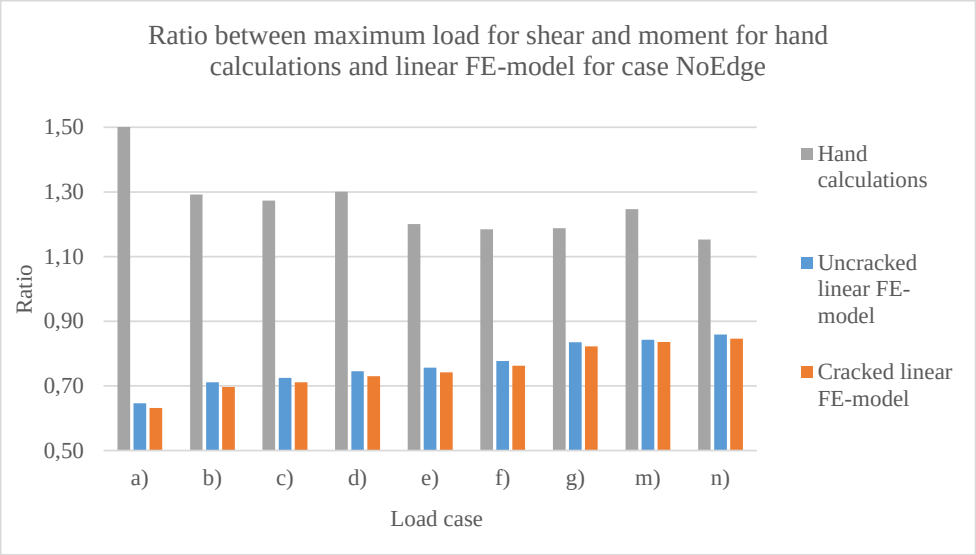

Figure 5.3: Ratio between the maximum load for shear compared to moment for hand calculations and both uncracked and cracked linear FE-models for case NoEdge.

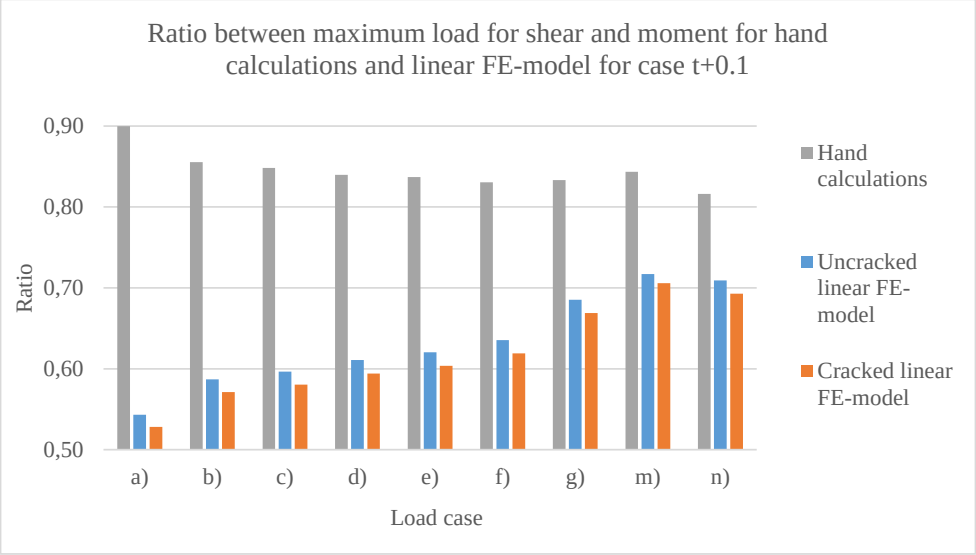

Figure 5.4: Ratio between the maximum load for shear compared to moment for hand calculations and both uncracked and cracked linear FE-models for case t+0.1.

Failure by punching shear was evaluated in the hand calculations but was not found to be critical for any of the studied load cases or geometries. Consequently, the results from these checks are excluded from the main figures but are available in Appendix C. In contrast, the non-linear analyses identified punching shear as the governing failure mode for most geometries subjected to load case a), which represents a single axle

wheel load. The Ref geometry exhibited a 91% higher ultimate load capacity compared to the corresponding hand calculation for punching failure. Table 5.1 summarises the failure modes obtained from the non-linear analyses using solid element models.

Table 5.1: Failure mode obtained in non-linear analyses with solid elements.

Load case	**a)**	**f)**
Ref	Punching	Moment
NoEdge	Punching	Moment
tConst	Moment	Moment
L4m	Punching	Moment
L2m	Punching	Moment
t+0.1	Punching	Moment

Figure 5.5 show the crack distribution and crack width along the cross section at maximum load of the L4m slab when subjected to load case a), representing one axle, fails in a brittle manner through punching shear failure in the non-linear analysis. This failure mode for load case a) was the same for all tested geometries with tapered slab in the non-linear analysis, Ref, NoEdge, t+0.1, L2m, and L4m. The crack pattern in the figure shows a shear crack along the critical sections and cracks at the root of the slab from the moment force. The geometry with constant thickness, tConst, failed in moment failure. Although the linear results did not predict moment failure for load case a) and f) in geometry tConst, they indicate that this geometry exhibits a behaviour more governed by bending compared to the others.

(a) The most significant cracks per element with a crack width size over 0.15 mm.

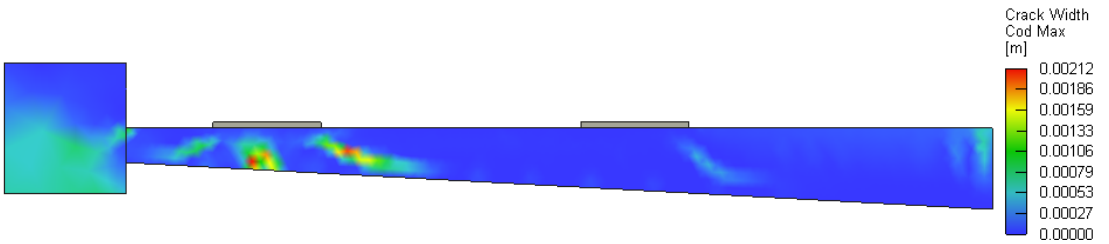

(b) Crack width.

Figure 5.5: Cross section in the transverse direction of L4m slab subjected to load case a).

The punching shear failure mode around the other load plate in the cantilever slab, as shown in Figure 5.5a, exhibited inclined cracks extending from the loaded area towards both the support and the edge beam. The edge beam functions as a flexible support for the slab.

For load case f) where three wheel pairs were loading the cantilever, the failure mode in the non-linear analysis showed moment failure for all geometries. When the reinforcement yielded, the moment forces were redistributed along the support. The slab failed by either crushing of the concrete or the reinforcement reaching its ultimate strain. Figure 5.6 presents the left side of the cantilever slab and due to symmetry in load case, only half of the slab was modelled for more efficient analysis. It can be noted that the yielding of the reinforcement goes well beyond the loading plates.

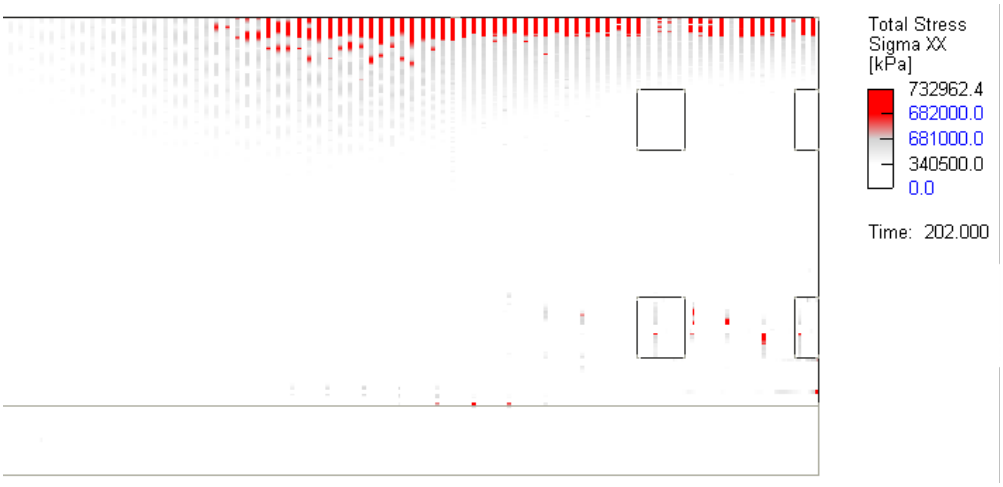

Figure 5.6: The reinforcement yielding for maximum load for geometry tConst with solid element model subjected to load case f). Only half of the cantilever is model and uses symmetry for efficiency, hence only the left half of the slab is presented.

In Figure 5.7, the crack widths and distribution are presented for the tConst geometry subjected to load case a). The results indicate a moment failure mechanism, although significant inclined cracks are formed near the outer load plate. This suggests a combined failure behaviour where the slab initially resists the load through flexural action, but as the moment capacity was reached at the support, increased rotation caused redistribution of the moment. This lead to a rise in moment demand beneath the outer load plate, which increased the crack widths and the risk of localized punching failure in that region.

(a) The most significant cracks per element with a crack width size over 0.15 mm.

(b) Crack width.

Figure 5.7: Cross section in the transverse direction of tConst slab subjected to load case a).

The failure modes for non-linear models using shell elements are not included in this section. These models exhibited convergence issues before reaching ultimate capacity, most likely due to their inability to capture localized failure mechanisms such as punching and shear. Therefore, only solid element models are considered reliable for interpreting failure behaviour.

5.2 Comparison between hand calculations and linear FE-models

Figures 5.8 and 5.9 show the ratio between the maximum loads obtained from hand calculations and those predicted by the linear FE models for the Ref geometry. Both uncracked and cracked conditions were considered, where cracking was modelled in the FE analyses by reducing the Young's modulus in the transverse direction. A ratio below 1.0 indicates a higher capacity obtained from the hand calculations.

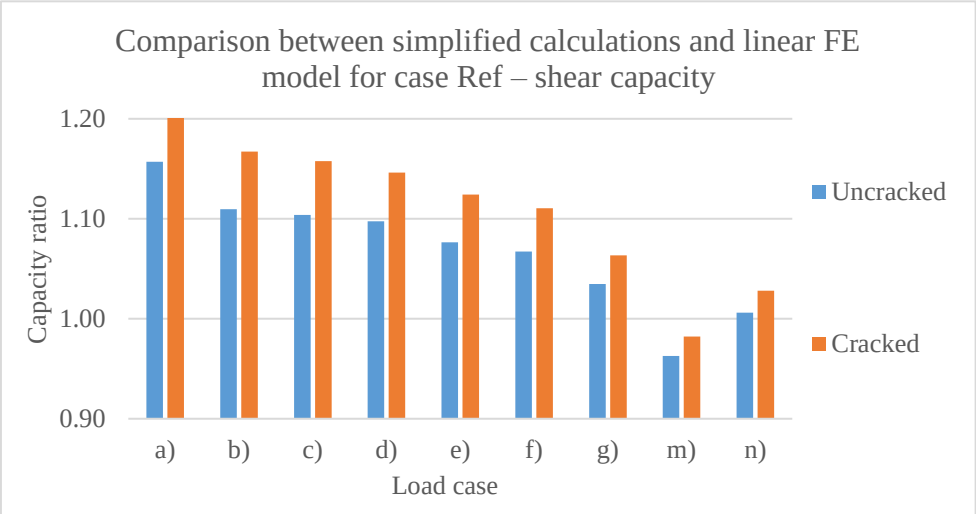

Figure 5.8: Comparison between hand calculations and the linear FE model for the Ref geometry, considering shear capacity for both uncracked and cracked concrete in the transverse direction.

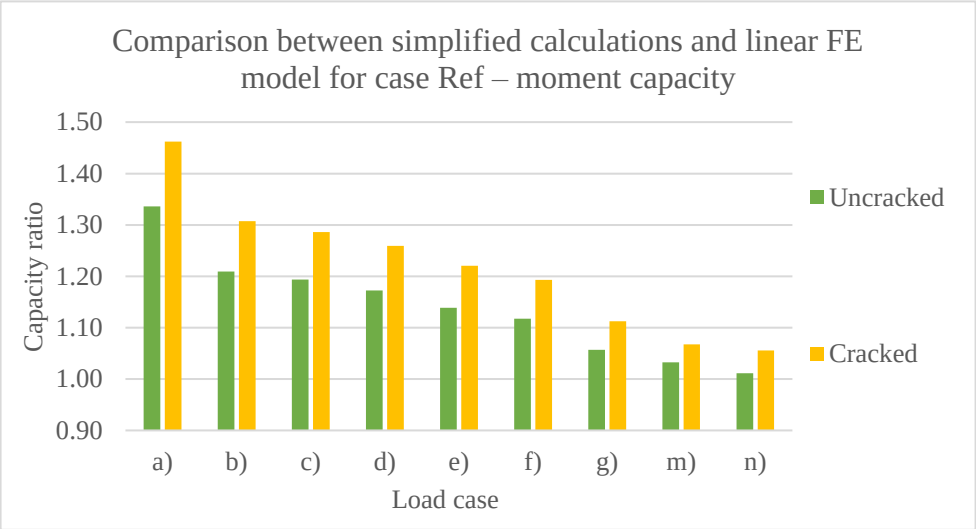

Figure 5.9: Comparison between hand calculations and the linear FE model for the Ref geometry, considering moment capacity for both uncracked and cracked concrete in the transverse direction.

Except for load case m) in the shear comparison, the linear FE models consistently predicted higher load-bearing capacities than the hand calculations for both shear and moment across all load cases. Additionally, for load cases involving multiple loads, the difference between hand calculations and FE predictions became smaller.

When comparing the effective width used in the hand calculations to that of the linear FE models for shear, the FE models typically yielded a shorter effective width. In the

hand calculations, it was assumed that all shear forces were fully transferred within this width, whereas this assumption did not hold for the FE models. However, as the number of loads were increased and the effective widths began to overlap, a greater portion of the shear effects was captured within the smaller effective width of the FE models, which consequently limited the predicted capacity. Although the expressions for moment is not as easily comparable, the same trend could be seen when increasing the number of loads. The same trend for both shear and moment could be seen across all geometries, which can be seen in Appendix B which shows similar figures for all geometries as in Figure 5.8 and 5.9.

Although the trend of a decreasing capacity ratio with an increasing number of loads was consistent across all geometries, the capacity ratio remained below 1.0 for most load cases in the NoEdge and t+0.1 geometries when evaluating shear capacity. Figure 5.10 presents the shear distribution for load case f), comparing the Ref and t+0.1 geometries. The figure illustrates that the effective widths differed between the geometries, primarily due to a greater effective depth at the critical section in geometry t+0.1. Nevertheless, the overall shear distribution was relatively similar, indicating that a higher proportion of the shear effects was captured within the effective width. This explains the lower shear capacity predicted by the FE models compared to the hand calculations.

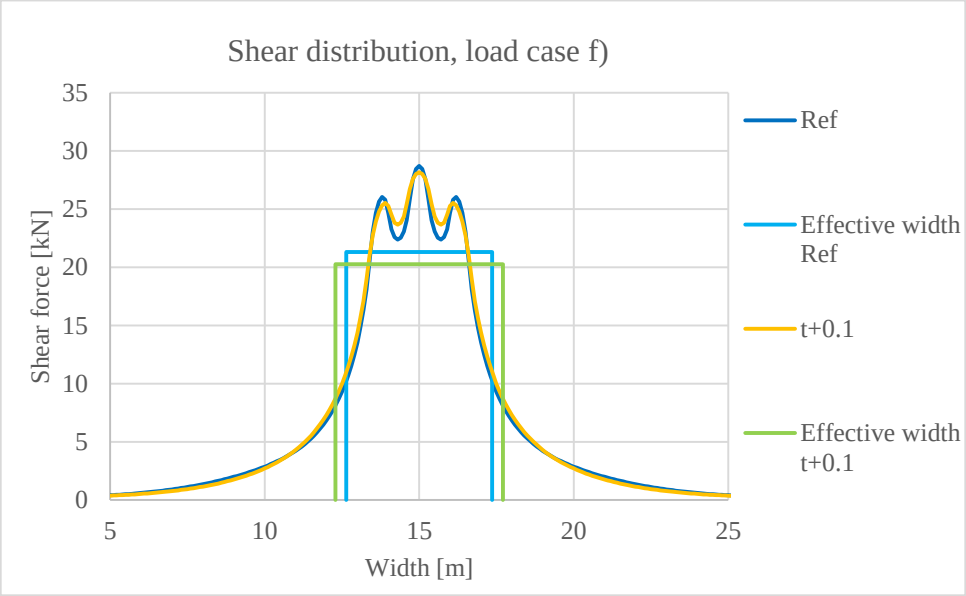

Figure 5.10: Shear distribution for load case f) with an applied load of $B = 100$ kN for the Ref and t+0.1 geometries. The self-weight is excluded. The marked zones represent the assumed effective widths.

5.3 Load distribution in linear FE-models

As mentioned, the discrepancy in maximum load capacity between hand calculations and linear FE-models decreased progressively with the number of axle loads, which suggests that a more distributed load leads to a more even internal force distribution.

Moreover, the inclusion of transverse cracking in the FE models resulted in increased load capacity, as the reduced transverse stiffness allowed for a broader distribution of loads. This effect is illustrated in Figure 5.11 and 5.12, which show the internal force distribution for load case a).

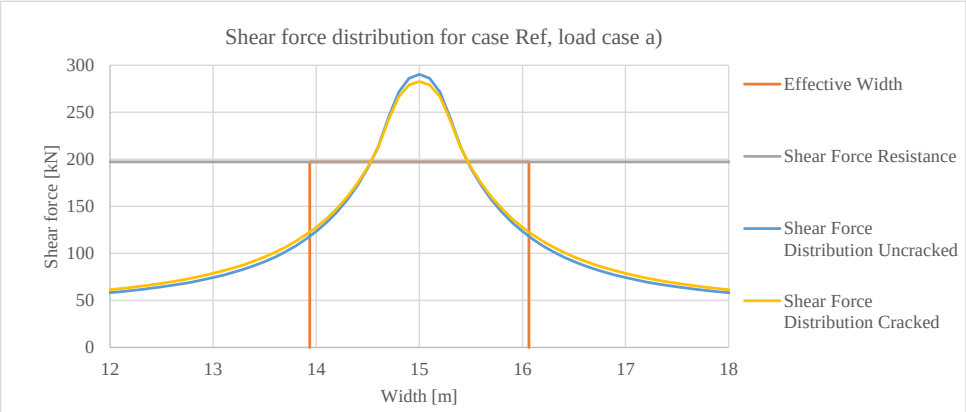

Figure 5.11: Distribution of shear forces from linear FE-model for case Ref using load case a).

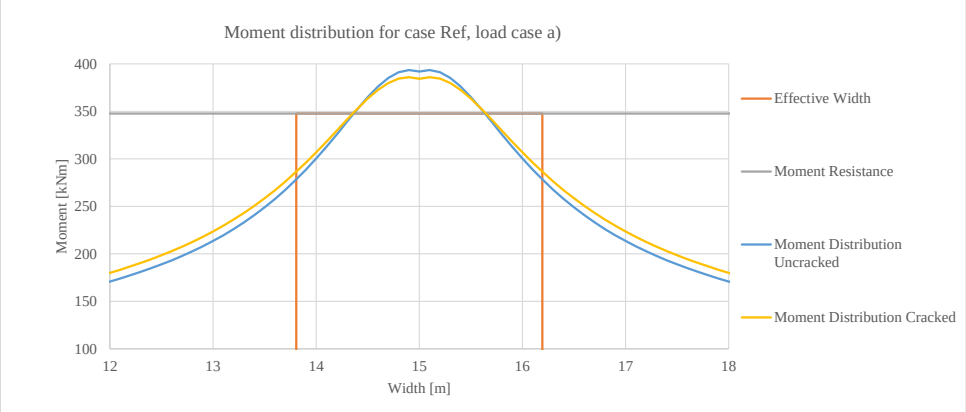

Figure 5.12: Moment distribution from linear FE-model for case Ref using load case a).

However, this effect was less pronounced in load cases involving a greater number of applied loads. Figure 5.13 and 5.14 illustrate the internal force distribution for load case n), where the difference between uncracked and cracked FE models was relatively small. This is likely due to the increased number of concentrated loads promoting a more uniform load distribution, thereby reducing the influence of transverse stiffness on the global structural response. This trend was consistently observed across all geometries and for both shear and moment responses.

Figure 5.13: Distribution of shear forces from linear FE-model for case Ref using load case n).

Figure 5.14: Moment distribution from linear FE-model for case Ref using load case n).

This trend is further illustrated in Figures 5.15 and 5.16, which show the shear force distributions for load cases a) and n), respectively, considering cracking in the transverse direction. In load case n), it was evident that the longitudinal load-spreading effects began to overlap, thereby reducing the influence of transverse cracking on the analysis outcome. Both figures provide an overview of the slab, where the red boxes indicate the locations of the applied loads. The grey area at the bottom represents the edge beam, while the fixed support is located at the top of the slab (not visible in the figures). The values presented correspond to shear forces in kN.

In Figure 5.15, corresponding to load case a), the critical sections are also indicated. For Critical Section 1, it is evident that the section intersects the area with the highest concentration of shear forces, confirming its role as the governing section in the analysis.

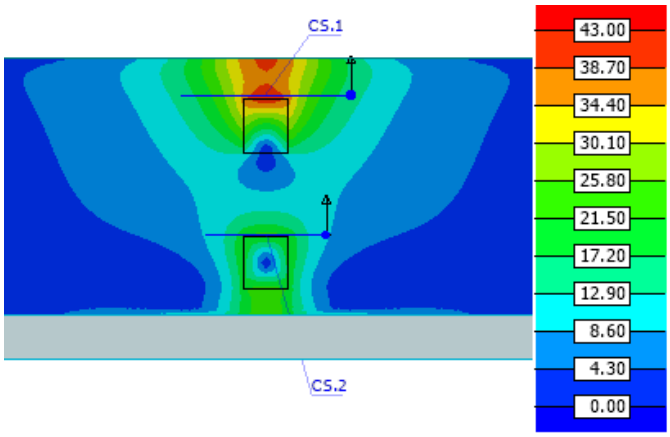

Figure 5.15: Distribution of shear forces in load case a) from the linear analysis towards the supports for a unit load of A=100 kN without considering self-wight. The black boxes shows the applied concentrated loads.

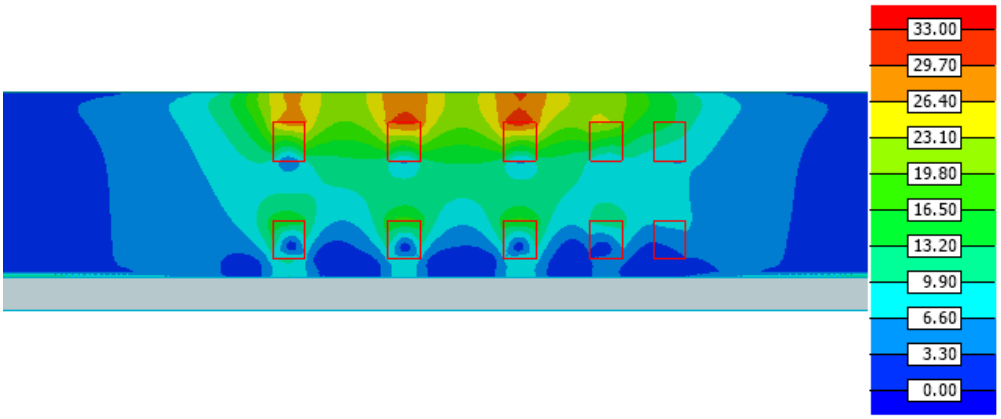

Figure 5.16: Distribution of shear forces in load case n) from the linear analysis towards the supports for a unit load of B=100 kN without considering self-weight. The red boxes shows the applied concentrated loads.

The load case L2m differs from the others in that only one wheel from each wheel pair is positioned on the overhang slab. Consequently, the shear distribution for load case a) in geometry L2m was compared to the distribution in Critical Section 2 of the Ref geometry, as shown in Figure 5.17. Although the loads were applied at the same distance from the slab edge in both geometries, their distance to the support differed. The figure illustrates that the Ref geometry enabled a wider distribution of shear forces.

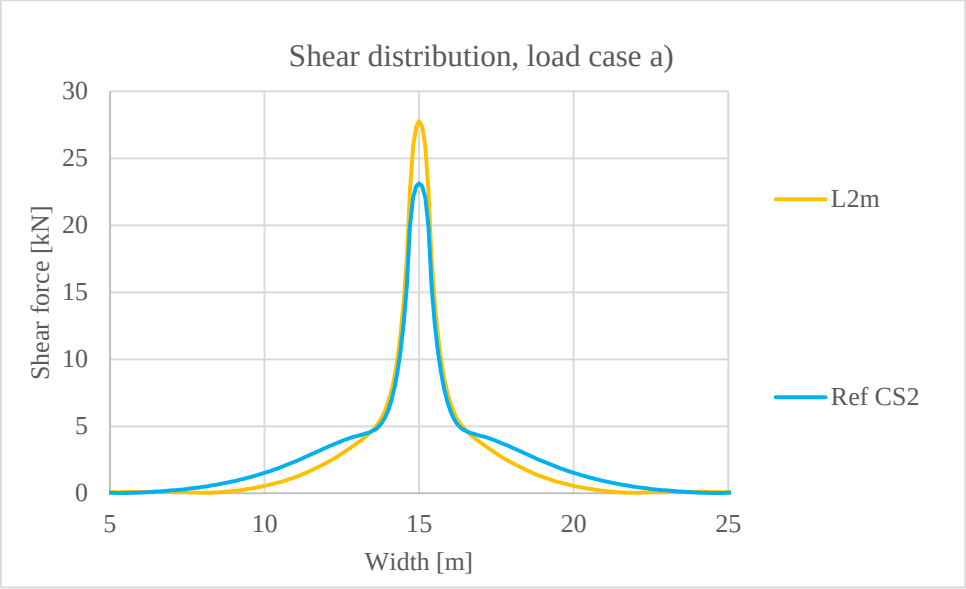

Figure 5.17: Shear distribution from linear FE-model using load case a) for case L2m and Critical Section 2 for case Ref.

5.4 Impact of edge beam

The influence of the edge beam on the ultimate load capacity and load distribution varied depending primarily on the assessment level and also the specific load case. In general, the edge beam has a more pronounced effect when fewer concentrated loads were applied. As the loads became more distributed across a wider portion of the slab, the edge beam's contribution to redistributing forces along the slab diminished and became less significant. Additionally, the effect of the edge beam differed depending on whether shear or moment was the governing failure mode.

As shown in Figures 5.2 and 5.3, hand calculations indicate that for the Ref geometry, shear governed the failure, whereas for the NoEdge geometry, failure was governed by bending moment across all cases. Table 5.2 summarizes the maximum load-bearing capacity and the influence of the edge beam for the base geometry based on hand calculations. This comparison highlights the differences in load capacity governed by shear and moment, respectively.

Since the edge beam was considered solely as a dead load in the shear capacity evaluation, it led to a consistent 6 % reduction in capacity across all cases. In contrast, for moment capacity, the edge beam contributed significantly to the longitudinal stiffness, resulting in substantial increases in load-bearing capacity, ranging up to nearly 100 % for load case a). Due to the shift in governing failure mode between geometries, the overall load-bearing capacity also changed, which is reflected in the final row of Table 5.2.

Table 5.2: Comparison of maximum load capacity, expressed in A and B-value, for geometries NoEdge and Ref (with edge beam) and their difference for each load case from hand calculations.

Load case	**a)**	**b)**	**c)**	**d)**	**e)**	**f)**	**g)**	**m)**	**n)**
Shear									
No Edge Beam [kN]	257	391	370	375	368	365	392	411	394
With Edge Beam [kN]	242	367	348	353	346	344	369	386	371
Difference [%]	-5.9	-5.9	-5.9	-5.9	-5.9	-5.9	-5.9	-5.9	-5.9
Moment									
No Edge Beam [kN]	171	302	290	289	306	308	330	329	342
With Edge Beam [kN]	339	491	458	456	444	432	435	420	429
Difference [%]	98.6	62.2	57.8	58.0	44.9	40.1	31.9	27.4	25.3
Load-bearing difference [%]	41.7	21.5	19.8	22.3	13.0	11.4	11.7	17.3	8.4

Corresponding results from the linear FE analyses are presented in Table 5.3. In these analyses, shear was the governing failure mode for both the Ref and NoEdge geometries across all load cases. Although the differences in load-bearing capacity were relatively small, the edge beam consistently contributed to a slight increase in shear capacity, with the exception of load case m). In this case, the added dead load from the edge beam outweighed its beneficial effect in redistributing shear forces, leading to a marginal decrease in overall capacity.

As with the hand calculations, the effect of the edge beam was more pronounced when evaluating moment capacity. The presence of the edge beam resulted in an increase in moment capacity for most load cases, though the effect was smaller compared to the hand calculations. In load cases m) and n), the contribution of the edge beam was minimal or even slightly negative.

Table 5.3: Comparison of maximum load capacity, expressed in A and B-value, for geometries NoEdge and Ref (with edge beam) and their difference for each load case from linear analysis.

Load case	**a)**	**b)**	**c)**	**d)**	**e)**	**f)**	**g)**	**m)**	**n)**
Shear									
No Edge Beam [kN]	280	400	376	381	364	360	383	381	378
With Edge Beam [kN]	297	429	403	405	389	382	392	379	381
Difference [%]	6.1	7.2	7.0	6.3	6.9	6.0	2.2	-0.6	0.8
Moment									
No Edge Beam [kN]	444	574	529	521	490	472	467	456	447
With Edge Beam [kN]	496	641	589	575	541	515	484	448	453
Difference [%]	11.8	11.7	11.4	10.2	10.4	9.1	3.8	-1.8	1.2

To further illustrate the difference in load distribution between shear and moment, Figures 5.18 and 5.19 present the shear force and moment distributions for the Ref and

NoEdge geometries under load case a), based on the linear analyses. These figures clearly demonstrate that the edge beam has a greater influence on the distribution of moments than on shear forces. While its impact on shear is limited, the edge beam enhances the slab's stiffness in the longitudinal direction, thereby enabling a wider and more effective redistribution of bending moments.

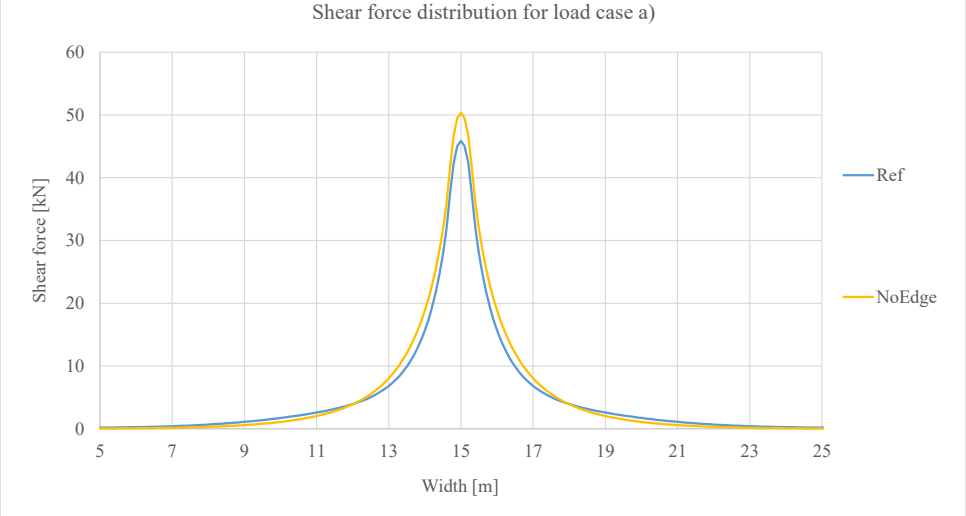

Figure 5.18: Shear force distribution for uncracked slab subjected to load case a), with and with out an edge beam.

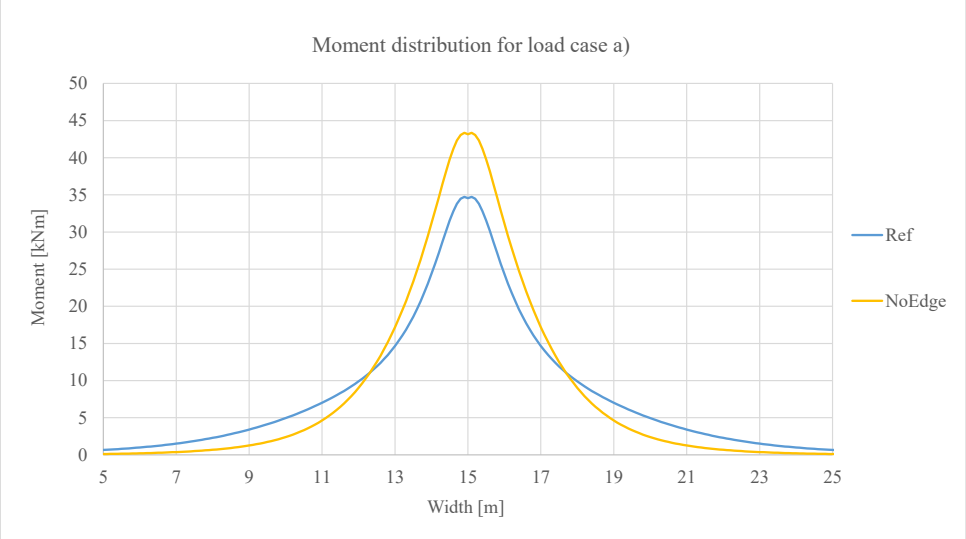

Figure 5.19: Moment distribution at support for uncracked slab subjected to load case a), with and with out an edge beam.

Table 5.4 presents the maximum load-bearing capacity obtained from the non-linear analyses for the Ref and NoEdge geometries. Compared to the results from the linear analyses, the influence of the edge beam was significantly greater in the non-linear models. This highlights the edge beam's enhanced ability to contribute to load redistribution and overall structural capacity when non-linear material behaviour and cracking were taken into account.

Table 5.4: Comparison of maximum load capacity value, expressed in A and B-value, for solid and shell elements in a non-linear model for load case a) and f).

Load case	**a)**		**f)**		**n)**	
Element Type	**Shell**	**Solid**	**Shell**	**Solid**	**Shell**	**Solid**
No Edge Beam [kN]	461	611	544	639	456	560
With Edge Beam [kN]	700	887	693	899	552	692
Difference [%]	52.0	45.3	27.2	40.8	21.0	23.4

Figures 5.20 and 5.21 show the moment and shear force distributions obtained from the non-linear analyses for load case a), comparing the Ref and NoEdge geometries. These results can be compared to the corresponding linear analyses shown in Figures 5.18 and 5.19. Unlike the linear analyses, the results from the non-linear models include the self-weight of the structure in both the moment and shear force distributions. As expected, the Ref geometry exhibited a higher self-weight due to the presence of the edge beam. The figures illustrate the distributions for the same applied load in both geometries, and the maximum moment and shear effects are of similar magnitude. However, as shown in Table 5.4, the overall load-bearing capacity of the Ref geometry was significantly higher. This is attributed to the edge beams impact on the redistribution, which is further shown in Section 5.5.

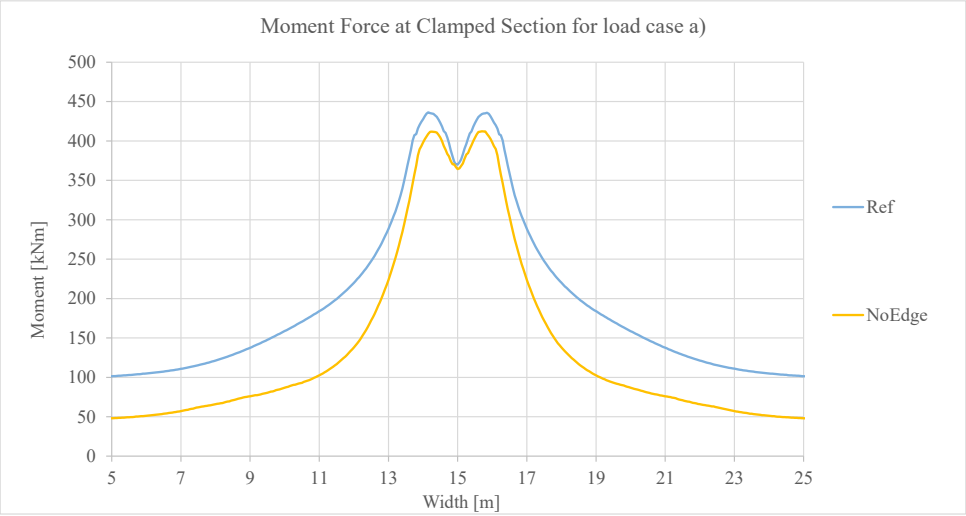

Figure 5.20: Moment distribution at support for geometry cases Ref and NoEdge from non-linear analysis for load case a).

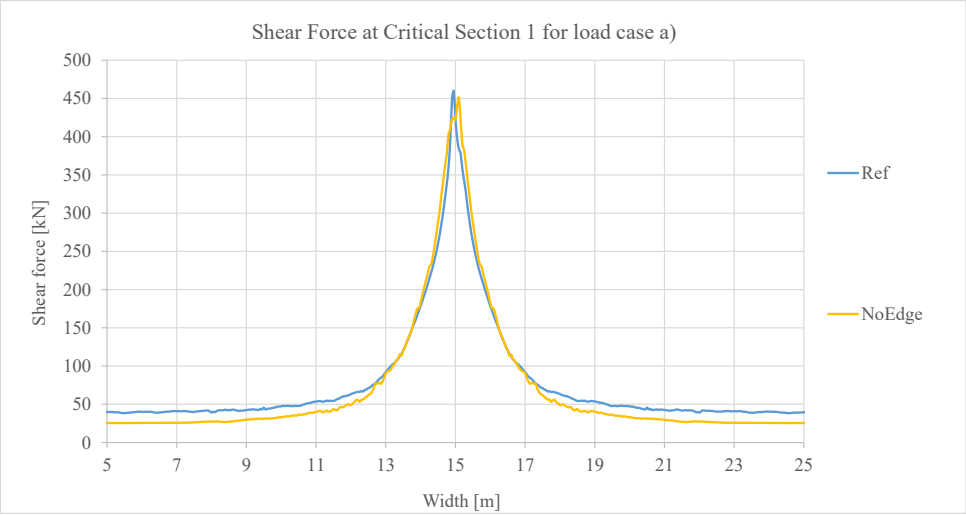

Figure 5.21: Shear force distribution at support for geometry cases Ref and NoEdge from non-linear analysis for load case a).

5.5 Non-Linear FE analyses results

This section presents the results from the non-linear FE analyses and compares them to the results of the simplified hand calculations and linear FE analyses. As described in Section 3.3, two different model configurations were used in the non-linear analysis: one model using only solid elements, and another model using solid elements for the edge beam and loading plates, and shell elements for the slab. Results from both model types are presented below.

To verify the validity of the model, Figure 5.22 shows the deflection of the solid model under self-weight only. Additionally, Figure 5.23 illustrates the resulting crack widths for the same load condition.

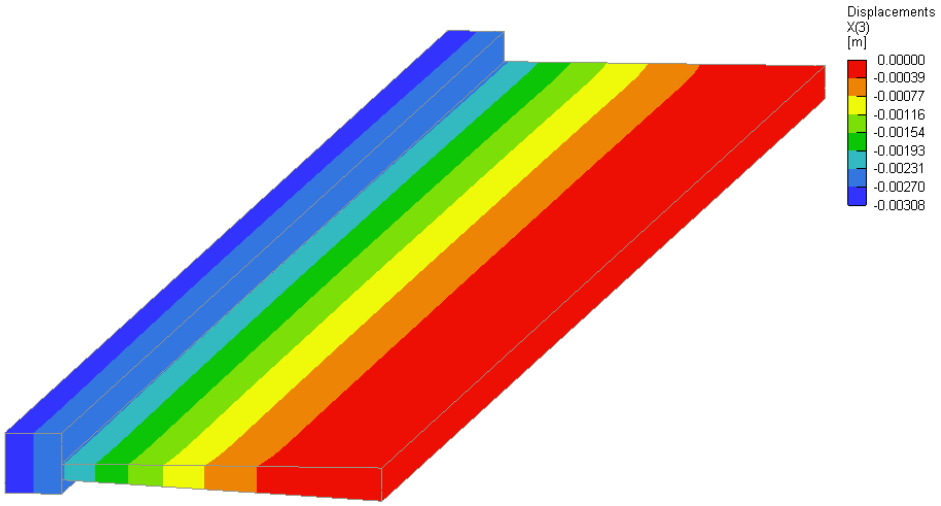

Figure 5.22: Displacement of the slab only considering the self-weight.

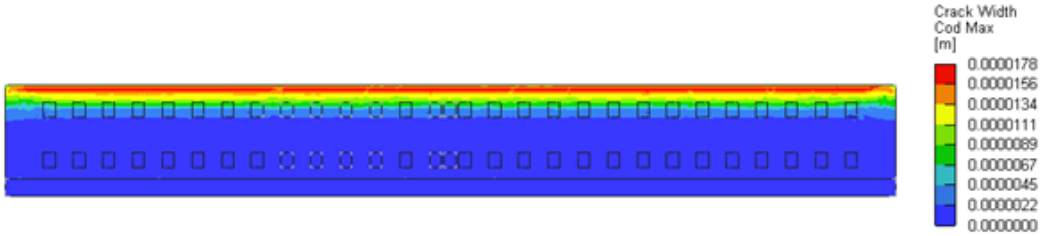

Figure 5.23: Crack width in the slab, only considering self-weight.

Table 5.24 presents the increase in ultimate load capacity for load cases a) and f) when compared to the linear FE models. The results indicate a significant capacity increase in the non-linear analyses, particularly for load case a). This observation aligns with the findings from the comparison between hand calculations and linear models in Section 5.2, where the difference was shown to decrease as more loads were included in the load case. However, it is important to note that the failure modes differed between the linear and non-linear models.

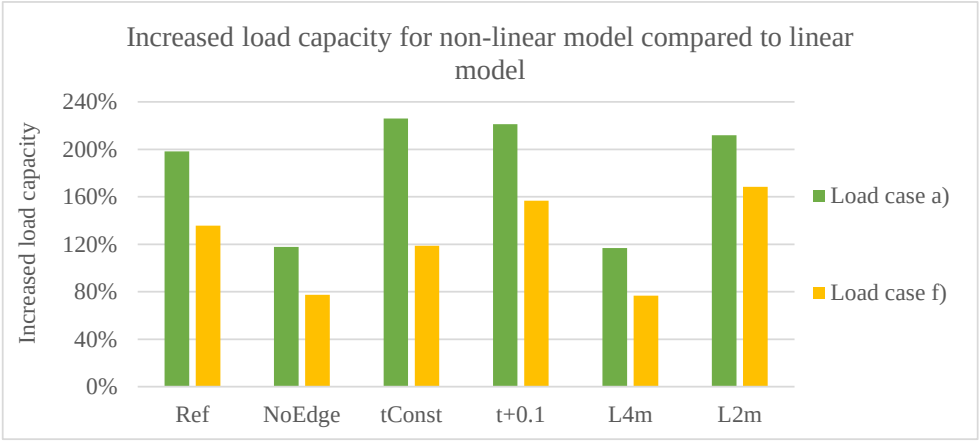

Figure 5.24: The non-linear model with solid elements increased ultimate load capacity compared to the linear model.

To enable a more consistent comparison, Figure 5.25 shows the increase in load capacity of the non-linear model relative to the linear model when the same failure modes are considered. Instead of comparing the governing failure mode from each model independently, the linear model results are here extracted based on the failure modes identified in the non-linear analyses. Since punching was found to govern for all geometries except tConst in load case a), it becomes evident that the difference in load capacity between the non-linear and linear models, when both were evaluated for punching, was significantly smaller than in Figure 5.24, where differing failure modes were compared. A similar trend was observed in cases where moment capacity was governing.

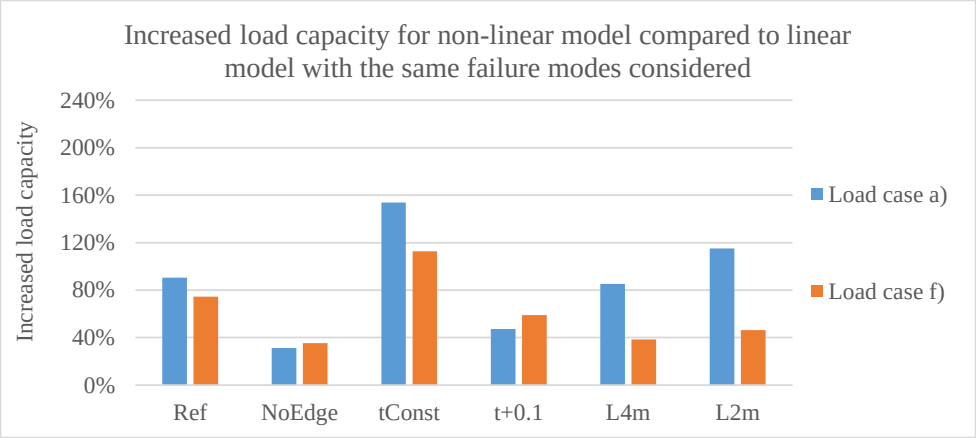

Figure 5.25: The non-linear model with solid elements increased ultimate load capacity compared to the linear model for the same failure mode.

Figures 5.26 and 5.27 show the shear distribution in Critical Section 1 for load case a) of the base geometry. The figures compare the results from the non-linear analysis with those from the linear analysis, including both the cracked and uncracked models. Prior to reinforcement yielding, the results show good agreement between the models. However, once yielding occurs, the shear distribution in the non-linear analysis begins to shift toward the slab edges, indicating a redistribution of internal forces.

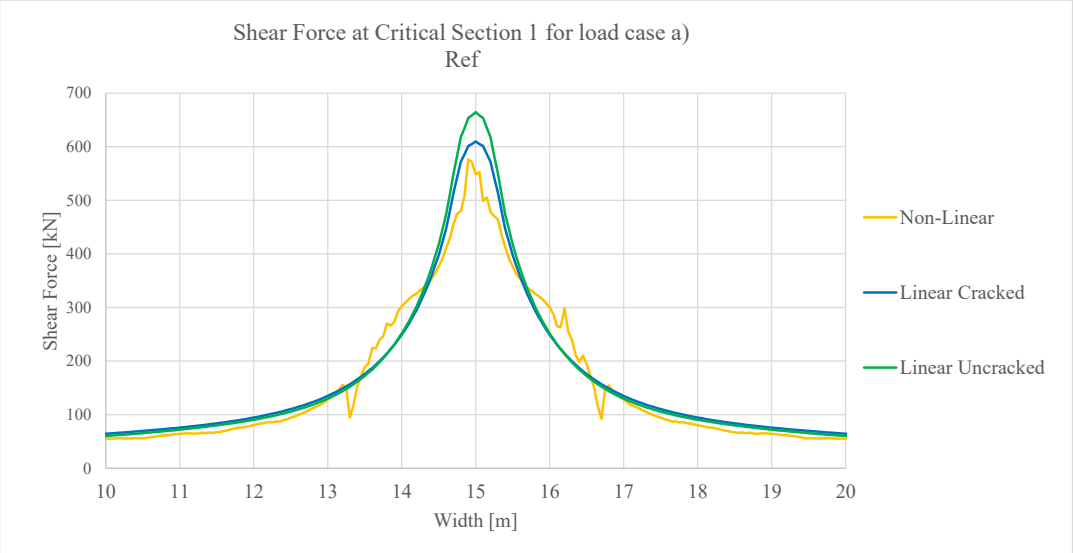

Figure 5.26: Shear force distribution before reinforcement start yielding.

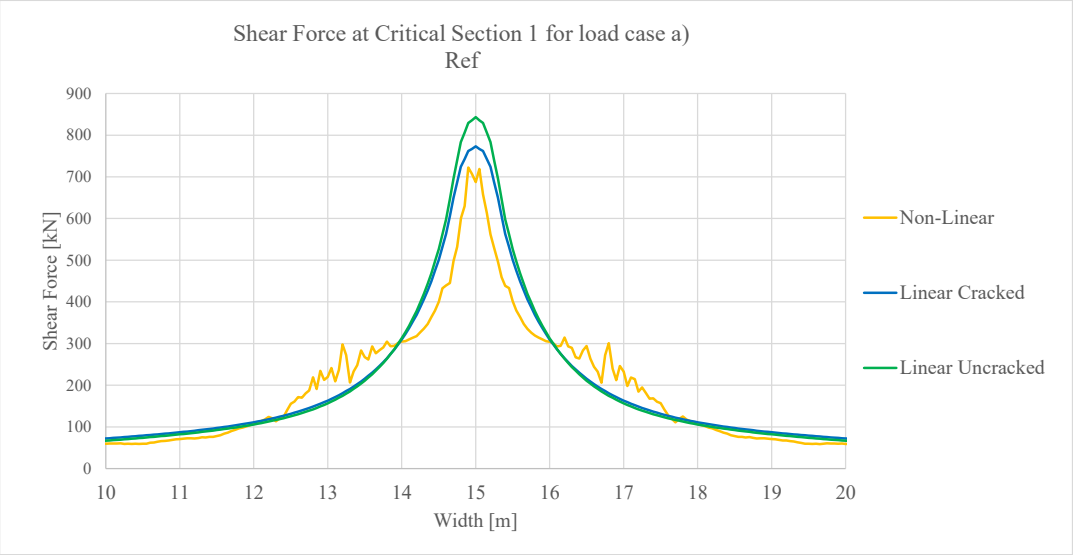

Figure 5.27: Shear force distribution after reinforcement yield.

The redistribution of forces toward the slab edges is further illustrated in Figure 5.28, which shows the moment distribution from the non-linear analysis at various load levels. Initially, the moment increased in the central region, closely following the distribution predicted by the linear analysis. However, beyond the onset of reinforcement yielding, the peak moment stabilized, and instead, the moment was gradually redistributed laterally toward the edges. This behaviour revealed a limitation of the linear analysis, where the assumed effective width significantly underestimates the actual load distribution near the ultimate load capacity.

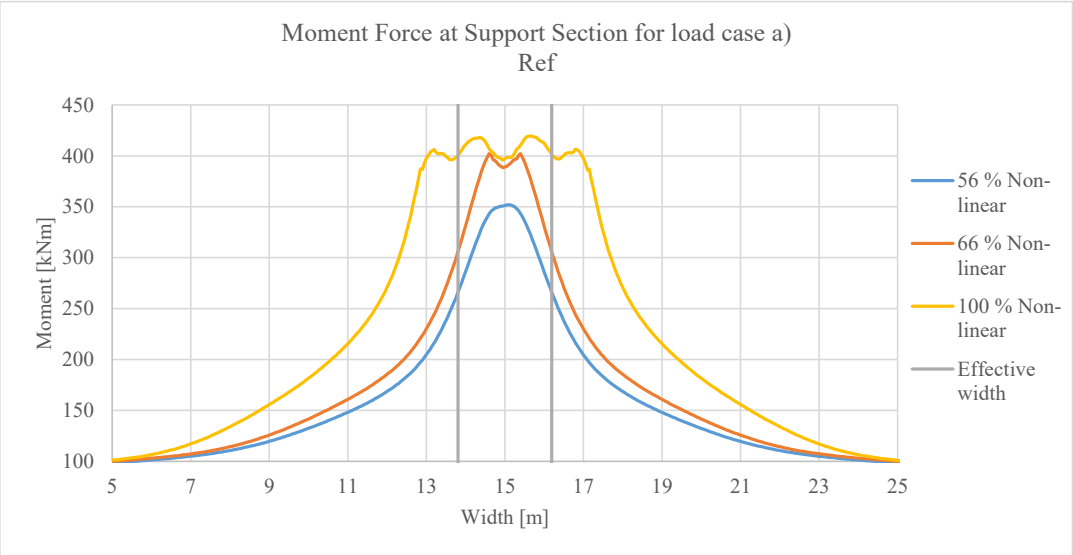

Figure 5.28: Moment distribution for case Ref subjected to load case a). Utilization ratio of maximum load capacity in non-linear analysis. The effective with used in linear analysis is presented.

A similar trend can be observed in Figure 5.29, which presents the moment distribution for load case f) in the L4m geometry. For comparison, the figure also includes the moment distribution from the linear analysis, shown at the same load levels as those used in the non-linear analysis. Although these load levels exceed the ultimate capacity predicted by the linear model, the results have been scaled to facilitate a direct comparison with the non-linear analysis.

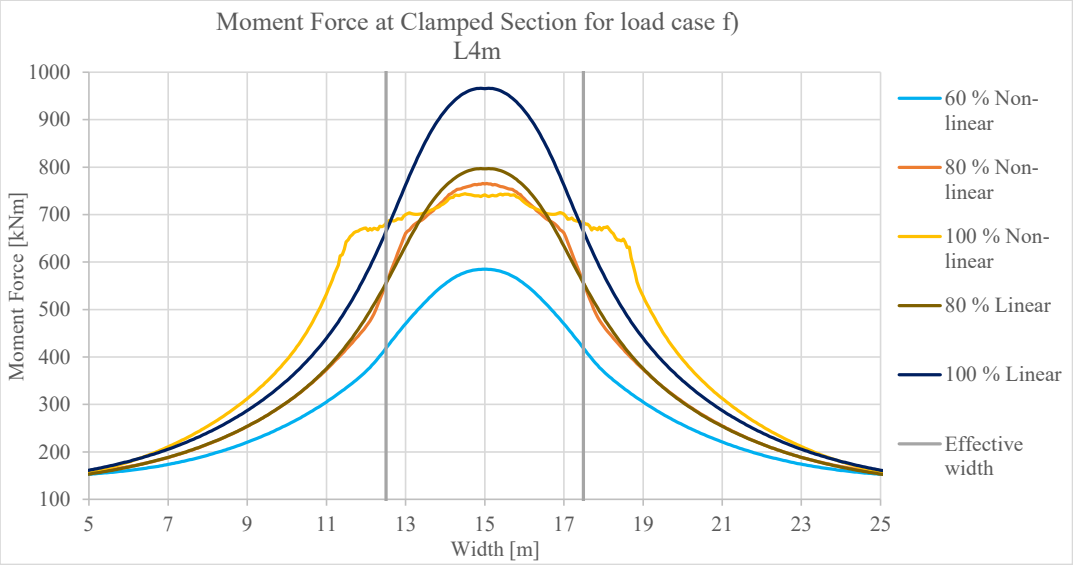

Figure 5.29: Moment distribution for case L4m subjected to load case f). Utilization ratio of maximum load capacity in non-linear analysis and distribution from linear analysis with corresponding load levels. The effective width used in linear analysis is presented.

5.5.1 Fluctuations in shear force distribution

Figure 5.30 shows the shear force distribution for load case f) in geometry L4m. The non-linear results are presented at 60 % and 100 % of the ultimate load, alongside the corresponding distribution from the linear analysis. While the linear analysis yielded a relatively smooth shear distribution, the non-linear results exhibited distinct local fluctuations along the evaluated critical section.

Figure 5.30: Shear force distribution for geometry L4m under load case f), comparing linear and non-linear FE analyses.

The irregular shear force pattern in the non-linear model correlated with the development of transverse cracking in the slab. Figure 5.31 shows the crack pattern and tensile strains for the same geometry and load case at 90 % of the maximum load. The areas of high tensile strain correspond with the location of longitudinal cracks (crack opening in the longitudinal direction).

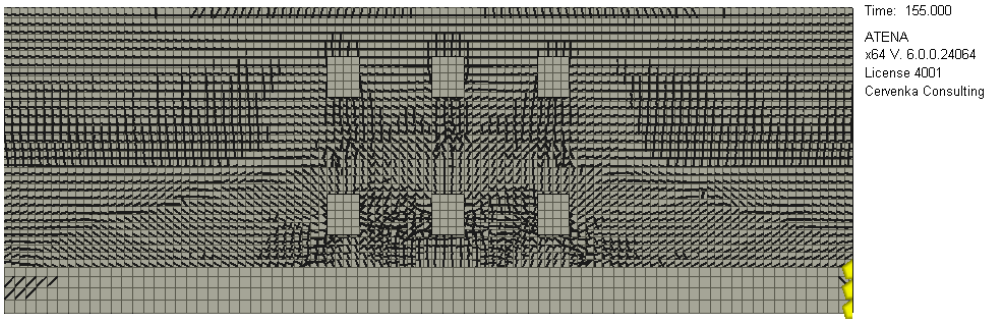

(a) Crack pattern.

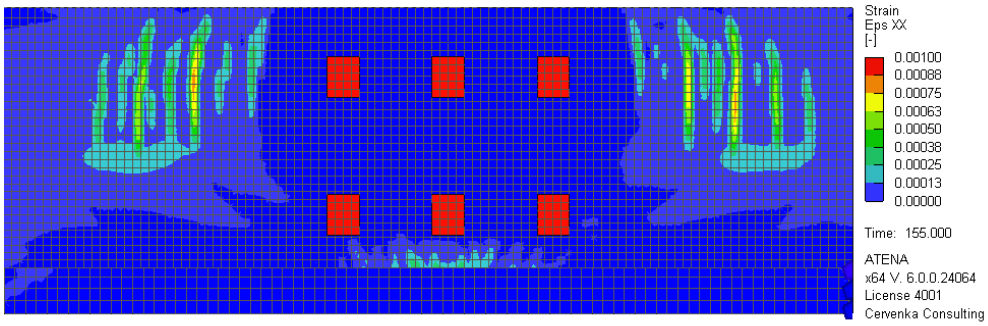

(b) Tensile strain

Figure 5.31: Overview of the slab subjected to load case f) with 90 % of maximum load.

The onset of these cracks affected the shear transfer locally, resulting in the observed fluctuations in the shear force distribution. As the load increased and deflections grew, the cracking became more pronounced, further amplifying the variation in shear forces. These fluctuations were observed across all geometries.

Despite these local variations, the overall trend of the non-linear shear distribution in Figure 5.30 aligned relatively well with the linear results, even at maximum load. In the case shown in the figure, the non-linear analysis indicated failure due to moment, at which point the shear distribution still resembled that of the linear analysis. This trend held for all cases where moment governs the failure.

5.5.2 Loading history

To evaluate the influence of load history on structural behaviour, the non-linear FE models, both the solid and shell element types, were subjected to prior loading. This preloading was applied as a bogie-type configuration, corresponding to load case c), and consisted of 13 load positions along the slab with 1.3 m spacing. The load magnitude was representative for SLS conditions, with a maximum B value of around 75 % of the load-bearing capacity, a load large enough to cause cracks along the slab with a crack width of 0.1 mm. This procedure aimed to simulate accumulated damage and stiffness degradation due to earlier or repeated service loads. Figure 5.32 shows the solid model with loading plates an the refined mesh in the midsection where the final load is applied to failure.

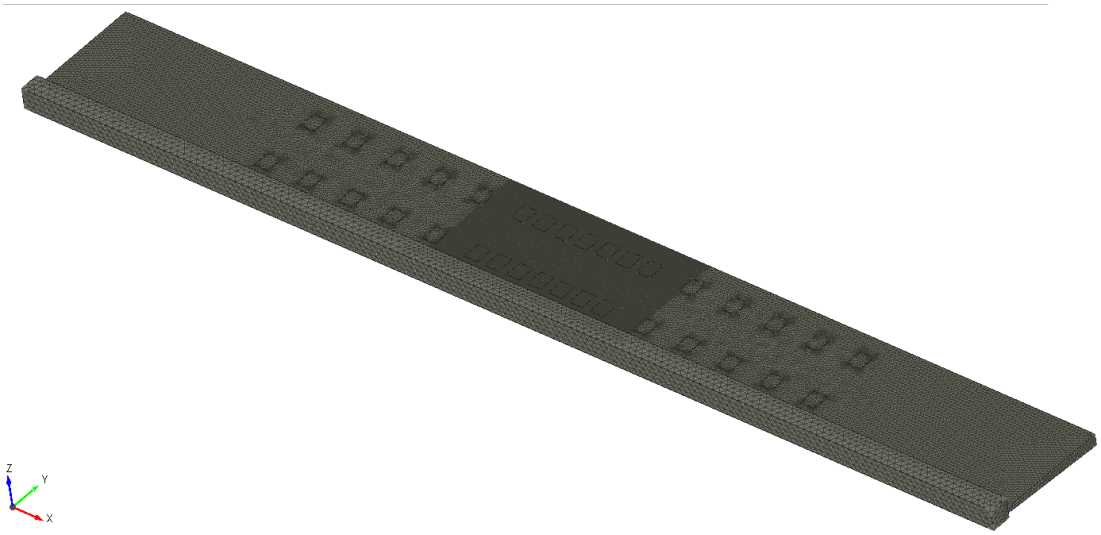

Figure 5.32: Meshed model.

The impact of this load history on the global response is illustrated in Figure 5.33, which shows the load–deflection behaviour for the solid element model with and without prior loading. Deflection was measured as the maximum vertical displacement along the edge beam, while the applied load represents the total support reactions, including self-weight. In the preloaded model, the self-weight was applied under SLS conditions, whereas in the model without prior loading, self-weight was included in the ULS load combination using a factor of 1.2. The steps in the two loading procedures are illustrated in Figure 4.16 and 4.17.

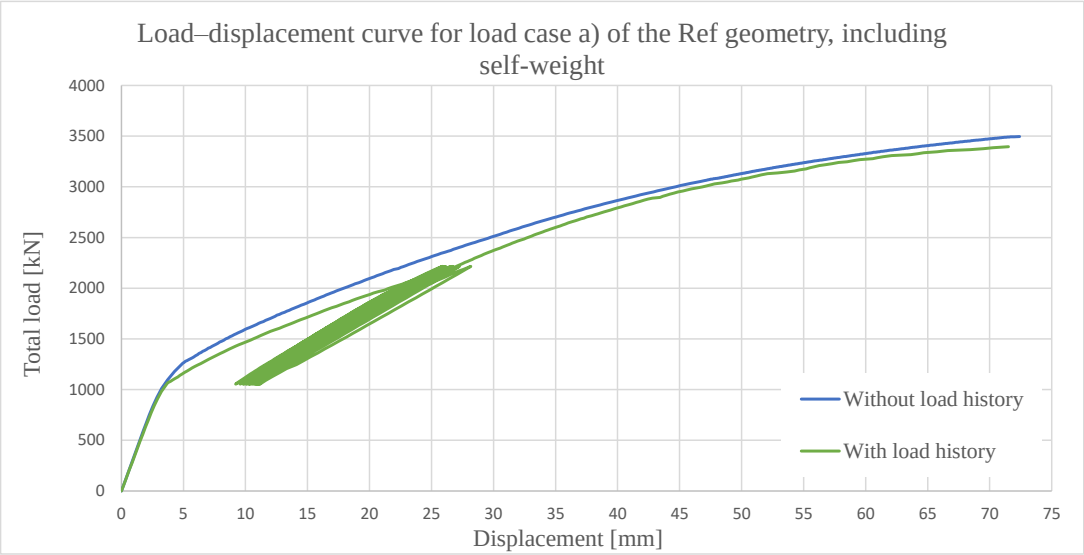

Figure 5.33: Displacement of the cantilever slab subjected to load case a) with and without load history.

Initially, the model with load history exhibited reduced stiffness, resulting in greater deflections at lower load levels. As the load was increased, the two curves converged, and at ultimate failure both models reached similar maximum displacements. This indicated that while load history affects the initial stiffness and crack development, its impact on ultimate load-bearing capacity was limited in the solid element model. However, in the shell element model, see Figure 5.34, the ultimate load was reduced by approximately 8% due to the inclusion of loading history. Furthermore, the deflections at corresponding load levels were consistently higher compared to the model without prior loading.

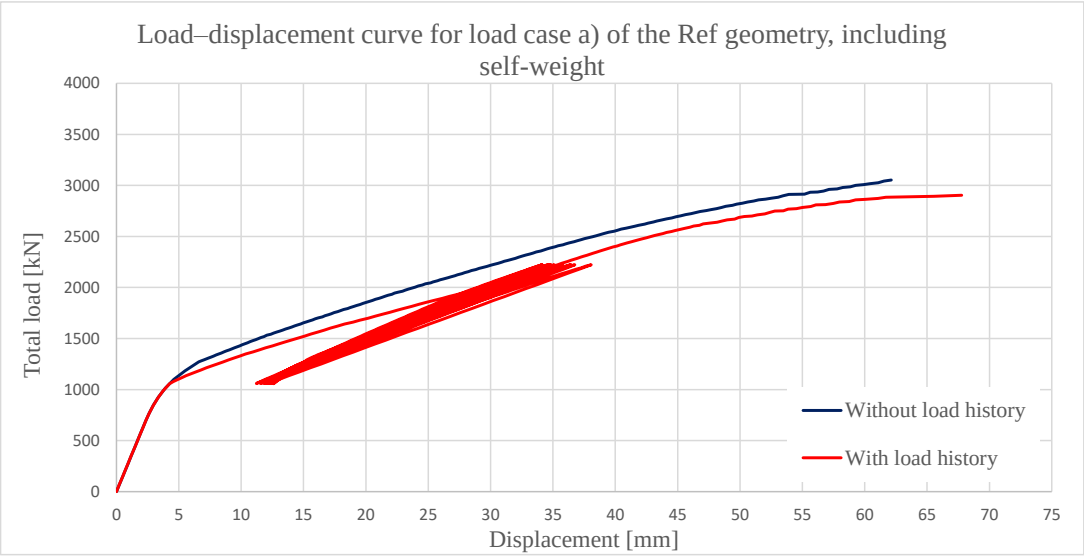

Figure 5.34: Displacement of the cantilever slab subjected to load case a) with and without load history.

The reinforcement stresses in the solid element model also reflected the effects of loading history, as shown in Figure 5.35. These results refer to the stress state caused solely by self-weight, both before and after the preloading step. Prior to the application of load history, the maximum reinforcement stress from self-weight was 45 MPa. After the model had been subjected to preloading, this stress increased to 145 MPa under the same self-weight condition, indicating a permanent shift due to cracking and stiffness degradation. During the preloading phase itself, reinforcement stresses reached up to 480 MPa, compared to the yielding stress of 682 MPa in the model.

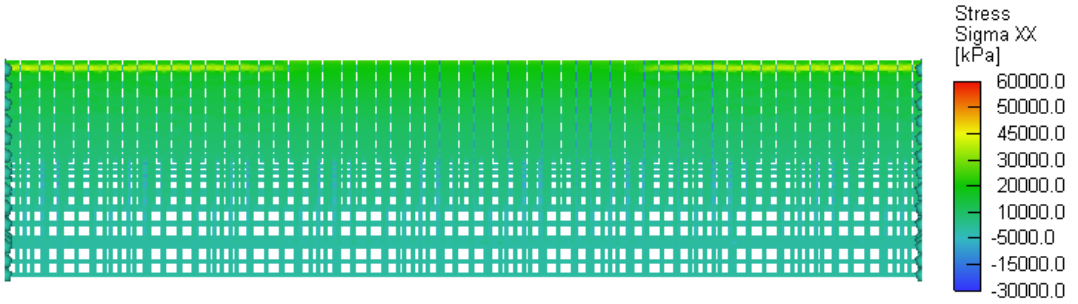

(a) Before loading history

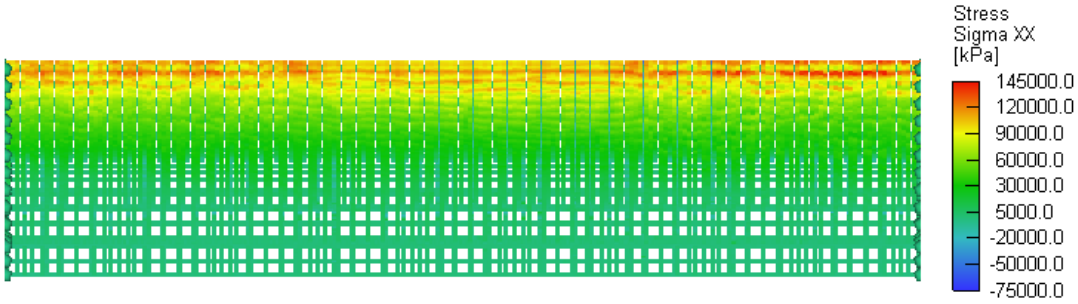

(b) After loading history

Figure 5.35: Reinforcement stresses subjected to self-weight.

The increase in reinforcement stress corresponds to wider cracks formed during the preloading phase. As cracking occurred, tension previously carried by the concrete was progressively transferred to the reinforcement. Increased cracking near the support caused more of the tension force to be carried by the reinforcement bars. Figure 5.36 shows the crack width before and after the load history, with a significant increase from 0.0155 mm to 0.124 mm.

(a) Before loading history

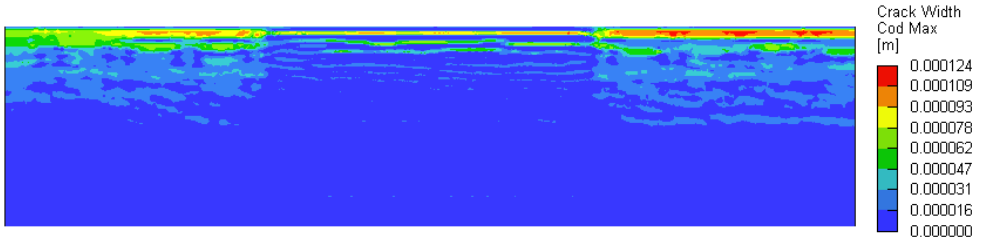

(b) After loading history

Figure 5.36: Crack width in slab subjected to self-weight.

The crack widths in Figure 5.36 exhibit varying distributions and widths depending on the mesh size. Larger elements show cracks distributed over a broader area with slightly greater width compared to finer meshes. Conversely, slabs with finer mesh configurations display narrower and more localized cracks. Particularly for slabs subjected solely to self-weight before the load history, crack widths vary depending on the mesh size. However, these cracks are relatively small, resulting in minimal significant differences that have no real effect.

In the shell element model, the shear force distribution exhibited more fluctuation compared to the model without load history. This behaviour can be attributed to increased cracking in the slab, which alters the internal stiffness and affects how shear forces are transferred. The shear forces became marginally more concentrated around certain regions, particularly near the load application points, producing a wider plateau. However, the overall distribution pattern remained very similar to the model without load history.

The changes in moment distribution were also minor, but slightly more apparent than in the shear force case. Figure 5.37 shows the moment distribution along the support for the reference geometry at 80% of the maximum capacity in the model without load history, allowing a direct comparison. In the model with load history, a small increase in moment concentration near the midspan can be observed.

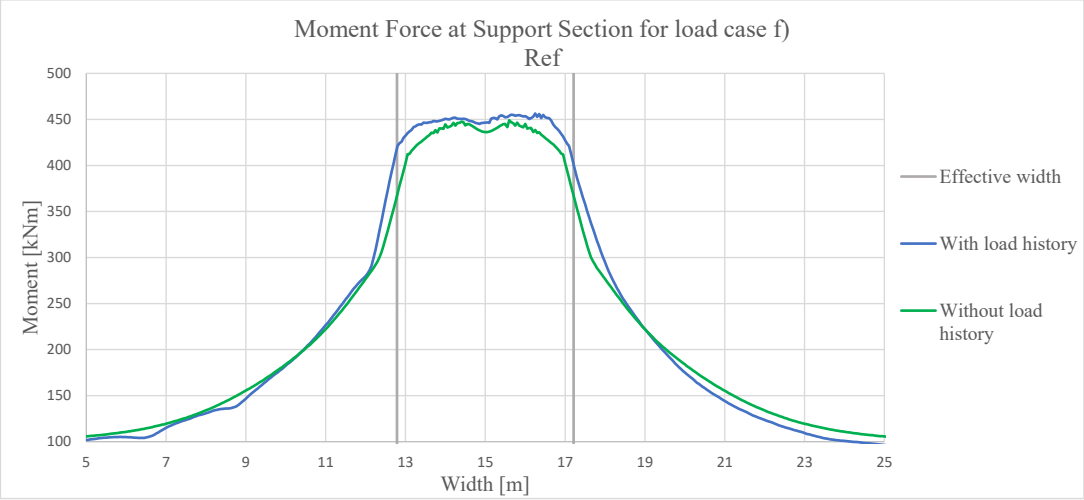

Figure 5.37: The moment distribution along the support for the reference geometry subjected to load case f) at 80% of the maximum load in the model without load history.

6 Discussion and Conclusions

This chapter presents a discussion about results obtained in this thesis. The main conclusions are also presented, as well as suggestions for future work.

6.1 Discussion

The results of this study highlight the significance of model complexity in evaluating load distribution, structural capacity, and failure modes in RC overhang slabs. Simplified methods, such as hand calculations, offer conservative estimates compared to the non-linear analyses, but are unable to capture the redistribution of internal forces following cracking and reinforcement yielding. Linear FE models improve the accuracy in force distribution, even if it does not account for cracking. The capacity was increased in most cases for the linear models compared to the hand calculations, with the exception for the geometries NoEdge and t+0.1. The reduction of stiffness in the transversal direction by 40% made the linear model match the non-linear model force distribution up to reinforcement yielding relatively accurate. Once yielding initiates, the non-linear FE model demonstrates the slab's ability to redistribute loads, particularly the moment distribution, and to significantly increase its load-carrying capacity as illustrated in Figure 5.1. Notably, both hand calculations and linear models predict shear failure as the governing failure mode for most load cases and geometries, whereas non-linear FE analyses identified moment or punching failure often governs.

There are several simplifications made in the non-linear analyses in order to make the model manageable with reasonable computational cost. The number of elements used was a limiting factor in terms of computational cost, especially for the solid element model. Since the model was relatively large and the need to have several elements under the load plates to accurately capture the shear behaviour using element models, a model with finer elements at the loading plates and larger for the rest of the model was used. One important simplification is that the cantilever slab was considered fully fixed along the vertical support, not allowing rotation or any deflection vertically at the support. In reality, however, it is reasonable to assume that the slab will experience deflection in the vertical direction due to the deflection of the main girder, meaning that the boundary conditions are less rigid than assumed. This simplification may lead to an overestimation of the slab's stiffness, as the flexibility in the longitudinal direction is not fully captured. It can therefore be assumed that allowing the cantilever to deflect more would increase the load-bearing capacity by enabling greater load redistribution in the longitudinal direction.

Regarding the choice of safety format in the non-linear analyses, the GRF method was applied, primarily due to its practical advantages. It requires only one analysis per load combination and utilizes mean material properties, making it computationally efficient. As described in Section 3.3.8, a model uncertainty factor of 1.06, which was used for this report, is typically used for for failure modes characterized by low modelling uncertainty, whereas for for failure in shear and punching shear, a higher model uncertainty factor is commonly used. However, in order to better capture the difference between the different analyses, the same model uncertainty factor was used, regardless of failure mode. For failure modes governed by shear, particularly in load cases with fewer applied loads, the ECOV method would have been more appropriate due to its ability

to capture the influence of variation in the material properties on the design resistance. Nonetheless, due to the substantial reduction in computational effort offered by the GRF method, it was chosen for all non-linear analyses in this study.

As the linear models predominantly predict shear failure, and considering the higher modelling uncertainty associated with shear, the question arises whether the non-linear model is capable of accurately capturing this failure mode. Although the mesh was refined around the applied loads and the number of elements through the slab thickness should be sufficient to capture the governing mechanisms, the complexity of shear failure in reinforced concrete remains a modelling challenge. To better verify the models ability to represent shear behaviour, it would be beneficial to replicate previous experimental tests, as the one described in Section 2.5 which failed in shear, and compare the results with the observed structural responses.

According to Trafikverket (2023a), the required assessment range for wheel spacing is 1.7 m to 2.3 m. Since the focus of this study was to investigate different assessment levels on different geometries and how the load capacity and distribution change for each level, only the minimum spacing (1.7 m) was used. For load case a), representing a single axle load, the observed failure mode in the non-linear analysis was predominantly punching shear failure for the outer wheel pair, especially in slab geometries with a tapered slab. This is consistent with results from previous experimental testing (ref). Had the maximum spacing (2.3 m) been applied, the outer wheel pair would have shifted 0.3 m closer to the edge beam. For slabs with tapered thickness, this shift implies a thinner slab section under the load and shorter punching perimeter. Both of which reduce punching shear resistance. This effect is particularly evident for the tapered slab type, which showed lower capacity and earlier punching failure in the non-linear analysis.

An important observation can be made for the tConst geometry, which features a constant thickness along the slab. Unlike the other geometries with tapered thickness, tConst consistently exhibits moment failure in the non-linear analyses and shows a tendency towards moment-governed behaviour also in hand calculations and linear FE models. While shear failure is still predicted in several linear cases, the margin to moment failure is significantly smaller compared to the other geometries. Furthermore, for load case a), all other geometries exhibit punching failure in the non-linear model, whereas tConst does not. Additional differences between geometries can also be observed, for instance, the comparison between Ref and L2m showed that the shorter slab experiences a more concentrated shear distribution, as shown in Figure 5.17. However, both of these findings are in line with expectations based on the geometric configurations.

6.2 Conclusions

Hand calculations and linear finite element models provide conservative estimates of load-carrying capacity when compared to non-linear analysis. While suitable for preliminary design or safety checks, they do not reflect the full structural response beyond yielding. Conclusions in summary from this report:

- The equations used to determine the effective width used for moment calculations in the hand calculations is conservative, but captures the impact of the edge beam. However, for shear, the hand calculations fails to capture the edge beams

contribution to stiffness and load distribution since it is only regarded as a dead weight.

- Linear FE models with a 40% reduction in transverse stiffness, combined with the effective width method from Pacoste et al. (2012), provide a conservative and simplified approximation of moment distribution and load-bearing capacity. However, non-linear models demonstrate the slab's ability to redistribute bending moments beyond the limits of the effective width, ultimately resulting in a significantly higher failure load.
- The shear force distribution in the linear FE model aligns reasonably well with the non-linear shell element model up to the point of reinforcement yielding. However, the non-linear analysis shows a generally wider spread of shear forces, reflecting the redistribution enabled by cracking and stiffness degradation. Notably, the solid element model does not exhibit shear failure along the critical inner section, despite the linear model predicting such a failure. These findings suggest that non-linear solid models indicate a higher shear capacity in cantilever slabs than what is predicted by linear FE models using local resistance models based on beam theory without shear reinforcement. This highlights the limitations of simplified approaches, such as hand calculations and linear FE models, in accurately capturing the full shear-carrying mechanism in RC slabs without shear reinforcement.
- Non-linear analysis reveals that reinforced concrete overhang slabs are capable of significant increased load-carrying capacity, allowing internal forces to redistribute after reinforcement yielding. As a result, these structures can sustain considerably higher loads than predicted by conventional linear or code-based methods.
- The loading history in the non-linear model primarily affected deflection and crack widths in the serviceability limit state, but had no significant impact on the load distribution, ultimate load-bearing capacity, or final deflection. The shell element model showed a greater sensitivity to load history compared to the solid element model. Although load history analyses require considerable amount of computation time, their influence on the final load distribution, ultimate bearing capacity, and deflection is limited.

6.3 Suggestions for further work

- To ensure that the model can capture shear failure, an aspect that is particularly challenging in non-linear FE analysis, the non-linear model could be validated against experimental test results to verify its accuracy. Also adjust the model for the stiffness in rotation and the vertical displacement at the support to account for the global response from the bridge.
- Study how long term effects as creep and shrinkage influence the force distributions and load bearing capacity.
- Investigate how the distribution and capacity change if the distance between the wheels are varied between 1.7 and 2.3 m, and how it is influenced by the different assessment levels.

7 References

Al-Emrani, M., Engström, B., Johansson, M., & Johansson, P. (2013). *Bärande konstruktioner – del 1*. Chalmers Tekniska Högskola.

Boverket. (2024). Utsläpp av växthusgaser från bygg- och fastighetssektorn [Accessed: 2025-01-22]. https://www.boverket.se/sv/byggande/hallbart-byggande-och-forvaltning/miljoindikatorer---aktuell-status/vaxthusgaser/

CEB-FIP. (1993). *Ceb-fip model code 1990*. Thomas Telford Ltd.

CEB-FIP. (2013). *Fib model code for concrete structures 2010*. International Federation for Structural Concrete (fib).

Cervenka, V., Cervenka, J., & Pukl, R. (2007). Safety assessment in fracture analysis of concrete structures. *Proceedings of the 6th International Conference on Fracture Mechanics of Concrete and Concrete Structures*, *2*, 1043–1049.

Cervenka Consulting. (2025). ATENA (Version 2024) [Software]. https://www.cervenka.cz/products/atena/

Davidsson, M. (2003). *Strukturanalys av brokonstruktioner med finita elementmetoden – fördelning av krafter och moment* (Technical Report). Brosamverkan Väst. Göteborg.

EN 1992-1-1. (2008). *Eurocode 2: Design of concrete structures - part 1-1: General rules and rules for buildings*. Swedish Standards Institute.

EN 1992-2. (2005). *Eurocode 2: Design of concrete structures - part 2: Concrete bridges - design and detailing rules*. Swedish Standards Institute.

Engström, B. (2014). *Design and analysis of slabs and flat slabs* (Report 2011-5, Edition 2014) [ISSN 1652-9162]. Chalmers University of Technology.

Engström, B. (2015). *Design and analysis of continous beams and columns* (Report 2007-3, Edition 2015) [ISSN 1652-9162]. Chalmers University of Technology.

Hendriks, M., de Boer, A., & Belletti, B. (2017). *Guidelines for nonlinear finite element analysis of concrete structures* (tech. rep. No. RTD:1016-1:2017). Rijkswaterstaat Centre for Infrastructure. Netherlands. https://www.researchgate.net/publication/287737905

Muñoz, J. J. V. (2020). *Bridge overhang slabs with edge beams: Lcca and structural analysis for the development of new concepts* [Doctoral Thesis in Structural Engineering and Bridges]. KTH Royal Institute of Technology [TRITA-ABE-DLT-2037].

Muñoz, J. J. V., Pacoste, C., & Karoumi, R. (2023). Assessment of effective and minimal slab widths for evaluating the shear capacity of rc overhang slabs. *Nordic Concrete Research*, *68*(1), 64–85. https://doi.org/10.2478/ncr-2023-0003

Muttoni, A., & Fernández Ruiz, M. (2008). Shear strength of members without transverse reinforcement as function of critical shear crack width. *ACI Structural Journal*, *105*(2), 163–172.

Muttoni, A., & Simões, J. T. (2023). Shear and punching shear according to the critical shear crack theory: Background, recent developments and integration in codes. *Revista IBRACON de Estruturas e Materiais*, *16*(3), e16302. https://doi.org/10.1590/S1983-41952023000300002

Natanaelsson, K., & Eriksson, T. (2020). *Implementering av bärighetsklass 4* (Technical Report). Trafikverket.

Pacoste, C., Plos, M., & Johansson, M. (2012). *Recommendations for finite element analysis for the design of reinforced concrete slabs* (Technical Report). Royal Institute of Technology. Stockholm, Sweden.

Plos, M. (2000). *Finite element analyses of reinforced concrete structures*. Chalmers University of Technology.

Plos, M., Johansson, M., Zandi, K., & Shu, J. (2021). *Recommendations for assessment of reinforced concrete slabs: Enhanced structural analysis with the finite element method* (tech. rep. No. ACE 2021:3). Chalmers University of Technology, Department of Architecture and Civil Engineering, Division of Structural Engineering. Gothenburg, Sweden.

Plos, M., Shu, J., Zandi, K., & Lundgren, K. (2017). A multi-level structural assessment strategy for reinforced concrete bridge deck slabs. *Structure and Infrastructure Engineering*, *13*(2), 223–241. https://doi.org/10.1080/15732479.2016.1162177

PTC. (2025). Mathcad Prime (Version 10.0.0) [Software]. https://www.mathcad.com

Reissen, K., & Hegger, J. (2016). Experimental investigations on the effective width for shear. *Proceedings of IABMAS 2016, 8th International Conference on Bridge Maintenance, Safety and Management*.

Setiawan, A., Cantone, R., Ruiz, M. F., & Muttoni, A. (2024). Verification of shear failures of cantilever bridge deck slabs subjected to concentrated loads. *Engineering Structures*, *303*, 117491. https://doi.org/10.1016/j.engstruct.2024.117491

Shu, J., Plos, M., Zandi, K., & Ashraf, A. (2019). Distribution of shear force: A multi-level assessment of a cantilever rc slab. *Engineering Structures*, *190*, 345–359. https://doi.org/10.1016/j.engstruct.2019.04.045

Statens Betongkommitté. (1968). *B7, bestämmelser för betongkonstruktioner: Allmänna konstruktionsbestämmelser*.

Strusoft. (2025). FEM-Design (Version 23) [Software]. https://www.strusoft.com

Trafikverket. (2023a). *Bro och broliknande konstruktion, bärighetsberäkning* (Technical Report). Trafikverket.

Trafikverket. (2023b). Så sköter vi broar och tunnlar [Accessed: 2025-01-22]. https://www.trafikverket.se/resa-och-trafik/underhall/sa-skoter-vi-broar-och-tunnlar/

Vaz Rodriguez, R. (2007). *Shear strength of reinforced concrete bridge deck slabs* [PhD thesis]. École Polytechnique Fédérale de Lausanne.

Vaz Rodriguez, R., Fernández Ruiz, M., & Muttoni, A. (2008). Shear strength of r/c bridge cantilever slabs. *Engineering Structures*, *30*, 3024–3033. https://doi.org/10.1016/j.engstruct.2008.04.017

Appendix A- Hand calculations example

This appendix provides a calculation example of the maximum B-value of a specific load case

Geometry parameters:

$L := 3.2\ m$ $b := 1\ m$

$h_{sup} := 0.33\ m$ $h_{edge} := 0.16\ m$

$\phi := 16\ mm$ $\phi' := 10\ mm$

$A_s := \frac{1\ m}{85\ mm} \cdot \left(\frac{\phi}{2}\right)^2 \cdot \pi$ $A_{s\_z} := \frac{1\ m}{300\ mm} \cdot \left(\frac{\phi'}{2}\right)^2 \cdot \pi$

$A'_s := \frac{1\ m}{300\ mm} \cdot \left(\frac{\phi'}{2}\right)^2 \cdot \pi$ $A'_{s\_z\_1} := \frac{1\ m}{290\ mm} \cdot \left(\frac{\phi'}{2}\right)^2 \cdot \pi$ $A'_{s\_z\_2} := \frac{1\ m}{250\ mm} \cdot \left(\frac{\phi'}{2}\right)^2 \cdot \pi$

$c_{cover\_top} := \max(20\ mm, 1.5 \cdot \phi) = 0.024\ m$

Concrete cover

$c_{cover\_bottom} := \max(20\ mm, 1.5 \cdot \phi') = 0.02\ m$

$h_{edgebeam} := 0.6\ m$ $w_{edgebeam} := 0.565\ m$ $h_{surface} := 0.1\ m$ $\rho_{surf} := 22\ \frac{kN}{m^3}$

Material parameters:

Concrete

$f_{ck} := 35.5\ MPa$ $\gamma_c := 1.5$ $f_{cd} := \frac{f_{ck}}{\gamma_c} = 23.667\ MPa$

$E_{ck} := 34\ GPa$ Class K50

$\rho_c := 25\ \frac{kN}{m^3}$

Reinforcement:

$f_{yk} := 620\ MPa$ $\gamma_s := 1.15$ $f_{yd} := \frac{f_{yk}}{\gamma_s} = 539.13\ MPa$ $E_s := 200\ GPa$

Wheel distance:

$b_{wheel} := 0.2\ m$ $l_{wheel} := 0.3\ m$ $cc_{wheel} := 1.7\ m$

$L_{lane} := 3\ m$ $\gamma_{traffic} := 1.5$

$\alpha_{wheel} := \begin{bmatrix} L - \frac{(L_{lane} + cc_{wheel} + l_{wheel})}{2} \\ L - \frac{(L_{lane} + l_{wheel} - cc_{wheel})}{2} \end{bmatrix} = \begin{bmatrix} 0.7 \\ 2.4 \end{bmatrix} m$ Distance from support to each wheel

Shear:

The shear is checked at two critical section, at a distance 0,5d from each wheel pair

A coordinate system is defined with x=0 at the connection between slab and edgebeam.

Capacity section 1:

$$h_{wheel\_1} := h_{edge} + \frac{h_{sup} - h_{edge}}{L} \cdot \left(L - \alpha_{wheel_0}\right) = 0.293\ m$$

$$d_{wheel\_1} := h_{wheel\_1} - c_{cover\_top} - \frac{\phi}{2} = 0.261\ m$$

$$x_{crit\_1} := L - \alpha_{wheel_0} + 0.5 \cdot d_{wheel\_1} + h_{surface} = 2.73\ m$$

$$h_{crit\_1} := h_{edge} + \left(h_{sup} - h_{edge}\right) \cdot \frac{x_{crit\_1}}{L} = 0.305\ m$$

$$d_{crit\_1} := h_{crit\_1} - c_{cover\_top} - \frac{\phi}{2} = 0.273\ m$$ Effective height at critical section

$$C_{Rd\_c} := \frac{0.18}{\gamma_c} = 0.12$$

$$k_1 := min\left(1 + \left(\frac{200}{\frac{d_{crit\_1}}{mm}}\right)^{\frac{1}{2}}, 2\right) = 1.856$$

$$\rho_{l\_1} := min\left(\frac{A_s + A'_s}{b \cdot d_{crit\_1}}, 0.02\right) = 0.01$$

$$V_{Rd\_c\_1} := C_{Rd\_c} \cdot k_1 \cdot \left(100 \cdot \rho_{l\_1} \cdot \frac{f_{ck}}{MPa}\right)^{\frac{1}{3}} \cdot \frac{b}{mm} \cdot \frac{d_{crit\_1}}{mm} \cdot N = 197.3\ kN$$

$$V_{Rd\_c\_min\_1} := 0.035 \cdot k_1^{\frac{3}{2}} \cdot \left(\frac{f_{ck}}{MPa}\right)^{\frac{1}{2}} \cdot \frac{b}{mm} \cdot \frac{d_{crit\_1}}{mm} \cdot N = 143.959\ kN$$

$$V_{Rd\_c\_crit\_1} := \max\left(V_{Rd\_c\_min\_1}, V_{Rd\_c\_1}\right) = 197.3\ kN$$

Capacity section 2:

$$h_{wheel\_2} := h_{edge} + \frac{h_{sup} - h_{edge}}{L} \cdot \left(L - \alpha_{wheel_1}\right) = 0.203\ m$$

$$d_{wheel\_2} := h_{wheel\_2} - c_{cover\_top} - \frac{\phi}{2} = 0.171\ m$$

$$x_{crit\_2} := L - \alpha_{wheel_1} + 0.5 \cdot d_{wheel\_2} + h_{surface} = 0.985\ m$$

$$h_{crit\_2} := h_{edge} + \left(h_{sup} - h_{edge}\right) \cdot \frac{x_{crit\_2}}{L} = 0.212\ m$$

$$d_{crit\_2} := h_{crit\_2} - c_{cover\_top} - \frac{\phi}{2} = 0.18\ m$$ Effective height at critical section

$$k_2 := min\left(1 + \left(\frac{200}{\frac{d_{crit\_2}}{mm}}\right)^{\frac{1}{2}}, 2\right) = 2$$

$$\rho_{l\_2} := min\left(\frac{\frac{2}{3} A_s + A'_s}{b \cdot d_{crit\_2}}, 0.02\right) = 0.01$$

$$V_{Rd\_c\_2} := C_{Rd\_c} \cdot k_2 \cdot \left(100 \cdot \rho_{l\_2} \cdot \frac{f_{ck}}{MPa}\right)^{\frac{1}{3}} \cdot \frac{b}{mm} \cdot \frac{d_{crit\_2}}{mm} \cdot N = 143.172\ kN$$

$$V_{Rd\_c\_min\_2} := 0.035 \cdot k_2^{\frac{3}{2}} \cdot \left(\frac{f_{ck}}{MPa}\right)^{\frac{1}{2}} \cdot \frac{b}{mm} \cdot \frac{d_{crit\_2}}{mm} \cdot N = 106.371\ kN$$

$$V_{Rd\_c\_crit\_2} := \max\left(V_{Rd\_c\_min\_2}, V_{Rd\_c\_2}\right) = 143.172\ kN$$

Calculation of B-value, section 1:

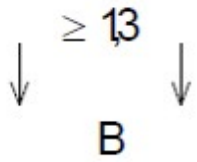

This calculation example uses the third load case in Figure 4.4.

Effective width d/2 from the load:

$$x_1 := \frac{d_{wheel\_1}}{2} + \frac{l_{wheel}}{2} = 0.28\ m$$

$$b_{eff\_1} := \max\left(7 \cdot d_{wheel\_1} + b_{wheel} + c_{cover\_top},\ 10 \cdot d_{wheel\_1} + 1.3 \cdot x_1\right) = 2.973\ m$$

A distribution factor is defined as the total load of the load case divided by the length over which it is distributed when taking Figure 3.3 into account

$$Length_1 := 1.3\ m + b_{eff\_1} = 4.273\ m \qquad B := 1$$

$$\chi_{shear\_1} := \frac{B}{Length_1} = 0.234\ \frac{1}{m}$$

Dynamic factor:

$$v := 80 \quad \left[\frac{km}{h}\right]$$

$$D := \frac{180 + 8 \cdot (v - 10)}{20 + \frac{L}{m}} \cdot \frac{1}{100} = 0.319$$

The shear in the critical section is calculated with:

$$Q_{B\_shear} \cdot \chi_{shear} \cdot \frac{V_{crit}}{100\ kN} \cdot (1 + D) \cdot \gamma_{traffic} + V_{self}$$

V_{crit} is the shear force in the critical section from a load of B=100 kN:

$$V_{crit\_1} := 100\ kN$$

Shear in critical section from self-weight: $\gamma_{self} := 1.2$

$$q_{edge} := \rho_c \cdot b \cdot h_{edge} \cdot \gamma_{self} \qquad q_{sup} := \rho_c \cdot b \cdot h_{sup} \cdot \gamma_{self}$$

$$V_{self\_slab\_1} := q_{edge} \cdot x_{crit\_1} + \frac{\left(q_{sup} - q_{edge}\right) \cdot x_{crit\_1}}{2} = 20.068\ \textbf{kN}$$

$$V_{self\_edgebeam} := b \cdot h_{edgebeam} \cdot w_{edgebeam} \cdot \rho_c \cdot \gamma_{self} = 10.17\ \textbf{kN}$$

$$V_{self\_surf\_1} := h_{surface} \cdot x_{crit\_1} \cdot \rho_{surf} \cdot b = 6.007\ \textbf{kN}$$

$$V_{self\_1} := V_{self\_slab\_1} + V_{self\_edgebeam} + V_{self\_surf\_1} = 36.245\ \textbf{kN}$$

Maximum characteristic value of B in critical section 1 for the specific load case:

$$Q_{B\_shear\_1} := \frac{V_{Rd\_c\_crit\_1} - V_{self\_1}}{\chi_{shear\_1} \cdot \textbf{m} \cdot \frac{V_{crit\_1}}{100\ \textbf{kN}} \cdot \left(1 + D\right) \cdot \gamma_{traffic}} = 347.814\ \textbf{kN}$$

Calculation of B-value, section 2:

Effective width d/2 from the load:

$$x_2 := \frac{d_{wheel\_2}}{2} + \frac{l_{wheel}}{2} = 0.235\ \textbf{m}$$

$$b_{eff\_2} := \max\left(7 \cdot d_{wheel\_2} + b_{wheel} + c_{cover\_top}, 10 \cdot d_{wheel\_2} + 1.3 \cdot x_2\right) = 2.011\ \textbf{m}$$

Distribution factor:

$$Length_2 := 1.3\ \textbf{m} + b_{eff\_2} = 3.311\ \textbf{m}$$

$$\chi_{shear\_2} := \frac{B}{Length_2} = 0.302\ \frac{1}{\textbf{m}}$$

shear force in the critical section from a load of B=100 kN:

$$V_{crit\_2} := 50\ \textbf{kN}$$

Shear in critical section from self-weight:

$$V_{self\_slab\_2} := q_{edge} \cdot x_{crit\_2} + \frac{\left(q_{sup} - q_{edge}\right) \cdot x_{crit\_2}}{2} = 7.242\ \textbf{kN}$$

$$V_{self\_surf\_2} := h_{surface} \cdot x_{crit\_2} \cdot \rho_{surf} \cdot b = 2.168 \ \textbf{kN}$$

$$V_{self\_2} := V_{self\_slab\_2} + V_{self\_edgebeam} + V_{self\_surf\_2} = 19.579 \ \textbf{kN}$$

Maximum characteristic value of B in critical section 2 for the specific load case:

$$Q_{B\_shear\_2} := \frac{V_{Rd\_c\_crit\_2} - V_{self\_2}}{\chi_{shear\_2} \cdot \boldsymbol{m} \cdot \frac{V_{crit\_2}}{100 \ \textbf{kN}} \cdot (1 + D) \cdot \gamma_{traffic}} = 413.653 \ \textbf{kN}$$

Punching shear:

Punching shear is evaluated by using a control perimeter which is taken at a distance 2,0d around the loaded area.

First, punching is evaluated by considering each wheel load separetely, regardless if the control perimeters overlap. Then, overlapping of control perimeters is considered. This is shown in the following figures:

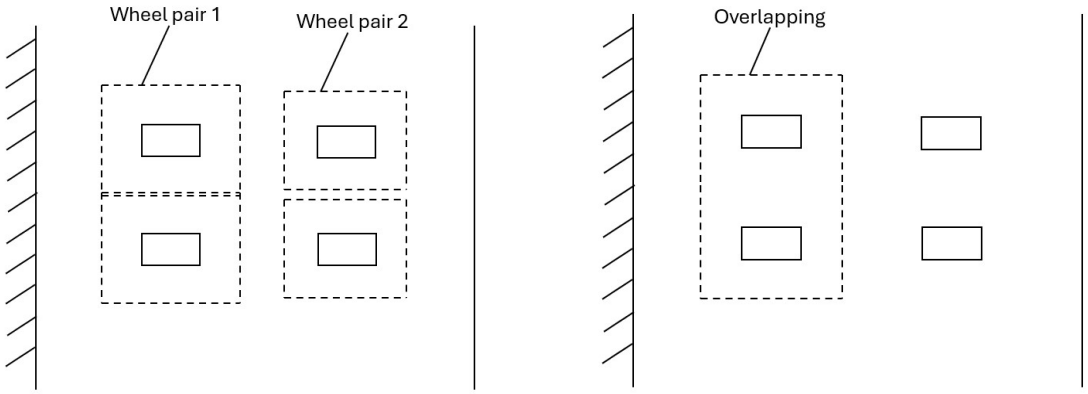

Capacity at wheel pair 1:

$$C_{Rd\_c} := \frac{0.18}{\gamma_c} = 0.12$$

$$h_1 := 0.16\ m + \frac{2.35}{3.2} \cdot (0.33 - 0.16)\ m = 0.285\ m$$

$$d_{y\_1} := h_1 - c_{cover\_top} - \frac{\phi}{2} = 0.253\ m$$ Effective depth in transversal direction

$$d_{z\_1} := h_1 - c_{cover\_top} - \phi - \frac{\phi'}{2} = 0.24\ m$$ Effective depth in longitudinal direction

$$d_{ef\_1} := \frac{d_{y\_1} + d_{z\_1}}{2} = 0.246\ m$$ The height of the control perimeter is taken as the effective depth

$$k_1 := min\left(1 + \left(\frac{200}{\frac{d_{ef\_1}}{mm}}\right)^{\frac{1}{2}}, 2\right) = 1.901$$

$$\rho_{y\_1} := \frac{A_s + A'_s}{d_{y\_1} \cdot b} = 0.0104$$ Reinforcement ratio in transversal direction

$$\rho_{z\_1} := \frac{A_{s\_z} + A'_{s\_z\_1}}{d_{z\_1} \cdot b} = 0.0022$$ Reinforcement ratio in longitudinal direction

$$\rho_{l\_1} := min\left(\sqrt{\rho_{y\_1} \cdot \rho_{z\_1}}, 0.02\right) = 0.0048$$

$$v_{Rd\_c\_1} := C_{Rd\_c} \cdot k_1 \cdot \left(100 \cdot \rho_{l\_1} \cdot \frac{f_{ck}}{MPa}\right)^{\frac{1}{3}} \cdot MPa = 0.587\ MPa$$

Capacity at wheel pair 2:

$$h_2 := 0.16\ m + \frac{0.65}{3.2} \cdot (0.33 - 0.16)\ m = 0.195\ m$$

$$d_{y\_2} := h_2 - c_{cover\_top} - \frac{\phi}{2} = 0.163\ m$$

$$d_{z\_2} := h_2 - c_{cover\_top} - \phi - \frac{\phi'}{2} = 0.15\ m$$

$$d_{ef\_2} := \frac{d_{y\_2} + d_{z\_2}}{2} = 0.156\ m$$

$$k_2 := min\left(1 + \left(\frac{200}{\frac{d_{ef\_2}}{mm}}\right)^{\frac{1}{2}}, 2\right) = 2$$

$$\rho_{y\_2} := \frac{\frac{2}{3} A_s + A'_s}{d_{y\_2} \cdot b} = 0.0113$$

$$\rho_{z\_2} := \frac{A_{s\_z} + A'_{s\_z\_2}}{d_{z\_2} \cdot b} = 0.0039$$

$$\rho_{l\_2} := min\left(\sqrt{\rho_{y\_2} \cdot \rho_{z\_2}}, 0.02\right) = 0.0066$$

$$v_{Rd\_c\_2} := C_{Rd\_c} \cdot k_2 \cdot \left(100 \cdot \rho_{l\_2} \cdot \frac{f_{ck}}{MPa}\right)^{\frac{1}{3}} \cdot MPa$$

Calculation of punching:

The shear induced along the control perimeter is assumed to be constant, as well as the effective depth.

The punching shear is first checked at each wheel load separately, regardless if the control perimeters overlap. Then, the cases at which the control perimeters overlaps is checked.

Check of wheel pair 1, separately:

$b_{wheel} := 0.4\ m$ $l_{wheel} := 0.5\ m$

$u_1 := 2 \cdot \left(b_{wheel} + 4 \cdot d_{ef\_1}\right) + 2 \cdot \left(l_{wheel} + 4 \cdot d_{ef\_1}\right) = 5.742\ m$ Length of control perimeter

$P_1 := \frac{v_{Rd\_c\_1} \cdot u_1 \cdot d_{ef\_1}}{\left(1 + D\right) \cdot \gamma_{traffic}} = 419.773\ kN$ Maximum wheel load

$B_1 := 4 \cdot P_1 = 1679.091\ kN$ Corresponding B-value to maximum wheel load

Check of wheel pair 2, separately:

$u_2 := 2 \cdot \left(b_{wheel} + 4 \cdot d_{ef\_2}\right) + 2 \cdot \left(l_{wheel} + 4 \cdot d_{ef\_2}\right) = 4.297\ m$

$P_2 := \frac{v_{Rd\_c\_2} \cdot u_2 \cdot d_{ef\_2}}{\left(1 + D\right) \cdot \gamma_{traffic}} = 232.718\ kN$

$B_2 := 4 \cdot P_2 = 930.872\ kN$

Check of overlapping control perimeters

$u_{overlap} := 2 \cdot \left(b_{wheel} + 1.3\ m + 4 \cdot d_{ef\_1}\right) + 2 \cdot \left(l_{wheel} + 4 \cdot d_{ef\_1}\right) = 8.342\ m$

$P_{overlap} := \frac{v_{Rd\_c\_1} \cdot u_{overlap} \cdot d_{ef\_1}}{\left(1 + D\right) \cdot \gamma_{traffic}} = 609.864\ kN$

$B_{overlap} := 2 \cdot P_{overlap} = 1219.728\ kN$

$min\left(B_1, B_2, B_{overlap}\right) = 930.872\ kN$ Dimensioning B-value

Moment:

The critical section for the moment is defined at the support.

Moment capacity:

The moment capacity is calculated with:

$$M_{Rd\_crit} = \alpha \cdot f_{cd} \cdot b \cdot x \cdot \left(d_{sup} - \beta \cdot x\right) + \sigma'_s \cdot A'_s \cdot \left(d_{sup} - d'_{sup}\right)$$

$\alpha := 0.81$ $\beta := 0.416$

$d_{sup} := h_{sup} - c_{cover\_top} - \frac{\phi}{2} = 0.298\ m$ $d'_{sup} := c_{cover\_bottom} + \frac{\phi'}{2} = 0.025\ m$

$\varepsilon_{cu} := 0.0035$ $\varepsilon_{sy} := \frac{f_{yd}}{E_s} = 0.003$

The height of the compression zone, x, is found by the equation:

$$\alpha \cdot f_{cd} \cdot b \cdot x + \sigma'_s \cdot A'_s = \sigma_s \cdot A_s$$

Assuming all reinforcement yielding:

$\sigma_s := f_{yd}$ $\sigma'_s := f_{yd}$

Which gives :

$$x := \frac{\sigma_s \cdot A_s - \sigma'_s \cdot A'_s}{\alpha \cdot f_{cd} \cdot b} = 0.059\ m$$

$\varepsilon_s := \frac{d_{sup} - x}{x} \cdot \varepsilon_{cu} = 0.014$ $\varepsilon'_s := \frac{x - d'_{sup}}{x} \cdot \varepsilon_{cu} = 0.002$

As $\varepsilon'_s < \varepsilon_{sy}$ the assumption that all reinforcement is yielding is not correct

Iteration found the solution:

$x := 0.06087\ m$ $\varepsilon_s := \frac{d_{sup} - x}{x} \cdot \varepsilon_{cu} = 0.014$ $\varepsilon'_s := \frac{x - d'_{sup}}{x} \cdot \varepsilon_{cu} = 0.002$

With the tensile reinforcement yielding, but not the compressive reinforcement

$\sigma_s := f_{yd} = 539.13\ MPa$ $\sigma'_s := E_s \cdot \varepsilon'_s = 412.502\ MPa$

This yields a moment capacity of:

$$M_{Rd\_crit} := \alpha \cdot f_{cd} \cdot b \cdot x \cdot \left(d_{sup} - \beta \cdot x\right) + \sigma'_s \cdot A'_s \cdot \left(d_{sup} - d'_{sup}\right) = 347.664\ kN \cdot m$$

Calculation of B-value:

$$I_1 := \frac{h_{edgebeam}^{\ 3} \cdot w_{edgebeam} + h_{edge}^{\ 3} \cdot \left(L + w_{edgebeam} - \alpha_{wheel}\right)}{12} = \begin{bmatrix} 1.122 \cdot 10^{10} \\ 1.064 \cdot 10^{10} \end{bmatrix} mm^4$$

$$I_2 := \frac{h_{sup}^{\ 3}}{12} = \left(2.995 \cdot 10^{9}\right) \frac{1}{m} \cdot mm^4$$

$$c := \frac{3 \cdot E_{ck} \cdot I_2}{\alpha_{wheel}^{\ 3}} = \begin{bmatrix} 890.567 \\ 22.097 \end{bmatrix} MPa$$

$$n := \left(\frac{c}{4 \cdot E_{ck} \cdot I_1}\right)^{\frac{1}{4}} = \begin{bmatrix} 0.874 \\ 0.352 \end{bmatrix} \frac{1}{m}$$

Effective width with respect to moment:

$$b_{eff\_mom} := \frac{2}{n} = \begin{bmatrix} 2.288 \\ 5.689 \end{bmatrix} m$$

In the same way as for the shear, a distribution factor can be defined by dividing the load by the length it is distributed over:

$$Length_1 := 1.3\ m + b_{eff\_mom_0} = 3.588\ m \qquad Length_2 := 1.3\ m + b_{eff\_mom_1} = 6.989\ m$$

$$\chi_{mom1} := \frac{B}{Length_1} = 0.279\ \frac{1}{m}$$

$$\chi_{mom2} := \frac{B}{Length_2} = 0.143\ \frac{1}{m}$$

The final distribution factor is defined as a weighted average when considering the distribution factors from each load and the distance from the loads to the support:

$$\chi_{mom} := \frac{\chi_{mom1} \cdot \alpha_{wheel_0} + \chi_{mom2} \cdot \alpha_{wheel_1}}{\alpha_{wheel_0} + \alpha_{wheel_1}} = 0.174\ \frac{1}{m}$$

In the same way as for the shear, the maximum B-value is calculated by:

$$Q_{B\_mom} \cdot \chi_{mom} \cdot \frac{M_{crit}}{100\ kN} \cdot \left(1 + D\right) \cdot \gamma_{traffic} + M_{self}$$

M_{crit} is the moment in the critical section from a load of 100 kN in the midpoint between the wheels:

$$M_{crit} := \left(\text{mean}\left(\alpha_{wheel}\right) + \frac{l_{wheel}}{2}\right) \cdot 100\ kN = 180\ kN \cdot m$$

Moment in the critical section from the self-weight:

$$M_{self\_edgebeam} := \rho_c \cdot \gamma_{self} \cdot b \cdot h_{edgebeam} \cdot w_{edgebeam} \cdot \left(L + \frac{w_{edgebeam}}{2} \right) = 35.417 \ \boldsymbol{kN \cdot m}$$

$$M_{self\_slab} := q_{edge} \cdot L \cdot \frac{L}{2} + \frac{\left(q_{sup} - q_{edge} \right) \cdot L}{2} \cdot \frac{L}{3} = 33.28 \ \boldsymbol{kN \cdot m}$$

$$M_{self\_surf} := h_{surface} \cdot L \cdot \frac{L}{2} \cdot \rho_{surf} \cdot b = 11.264 \ \boldsymbol{kN \cdot m}$$

$$M_{self} := M_{self\_slab} + M_{self\_edgebeam} + M_{self\_surf} = 79.961 \ \boldsymbol{kN \cdot m}$$

Maximum value of B for the specific load case:

$$Q_{B\_mom} := \frac{M_{Rd\_crit} - M_{self}}{\chi_{mom} \cdot \boldsymbol{m} \cdot \frac{M_{crit}}{100 \ \boldsymbol{kN}} \cdot \left(1 + D \right) \cdot \gamma_{traffic}} = 432.748 \ \boldsymbol{kN}$$

Appendix B- Comparison between simplified calculations and linear FE-models

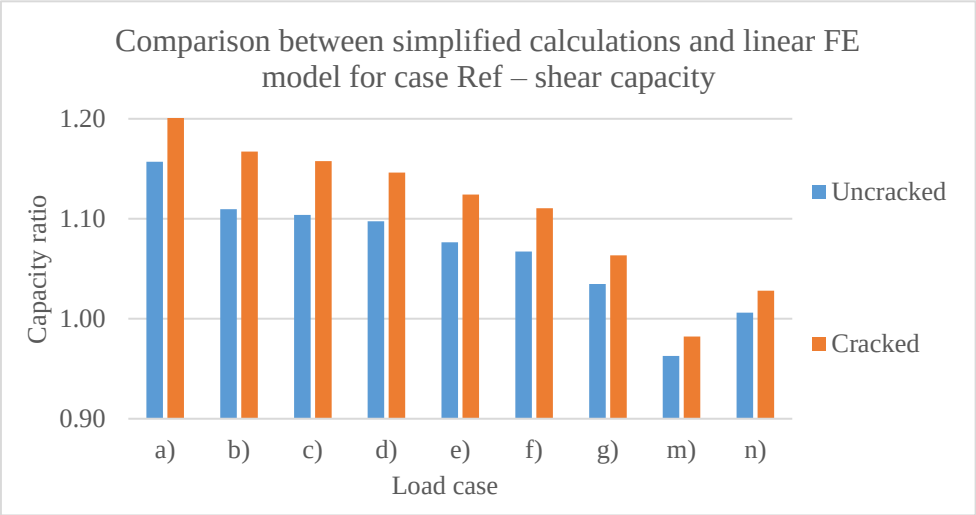

Figure B.1: Comparison between simplified hand calculations and linear FE-model for case Ref, considering shear capacity for both uncracked and cracked concrete in the transversal direction.

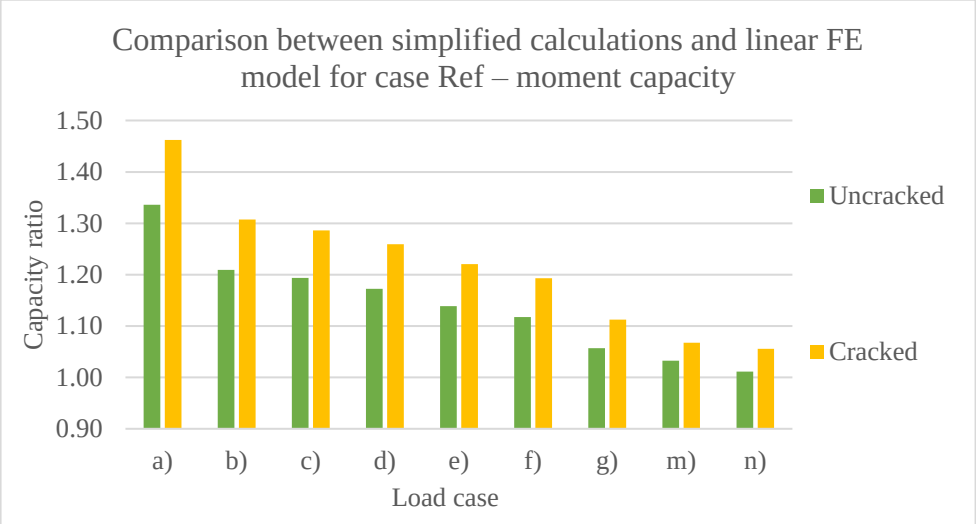

Figure B.2: Comparison between simplified hand calculations and linear FE-model for case Ref, considering moment capacity for both uncracked and cracked concrete in the transversal direction.

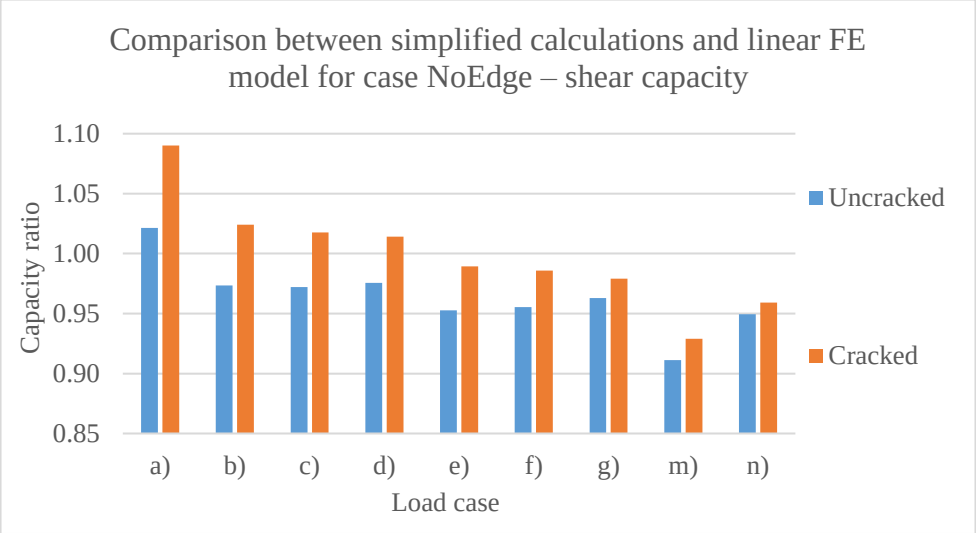

Figure B.3: Comparison between simplified hand calculations and linear FE-model for case NoEdge, considering shear capacity for both uncracked and cracked concrete in the transversal direction.

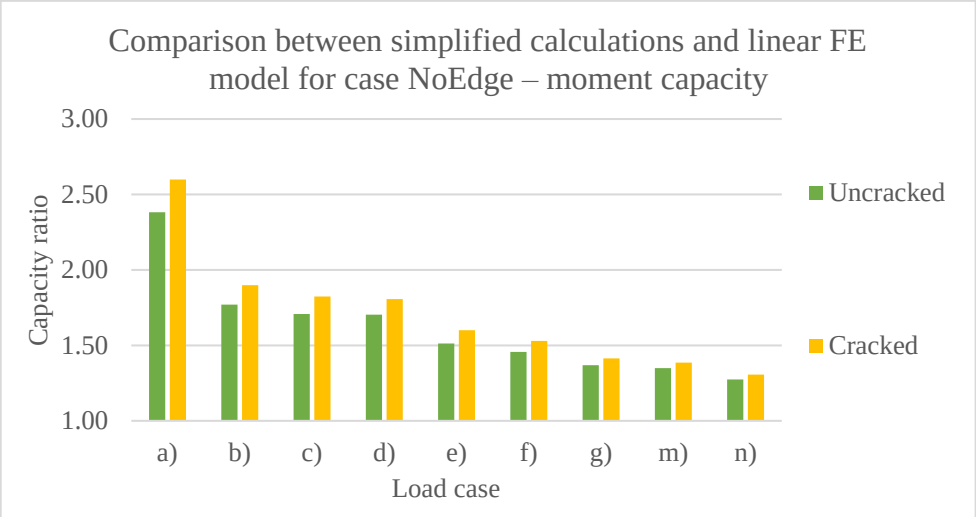

Figure B.4: Comparison between simplified hand calculations and linear FE-model for case NoEdge, considering moment capacity for both uncracked and cracked concrete in the transversal direction.

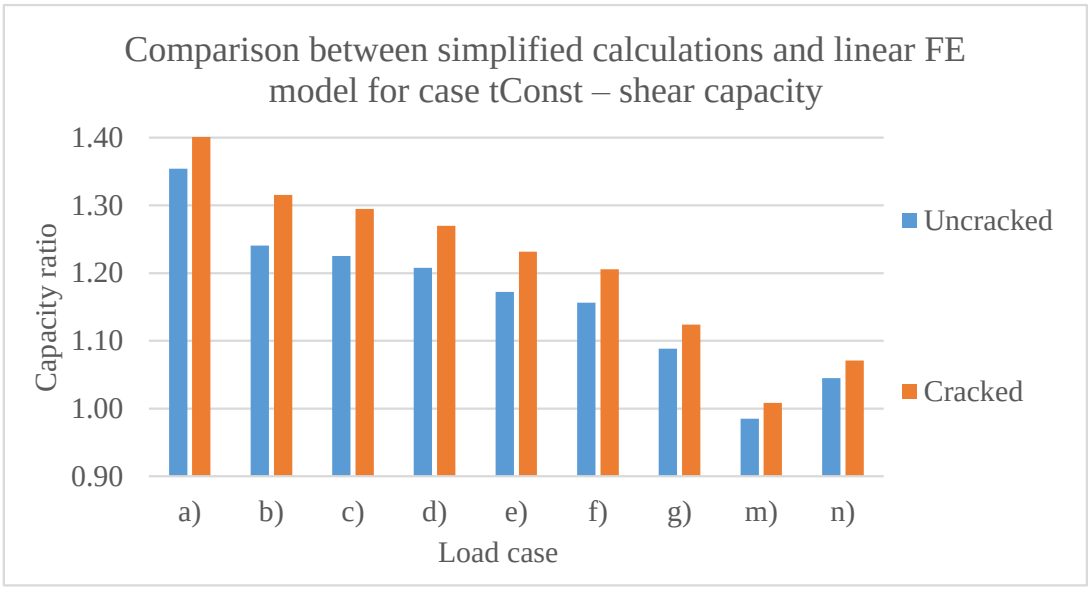

Figure B.5: Comparison between simplified hand calculations and linear FE-model for case tConst, considering shear capacity for both uncracked and cracked concrete in the transversal direction.

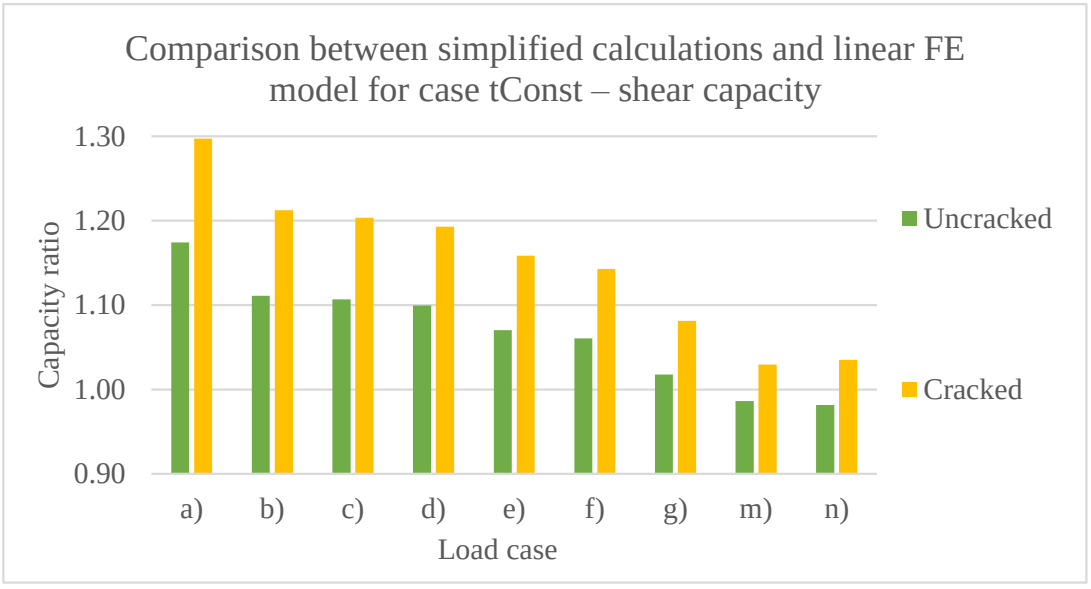

Figure B.6: Comparison between simplified hand calculations and linear FE-model for case tConst, considering moment capacity for both uncracked and cracked concrete in the transversal direction.

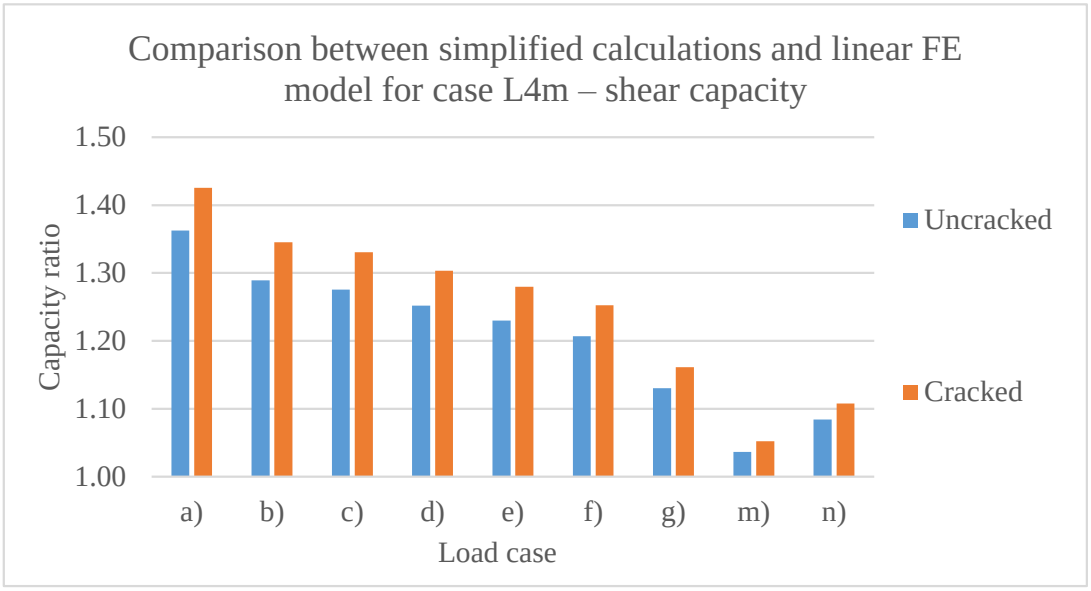

Figure B.7: Comparison between simplified hand calculations and linear FE-model for case L4m, considering shear capacity for both uncracked and cracked concrete in the transversal direction.

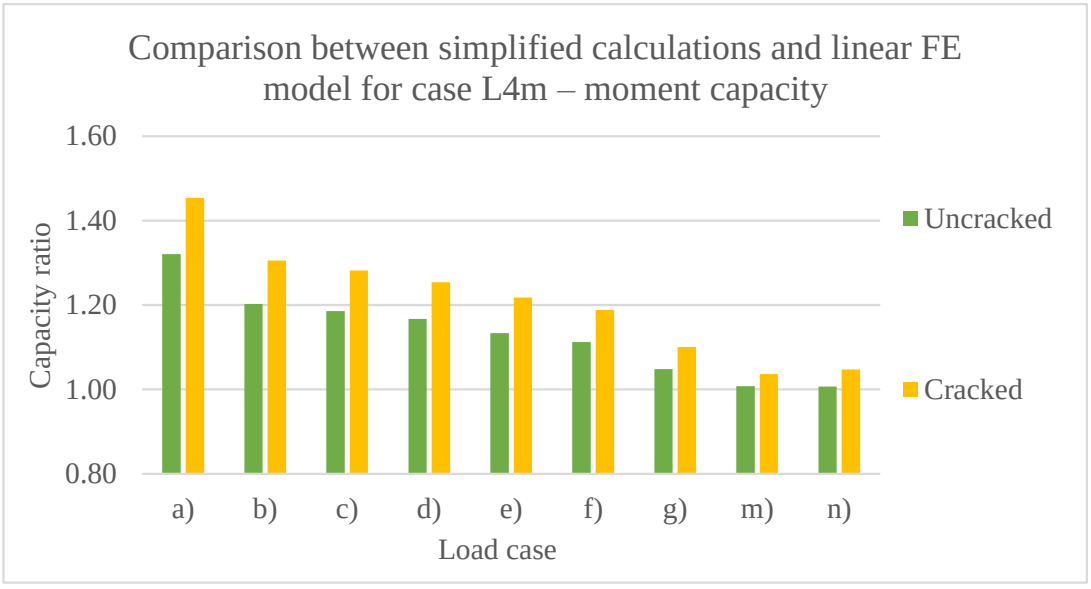

Figure B.8: Comparison between simplified hand calculations and linear FE-model for case L4m, considering moment capacity for both uncracked and cracked concrete in the transversal direction.

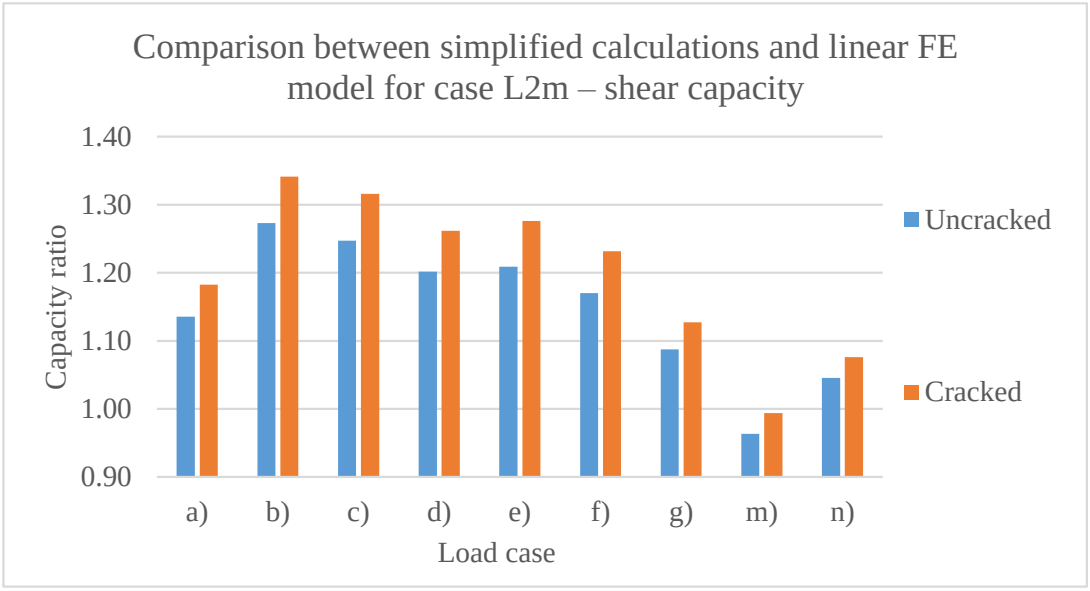

Figure B.9: Comparison between simplified hand calculations and linear FE-model for case L2m, considering shear capacity for both uncracked and cracked concrete in the transversal direction.

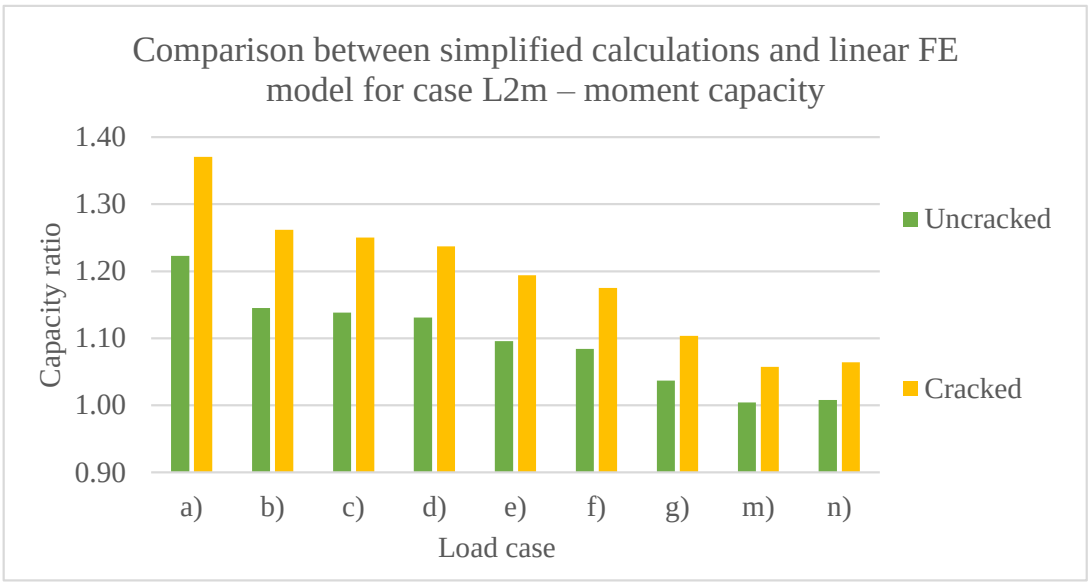

Figure B.10: Comparison between simplified hand calculations and linear FE-model for case L2m, considering moment capacity for both uncracked and cracked concrete in the transversal direction.

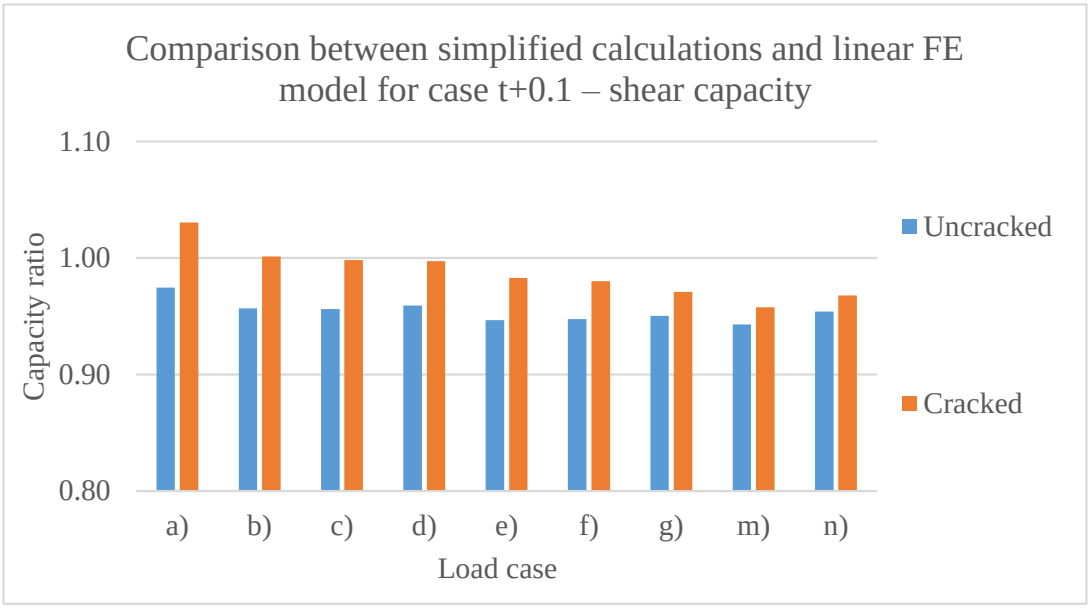

Figure B.11: Comparison between simplified hand calculations and linear FE-model for case t+0.1, considering shear capacity for both uncracked and cracked concrete in the transversal direction.

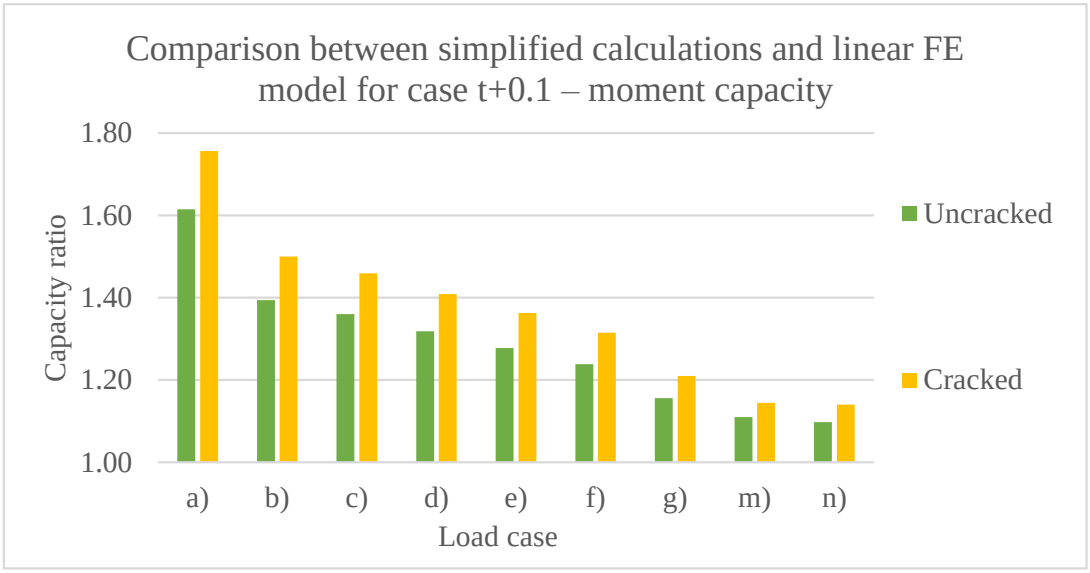

Figure B.12: Comparison between simplified hand calculations and linear FE-model for case t+0.1, considering moment capacity for both uncracked and cracked concrete in the transversal direction.

Appendix C- Punching shear

Calculation for punching shear capacity are presented in Appendix A.

Table C.1: A and B design value for punching shear resistance [kN] for each geometry case and loading case.

Case	Ref	NoEdge	tConst	L4m	L2m	t+0.1
a)	465.4	465.4	678.2	465.4	487.6	836.9
b)	775.1	775.1	1068.1	775.1	811.9	1273.55
c)	930.9	930.9	1356.5	930.9	975.1	1673.7
d)	846.2	846.2	1233.2	846.2	886.5	1521.6
e)	768.1	768.1	1027.0	768.1	1207.0	1200.4
f)	1057.8	1057.8	1541.4	1057.8	1108.1	1901.9
g)	1057.8	1057.8	1541.4	1057.8	1108.1	1901.9
m)	930.9	930.8	1356.5	930.9	975.1	1673.7
n)	846.2	846.2	1233.2	846.2	886.5	1521.6

DEPARTMENT OF ARCHITECTURE AND
CIVIL ENGINEERING
CHALMERS UNIVERSITY OF TECHNOLOGY
Gothenburg, Sweden 2025
www.chalmers.se

CHALMERS
UNIVERSITY OF TECHNOLOGY